bioRxiv preprint doi: https://doi.org/10.1101/2025.04.08.647738; this version posted April 9, 2025. The copyright holder for this preprint (which was not certified by peer review) is the author/funder, who has granted bioRxiv a license to display the preprint in perpetuity. It is made available under a CC-BY 4.0 International license.

Title: Glial *betaPix* is essential for blood vessel integrity in the zebrafish brain

ShihChing Chiu[1], Qinchao Zhou[1], Chenglu Xiao[2], Linlu Bai[1], Xiaojun Zhu[1,*], Wanqiu Ding[1,*], and Jing-Wei Xiong[1,2,*,#]

[1]Beijing Key Laboratory of Cardiometabolic Molecular Medicine, Institute of Molecular Medicine, and College of Future Technology, Peking University, Beijing 100871, China; [2]School of Basic Medical Sciences, The Second Affiliated Hospital, Institute of Biomedical Innovation, The MOE Basic Research and Innovation Center for the Targeted Therapeutics of Solid Tumors, Jiangxi Medical College, Nanchang University, Nanchang 330031, China

*Corresponding authors: WD (dingwq@pku.edu.cn), XZ (zhuxiaojun@pku.edu.cn), and JWX (jingwei_xiong@pku.edu.cn)

#Lead Contact: Jing-Wei Xiong, Ph.D. (jingwei_xiong@pku.edu.cn)

bioRxiv preprint doi: https://doi.org/10.1101/2025.04.08.647738; this version posted April 9, 2025. The copyright holder for this preprint (which was not certified by peer review) is the author/funder, who has granted bioRxiv a license to display the preprint in perpetuity. It is made available under a CC-BY 4.0 International license.

Abstract

The formation of blood-brain barrier and vascular integrity depends on the coordinative development of different cell types in the brain. Previous studies have shown that zebrafish *bubblehead* (*bbh*) mutant, which has mutation in the *betaPix* locus, develops spontaneous intracerebral hemorrhage during early development. However, it remains unclear in which brain cells *betaPix* may function. Here, we established a highly efficient conditional knockout method in zebrafish by using homology-directed repair (HDR)-mediated knockin and knockout technology, and generated *betaPix* conditional trap (*betaPix*^{ct}) allele in zebrafish. We found that *betaPix* in glia, but neither neurons, endothelial cells, nor pericytes, was critical for glial and vascular development and integrity, thus contributing to the formation of blood-brain barrier. Single-cell transcriptome profiling revealed that microtubule aggregation signaling stathmins and pro-angiogenic transcription factors *Zfhx3/4* were down-regulated in glial and neuronal progenitors, and further genetic analysis suggested that betaPix acted upstream on the PAK1-Stathmin and Zfhx3/4-Vegfaa signaling to regulate glia migration and vascular integrity. Therefore, this work reveals that glial *betaPix* plays an important role in brain vascular integrity in zebrafish embryos and possibly human cells.

Keywords: *betaPix*; hemorrhage; glial migration; knock-in; stathmin

bioRxiv preprint doi: https://doi.org/10.1101/2025.04.08.647738; this version posted April 9, 2025. The copyright holder for this preprint (which was not certified by peer review) is the author/funder, who has granted bioRxiv a license to display the preprint in perpetuity. It is made available under a CC-BY 4.0 International license.

Introduction

Intracerebral hemorrhage (ICH) is a life-threatening stroke type with the worst prognosis and few proven clinical treatments. Most patients who survive intracerebral hemorrhage end up with disabilities and are at risk for recurrency, cognitive decline, and systemic vascular issues, making this condition particularly significant among neurological disorders [1,2]. Several rodent models have been used for modeling ICH, including autologous blood injection, collagenase injection, thrombin injection, and micro-balloon inflation techniques [3]. Zebrafish (Danio rerio) exhibit a closed circulatory system and regulatory pathways that are highly conserved among vertebrates [4] with relatively cheap and easy to maintain disease models. Over the past decades, varieties of zebrafish mutants that spontaneously developed brain hemorrhage have been generated in mutagenesis screens, such as *redhead* [5], *reddish* [6,7] and *bubblehead* (*bbh*) [8,9]. Elucidating mutated gene function in these zebrafish models enables us to gain insights into the genetic basis and pathophysiological mechanisms of ICH development. The *bbh* mutant was identified independently in two large-scale ethylnitrosourea-induced mutagenesis screens [8,9] and positional cloning revealed that p21-activated kinase (Pak)-interacting exchange factor beta (*betaPix*) gene was mutated in *bbh* mutants [10]. *betaPix* contains SH3 domain that binds group I PAKs, and Dbl homology (DH) and pleckstrin homology (PH) domains that function as a RhoGEF to interact with Rac/Cdc42 small GTPases [11], thus participating in multiple cellular pathways to regulate cell polarity, adhesion and migration [12].

bioRxiv preprint doi: https://doi.org/10.1101/2025.04.08.647738; this version posted April 9, 2025. The copyright holder for this preprint (which was not certified by peer review) is the author/funder, who has granted bioRxiv a license to display the preprint in perpetuity. It is made available under a CC-BY 4.0 International license.

Various studies have reported that brain vessels are highly supported by neurons and glial cells during development and regeneration [13,14]. Glial-specific *betaPix* have been proposed to interact with *αvβ8* integrin and the Band 4.1s in glia, which link to multiple intracellular signaling effectors such as *Wnt7a* and *Wnt7b* [15], but this hypothesis was not experimentally addressed [16]. To this end, *betaPix* has been shown to interact with *αvβ8* integrins and mediate focal adhesion formation and thus modulate cerebral vascular stability in *bbh* zebrafish mutant [17]. Integrins are the main molecular link between cells and the extracellular matrix (ECM) which serve as scaffolds in the perivascular space. Based on a chemical suppressor screening of *bbh* hemorrhages, we have previously reported that a small molecule called miconazole downregulated the pErk-matrix metalloproteinase 9 (Mmp9) signaling to reduce ECM degradation, thus improving vascular integrity [18]. However, how *betaPix* cell-type specifically contributes to vascular integrity and maturation remains unclear. Here, we generated *betaPix* conditional trap (*betaPix*^{ct}) alleles by using a CRISPR/HDR-based Zwitch method, and found that betaPix acted mainly in glia to regulate glial and vascular integrity *via* Stathmin and Zfhx3/4 signaling. Therefore, this work provides the first experimental evidence that betaPix acts in glia for vascular integrity development, and its functional conservation between zebrafish and human cells may further guide us to decipher the genetic basis of ICH in the future.

bioRxiv preprint doi: https://doi.org/10.1101/2025.04.08.647738; this version posted April 9, 2025. The copyright holder for this preprint (which was not certified by peer review) is the author/funder, who has granted bioRxiv a license to display the preprint in perpetuity. It is made available under a CC-BY 4.0 International license.

Results

Generating *betaPix* conditional trap (*betaPix*^{ct}) allele by an HDR-mediated knockin and knockout method

To study *betaPix* function in cell-specific manner, we utilized a donor vector with an invertible gene trap cassette *via* HDR (Zwitch) [19-21] for generating *betaPix* conditional trap (*betaPix*^{ct}) alleles. Zwitch consists of a splice acceptor conjugated to a red fluorescent protein *via* a 2A self-cleaving peptide, flanked by two LoxP sites and two Lox 5171 sites in reciprocal orientations. Outside this conditional trap cassette, we included a lens-specific enhanced green fluorescence protein *α*-crystallin:EGFP for screening knockout founders, as well as inserted both left and right arms for targeting homologous sequences on the genome. We modified the Zwitch vector by adding a glycine-serine-glycine (GSG) spacer in front of the 2A peptide to enhance cleavage efficiency, and adding universal guide RNA (UgRNA)[22] target sequences outside the left and right homologous arms for linearizing donor vector (Figures 1A and S1A). We chose CRISPR/Cas9 system to generate double-strand breaks (DSBs) on intron 5 of the *betaPix* locus, and chose the most efficient guide RNAs based on their efficiency to induce CRISPR indels. We used either long arms such as ~1000 bp or short arms such as 24 bp that located upstream and downstream the guide RNA sites. We then co-injected the donor vectors with targeting guide RNA, universal guide RNA, and Cas9 mRNA into one-cell-stage embryos. At 4 days post-fertilization (dpf), we selected *α*-crystallin-EGFP-positive embryos (F_0) for raising to adulthood, and pre-selected F_0 founders by examining inheritable EGFP reporter expression of F_1 embryos. To confirm

bioRxiv preprint doi: https://doi.org/10.1101/2025.04.08.647738; this version posted April 9, 2025. The copyright holder for this preprint (which was not certified by peer review) is the author/funder, who has granted bioRxiv a license to display the preprint in perpetuity. It is made available under a CC-BY 4.0 International license.

the correct homologous recombination in the *betaPix* locus, we identified potential founders by genomic PCR to examine Zwitch insertion in the *betaPix* locus. Precise knock-in genotypes were further verified using Sanger sequencing (Figures 1B, 1C, S1B). Among 184 adult F_0 founders with α-crystallin-EGFP expression, we found 84 founders had EGFP-positive F_1 embryos, and 7 founders had expected PCR fragments around both 5' and 3' arms, which two founders had correct insertions in the *betaPix* locus by Sanger sequencing (Figure S1C), thus achieving ~1% efficiency on generating conditional alleles. Briefly, we established an efficient method for generating conditional knockin/knockout mutants in general, and generated a conditional gene trap line Ki(*betaPix*:Zwitch) in the *betaPix* locus in particular, which is referred to as $betaPix^{ct}$ hereafter.

A previous work has shown *bubblehead* (bbh^{m292}) mutant with a hypomorphic mutation in *betaPix*, and bbh^{fn40a} mutant with reduced *betaPix* transcripts without finding mutations in the coding region and the splicing sites [10]. bbh^{fn40a} mutants developed cerebral hemorrhages phenotype between 36 to 52 hpf (Figure S1D and S1E). To characterize the $betaPix^{ct}$ allele, we injected one-cell-stage $betaPix^{ct/ct}$ embryos with *Cre* mRNA to induce global inversion of Zwitch and deletion of *betaPix*. As expected, we found Cre-induced precise inversion in $betaPix^{m/m}$ as confirmed by Sanger sequencing (Figure 1C) and severe brain hemorrhages developed in the time window similar to bbh^{fn40a} mutants (Figures 1D and 1E). Consistently, qPCR analysis showed that *betaPix* decreased and *RFP* increased in heterozygous $betaPix^{m/+}$ and homozygous

bioRxiv preprint doi: https://doi.org/10.1101/2025.04.08.647738; this version posted April 9, 2025. The copyright holder for this preprint (which was not certified by peer review) is the author/funder, who has granted bioRxiv a license to display the preprint in perpetuity. It is made available under a CC-BY 4.0 International license.

131 *betaPix*$^{m/m}$ mutants compared with *betaPix*$^{ct/ct}$ wild-type siblings, while *alphaPix*
132 expression was not affected (Figure 1F). Of note, *TagRFP* expression in *betaPix*$^{m/+}$
133 (after Cre-mediated recombination in *betaPix*$^{ct/+}$ embryos) reflected endogenous
134 *betaPix* expression in the boundary of midbrains and hindbrains as well as the
135 hindbrains (Figure S1F and S1G). Together, these results suggest that the conditional
136 trap *betaPix*$^{ct/ct}$ zebrafish is functional for visualizing endogenous *betaPix* expression
137 (knockin) and loss-of-function study (conditional knockout).
138
139 **_betaPix_$^{m/m}$ mutant has brain hemorrhages, central arteries defects and abnormal**
140 **glial structure that is partially rescued by Pak1 inhibitor IPA3 treatment**
141 The main phenotypes in *bbh* mutants consist of brain hemorrhage and hydrocephalus
142 as early as 36 hpf, as well as poor endothelial–mesenchymal contacts and defective
143 central arteries (CtAs) sprouting in the hindbrain [10,17]. To demonstrate the practicability
144 of *betaPix* conditional trap lines, we assessed vasculature and glia in the hindbrain by
145 using light sheet fluorescence microscopy. Global *betaPix* inactivation in *betaPix*$^{m/m}$
146 mutants resulted in severe cerebral hemorrhages and defective angiogenesis in
147 hindbrain central arteries (Figures 1D, 1E, S2A and S2B), which is consistent with
148 previous studies [10,18].
149
150 It has been suggested that endothelial *betaPix* might not contribute to the occurrence of
151 brain hemorrhage [10]. During brain development, neurons and glia are important
152 perivascular cells and they orchestrate with endothelial cells in a temporal and spatial

bioRxiv preprint doi: https://doi.org/10.1101/2025.04.08.647738; this version posted April 9, 2025. The copyright holder for this preprint (which was not certified by peer review) is the author/funder, who has granted bioRxiv a license to display the preprint in perpetuity. It is made available under a CC-BY 4.0 International license.

153 pattern. Thus, we studied hindbrain radial glia development and found that radial glial
154 structure had disoriented arrangement and shorten process length in *betaPix*$^{m/m}$ embryos
155 compared to siblings (Figures 2A, 2B and S2C). As a result, neuronal and glial
156 precursors marker *nestin* increased while differentiated neuronal marker *pax2a*
157 decreased in *betaPix*$^{m/m}$ embryos, suggesting delayed neuronal development and
158 differentiation after *betaPix* inactivation (Figure 2C). By using global *betaPix* knockout
159 with multiple guide-RNA simultaneously [23], we found that CRISPR-induced *betaPix*
160 mutant F_0 embryos had almost identical phenotypes to those in *betaPix*^{fn40a} mutants
161 (Figure S3A-S3B), such as cerebral hemorrhages, central arteries defects, and abnormal
162 hindbrain glia and neuronal precursor development (Figures S3C to S3G), further
163 confirming the loss-of-function phenotypes in *betaPix*$^{m/m}$ mutants.
164
165 Zebrafish central arteries vascularization in the hindbrains starts at 29 hpf. Tip cells
166 start to form in the dorsal side of the primordial hindbrain channels (PHBC), sprout and
167 migrate into the hindbrain tissue, moving towards the center around 36 hpf to establish
168 connections with the basilar artery. A characteristic arch architecture forms at 48 hpf as
169 boundaries dividing the hindbrain into rhombomeres[24]. In *betaPix* knockouts, CtA
170 sproutings were restricted to the bottom of glial processes, thus not being able to
171 migrate upwards to form an arched structure (Figure 2D). The transcription factor SRY
172 box-2 (Sox2) is another marker gene for neuron and glial precursors. *Sox2*-positive
173 precursor cells tightly wrapped around the central artery in control siblings, but Sox2
174 precursor cells had loose contacts with the central arteries, with larger perivascular

bioRxiv preprint doi: https://doi.org/10.1101/2025.04.08.647738; this version posted April 9, 2025. The copyright holder for this preprint (which was not certified by peer review) is the author/funder, who has granted bioRxiv a license to display the preprint in perpetuity. It is made available under a CC-BY 4.0 International license.

distances in *betaPix* mutants (Figure 2E). These results implicate the impaired interactions between endothelial cells and neuronal/glial cells during development after *betaPix* deletion.

p21-activated kinase (Pak) is a binding partner for *betaPix*. *Pak2a* has been shown mediating downstream signaling in bbh^{m292} mutants. Group I PAK allosteric inhibitor IPA-3 covalently modifies and stabilizes the autoinhibitory N-terminal region of PAK1, PAK2 and PAK3 [25]. As expected, IPA-3 treatment significantly decreased incidence and intensity of cerebral hemorrhages in $betaPix^{m/m}$ mutant embryos (Figure 2F and 2G), while IPA-3 treatment had no effect on hematopoiesis in $betaPix^{ct/ct}$ control siblings. In addition, central arterial defects were partially rescued in $betaPix^{m/m}$ mutant embryos after IPA-3 treatment, showing increased endothelial protruding into the hindbrain and more arch structure formation (Figure 2H and 2I). IPA-3 treatment also decreased abnormal glial process arrangements, which the lengths of glial processes statistically reached the levels of the control siblings (Figure 2J). Thus, these data suggest that the betaPix-Pak1/2 signaling regulates brain vascular integrity during development.

Glial-specific *betaPix* knockouts recapture its global knockout phenotypes

To investigate *betaPix* function in different types of perivascular cells, we generated glial- or neuronal-specific transgenic lines using either glial fibrillary acidic protein (*gfap*) [26] or *huC* [27] promoters to drive *EGFP-Cre* fusion gene expression under

bioRxiv preprint doi: https://doi.org/10.1101/2025.04.08.647738; this version posted April 9, 2025. The copyright holder for this preprint (which was not certified by peer review) is the author/funder, who has granted bioRxiv a license to display the preprint in perpetuity. It is made available under a CC-BY 4.0 International license.

197 *betaPix*$^{ct/ct}$ background, respectively (Figure S4A). EGFP signals reported *Cre*
198 expression while RFP signals efficiently reported Cre-induced gene trap cassette
199 inversion and disruption of *betaPix* expressions (Figure S4B to S4F). Interestingly,
200 glial-specific *betaPix* knockouts developed severe cerebral hemorrhages and abnormal
201 central arteries vascularization, which were partially rescued by IPA-3 treatment
202 (Figure 3A to 3C), highlighting betaPix function in glia *via* Pak1/2 signaling. On the
203 other hand, neither vascular-, neuronal-, nor mural-specific deletion of *betaPix* had
204 evident *betaPix* mutant phenotypes (Figure S5A to S5D). These results suggest that
205 glial *betaPix* plays crucial roles in zebrafish embryonic vascular integrity and glial
206 development *via* regulating *Pak* activities.
207
208 **Single-cell transcriptome profiling reveals that stathmins in *gfap*-positive**
209 **progenitors were affected in *betaPix* knockouts**
210 To investigate the interplays between glial and hemorrhagic pathology caused by
211 *betaPix* loss-of-function, we profiled the cranial tissues of CRISPR-edited zebrafish at
212 1 and 2 dpf using the 10X Chromium single-cell RNA sequencing (scRNA-seq)
213 platform (Figure 4A). Multi-guide targeting was able to generate almost 100% F_0 null
214 mutants, allowing us to select mutant embryos before brain hemorrhages from 36 hpf.
215 Low-quality cells were excluded based on the numbers of genes detected and
216 percentages of reads mapped to mitochondrial genes per sample. A total of 38,670 cells
217 passed quality control and were used for subsequent analyses. Uniform manifold
218 approximation and projection (UMAP) identified 71 cell clusters, which represented 24

bioRxiv preprint doi: https://doi.org/10.1101/2025.04.08.647738; this version posted April 9, 2025. The copyright holder for this preprint (which was not certified by peer review) is the author/funder, who has granted bioRxiv a license to display the preprint in perpetuity. It is made available under a CC-BY 4.0 International license.

zebrafish cranial cell types based on known marker gene expression profiles (Figure 4B and S6A). Enriched gene markers were compared with previously annotated gene markers in the ZFIN database and literatures[28,29]. By comparing the proportion of cells in each sample, we found that most neuronal clusters had increased trends, while the numbers of progenitors, endothelial cells, erythrocytes, neural crests, muscles, cartilages, retinas (photoreceptor precursor cells), olfactory bulbs, or epidermis and pharyneal arches were reduced in *betaPix* knockout heads at 2 dpf (Figure 4C and S6B). This is consistent with the open public databases of single-cell transcriptome atlas where *betaPix* weakly expressed in a broad range of cells including glia, neurons and neuronal precursors, retinas, endothelial cells, pharynx, exocrine pancreas, olfactory cells and heart cells [30]. Given that *betaPix* is critical in glia during brain vascular integrity development (Figures 3 and S5), we examined the *gfap* expression among each cluster, and found relatively high *gfap* expression in clusters including progenitors, hindbrain, ventral diencephalon, ventral midbrain and floor plate (Figure S6A, arrow indicates). We next focused on the progenitor cluster, as of its enriched *gfap* expression and relatively more decreased cell numbers in *betaPix* mutants. Furthermore, this progenitor cluster exhibited high-level expression of cell proliferation and cell cycle related genes (*mki67*, *pcna*, *ccnd1*, *rrm1* and *rrm2*) as well as key glial-associated genes (*gfap*, *fabp7a*, *her4*.1, *cx43*, *id1*, *fgfbp3*, *atp1a1b* and *mdka*) (Table S1). From differentially expressed genes (DEGs) in this progenitor cluster between controls and *betaPix* knockouts at 2 dpf, enriched gene ontology (GO) terms revealed three major categories: epigenetic remodeling including chromatin silencing, negative regulation of

bioRxiv preprint doi: https://doi.org/10.1101/2025.04.08.647738; this version posted April 9, 2025. The copyright holder for this preprint (which was not certified by peer review) is the author/funder, who has granted bioRxiv a license to display the preprint in perpetuity. It is made available under a CC-BY 4.0 International license.

241 transcription, chromatin packaging and nucleosome positioning; microtubule
242 organizations including microtubule depolymerization, regulation of microtubule
243 polymerization and microtubule cytoskeleton organization; and neurotransmitter
244 secretion/transportation (Figure 4D). Of these signaling genes, we were particularly
245 interested in microtubule genes for further studies.
246
247 **Stathmin acts downstream of *betaPix* in glial migration *via* regulating tubulin**
248 **polymerization**
249 Microtubules are essential cytoskeletal elements composed of α/β-tubulin heterodimers.
250 The regulation of microtubule polymerization affects important cellular functions such
251 as mitosis, motor transport, and migration [31]. Based on the above scRNA-seq data
252 (Figures 4E and S6C), we then examined if microtubule polymerization genes
253 stathmins were affected in *betaPix* mutants. We found that stathmin1a (*stmn1a*),
254 stathmin1b (*stmn1b*), and stathmin4l (*stmn4l*) were relatively abundant in both the
255 whole brain and the progenitor cluster, and decreased specifically at 2dpf in *betaPix*
256 knockout progenitor cells (Figure 4E). Subsequent qRT-PCR revealed that these
257 stathmins expression decreased in both global *betaPix* knockouts (*betaPix*$^{m/m}$) and glial-
258 specific betaPix knockout glia (*gfap*:EGFP-Cre;*betaPix*$^{ct/ct}$) (Figure 4F and 4G), which
259 was further verified by RNA *in situ* hybridization analysis (Figure 4H). We next
260 investigated whether *Stathmins* act downstream to *betaPix* signaling on regulating
261 vascular integrity development. To this end, we found that *Pak1/2* inhibition enabled to
262 rescue down-regulated expressions of *stmn1a*, *1b* and *4l* in either global or glial-specific

bioRxiv preprint doi: https://doi.org/10.1101/2025.04.08.647738; this version posted April 9, 2025. The copyright holder for this preprint (which was not certified by peer review) is the author/funder, who has granted bioRxiv a license to display the preprint in perpetuity. It is made available under a CC-BY 4.0 International license.

betaPix knockout zebrafish (Figures 5A, 5B and S7A), supporting previous findings that *stathmin-1* acts downstream to *betaPix-Pak* signaling in neurite outgrowth in mice[32].

To test whether *Stathmin* family genes are important for vascular stability, we utilized CRISPR-induced F_0 knockout system simultaneously targeting the three stathmin genes. While singular stathmin gene knockout led to no evident phenotypes (data not shown), we found that simultaneously inactivating *stmn1a*, *stmn1b* and *stmn4l* caused brain hemorrhages and hydrocephalus in the brain, similar to that from *betaPix*^{fn40a} *and* *betaPix*$^{m/m}$ mutants (Figures 5C, 5D, S7B to S7E). By labeling both glia and vasculature with Tg(*gfap*:GFP; *kdrl*:mCherrry) transgenic embryos, we found that triple stathmin gene knockouts had impaired CtAs, abnormal glia and neuronal development in the hindbrain region (Figure 5E, 5F, S7F to S7H). Furthermore, overexpressing *stmn1b* by the *gfap* promoter partially rescued brain hemorrhages and delayed neuronal development in *bbh*^{fn40a} mutants (Figures 5G, 5H, S7I and S7J), of which glial processes elongation also improved, but CtAs defects failed to restore (Figures 5I, 5J and S7K). Thus, these data support the critical role of stathmins in glia.

To examine the direct role of *betaPix-stathmin* in glia, we turned to use human glioblastoma cell lines and manipulated the *betaPix* levels by siRNA knockdown or transgenic overexpression. We found that *betaPix* knockdown attenuated glial migration (Figures 5K, 5L, S7L to S7N), which is consistent with previous studies on

bioRxiv preprint doi: https://doi.org/10.1101/2025.04.08.647738; this version posted April 9, 2025. The copyright holder for this preprint (which was not certified by peer review) is the author/funder, who has granted bioRxiv a license to display the preprint in perpetuity. It is made available under a CC-BY 4.0 International license.

betaPix function in the endoderm [33], epithelial cells [34], neurons [35] and multiple carcinoma cell lines including glioblastoma [36-38]. Either *betaPix* or *Stmn1* overexpression led to a partial restoration of the impaired glial migration, suggesting *Stathmins* as downstream effectors of *betaPix*. Furthermore, immunofluorescence analysis revealed that *betaPix* knockdown led to abnormal accumulation of microtubules at the cell periphery, whereas ectopic expression of *betaPix* and *Stathmin* partially rescued these microtubule defects (Figures 5M and 5N). Together, these results suggest that *betaPix* depletion disrupts microtubule dynamics and leads to impaired glial development acting upstream to the *Pak-Stathmin* signaling, subsequently disrupting vascular integrity and resulting in brain hemorrhages. While the brain hemorrhages were only partially rescued and abnormal CtAs defects failed to restore, indicating that additional pathways may act downstream of *betaPix*.

Zfhx3/4 acts downstream of _betaPix_ in regulating vascular integrity development.

Previous studies have identified multiple signaling pathways important for zebrafish hindbrain angiogenic sprouting, such as VEGF, Notch, Wnt, Integrin β1, angiopoietin/TIE, and insulin-like growth factor signaling [39-42]. To investigate whether angiogenic signal is disrupted by *betaPix* depletion, we examined several angiogenic gene expression pattern by performing RNA *in situ* hybridization of embryos at 36 hpf. The expression level of *Vegfaa* in sprouting CtAs decreased in *bbh*^{fn40a} mutants (Figure 6A). Consistently, *betaPix* knockdown significantly reduced *VEGFA* expression in cultured glial cells, which was rescued by ectopic expression of *betaPix* (Figure 6B;

bioRxiv preprint doi: https://doi.org/10.1101/2025.04.08.647738; this version posted April 9, 2025. The copyright holder for this preprint (which was not certified by peer review) is the author/funder, who has granted bioRxiv a license to display the preprint in perpetuity. It is made available under a CC-BY 4.0 International license.

307 right panel). To explore how *betaPix* regulate *Vegf* signaling in glia, we also found a
308 significant enrichment of epigenetic and transcriptional regulation in progenitor cluster
309 indicated by the GO analysis of single-cell sequencing data (Figure 4D). Among these
310 candidate genes, transcription factor Zinc Finger Homeobox 3 (ZFHX3) is known to
311 mediate hypoxia-induced angiogenesis in hepatocellular carcinoma *via* transcriptional
312 activation of VEGFA [43]. Furthermore, ZFHX3 has been associated with stroke in
313 multiple genome-wide association studies [44-46]. Interestingly, we found that
314 transcription factors *Zfhx3* and *Zfhx4* significantly downregulated after *betaPix*
315 inactivation in cultured glial cells (Figure 6B), CRISPR-induced *betaPix* mutants at 2
316 dpf (Figure S8A), and glia-specific *betaPix* mutants (Figure S8B), thus suggesting that
317 *betaPix* acts upstream to Zfhx3/4-VEGFA signaling in regulating angiogenesis.
318
319 To determine whether *Zfhx3/4* is critical for vascular integrity by interacting with
320 *betaPix* in zebrafish, we depleted *Zfhx3* and *Zfhx4* simultaneously *via* CRISPR-
321 mediated F_0 knockouts (Figure S8C to S8E). We found that *zfhx3/4* knockouts
322 decreased *Vegfaa* expression at sprouting CtAs at 36 hpf (Figure 6C). *Zfhx3/4*
323 knockouts at 48 hpf had under-developed CtAs and reduced penetration of endothelial
324 cells into the hindbrain (Figure 6F and 6G), developed cerebral hemorrhages during 36
325 to 52 hpf, which are comparable with *betaPix* mutant phenotypes (Figure 6D-6G).
326 Despite up-regulated expression level of *nestin*, glial arrangement and processes
327 elongation remained statistically unaffected after *Zfhx3/4* inactivation (Figures 6F, 6G
328 and S8F). We next investigated whether increasing expression level of *Vegfaa* in

bioRxiv preprint doi: https://doi.org/10.1101/2025.04.08.647738; this version posted April 9, 2025. The copyright holder for this preprint (which was not certified by peer review) is the author/funder, who has granted bioRxiv a license to display the preprint in perpetuity. It is made available under a CC-BY 4.0 International license.

betaPix mutants was able to rescue impaired vascular integrity. By using *Zfhx4* mRNA microinjection into one-cell stage embryos in either *bbh*^{fn40a} mutants or CRISPR-induced *betaPix* knockouts, we found that ectopic expression of *Zfhx4* increased *Vegfaa* expression level (Figure 6L), thus leading to a drastic reduction of both percentages and volumes of brain hemorrhage shown in these mutants (Figures 6H, 6I, S8G to S8I), as well as improved CtAs and glial development (Figures 6J and 6K). In addition, scRNA-seq data showed that CRISPR-induced *betaPix* knockouts had down-regulated angiogenic gene expression in a cluster of endothelial cells (Figure 6M). Together, these data support the critical role of *Zfhx3/4* in vascular integrity and glial development probably acting upstream to VEGFA and downstream to betaPix.

Discussion

Conditional knockout technology in mice has been widely used to modify and determine targeted gene function in a cell-specific manner. Spatio-temporal specific modification is beneficial for studying embryonic lethality genes or investigating the function of targeted genes in specific cell populations. Despite being broadly utilized in mice, conditional knockouts in other animal models are limited due to technical difficulties. To this end, multiple research groups have designed different strategies for establishing floxed-mutant alleles, gene traps, and inducible Cas9 in zebrafish [47]. In particular, the Zwitch gene trap-based approach has been established successfully in zebrafish, enabling to simultaneously produce knockin reporter driven by the endogenous gene promoter and disrupting endogenous gene function [19-21]. We adapted

bioRxiv preprint doi: https://doi.org/10.1101/2025.04.08.647738; this version posted April 9, 2025. The copyright holder for this preprint (which was not certified by peer review) is the author/funder, who has granted bioRxiv a license to display the preprint in perpetuity. It is made available under a CC-BY 4.0 International license.

this strategy with the aid of CRISPR/Cas9 technology, and added a GSG spacer to enhance cleavage efficiency and universal guide RNA target sites on both homologous arms for producing linearized targeting vector. Moreover, we also found that utilizing either short or long homologous arms enables to achieve precise targeted integrations with this donor vector. Our short arms-based method can be broadly adapted because of less restrictions on arm sequences and easily engineering the donor vector. From the *betaPix* locus and other five unpublished loci that we already generated Zwitch alleles with ~1% correct insertions based on homologous recombination, we achieved Cre-induced, cell-specific deletion and functional analysis of targeted genes in both embryos and adult hearts. Therefore, our CRISPR-based Zwitch method can be widely applied for generating conditional mutant zebrafish in particular and possibly extended for other animal mutants in general.

Development of the vasculature in the central nervous system can be classified into three phases: vasculogenesis, angiogenesis and blood-brain barrier formation. The hallmark of CNS vasculature maturation is acquisition of BBB properties, establishing a stable environment crucial for brain homeostasis in response to extrinsic factors and physiological changes. The core features of the BBB include specialized tight junctions, highly selective transporters and limited immune cell trafficking [48,49]. In zebrafish, BBB can be functionally characterized from 3 dpf [50,51]. While *bubblehead* mutants acquire vessel rapture phenotype early before BBB maturation, presenting a good hemorrhagic model for studying early BBB

bioRxiv preprint doi: https://doi.org/10.1101/2025.04.08.647738; this version posted April 9, 2025. The copyright holder for this preprint (which was not certified by peer review) is the author/funder, who has granted bioRxiv a license to display the preprint in perpetuity. It is made available under a CC-BY 4.0 International license.

373 development. Multiple types of cells contribute to diverse aspects of BBB
374 development and maintenance, leading to proper vasculature function across
375 developmental timeline. Pericytes are perivascular cells embedded within the same
376 basement membrane with endothelial cells [52]. Pericyte-deficient mice with disrupting
377 PDGF-B signaling displayed BBB leakiness, reflecting altered pericyte coverage and
378 endothelial gene expressions [53-55]. Pericyte-secreted signals promoting the endothelial
379 survival, proliferation and sprout formation *via* multiple pathways such as
380 transforming growth factor-β (TGF-β) signaling [56-59], VEGF-VEGFR signaling [60,61],
381 Angiopoietin-Tie2 signaling [62-64], Sphingosine-1-phosphate (S1P) signaling [65] and
382 Notch signaling [66,67]. Apart from endothelial cells, pericytes also regulate
383 development of other members of the neurovascular unit. Pericytes regulate astrocyte
384 aquaporin-4 polarization and guide end-foot processes toward endothelial tubes [53,68].
385 In addition, pericytes secrete ECM molecules supporting the basement membrane and
386 regulation of the angioarchitecture [69-72].
387
388 Endothelial cells form the continuous inner layer of blood vessels with junctional
389 protein and selective transporters, which are the main subject of permeability
390 regulation in BBB. It is well accepted that endothelial cells do not show a
391 predetermined role and that the brain environment is sufficient to induce endothelial
392 barrier [73]. Accumulative evidences also point to critical role of endothelial signals in
393 regulating several aspects of BBB development. In particular, endothelial cell-derived
394 PDGF-B directly binds to surface receptor PDGFRβ on pericytes that are critical for

bioRxiv preprint doi: https://doi.org/10.1101/2025.04.08.647738; this version posted April 9, 2025. The copyright holder for this preprint (which was not certified by peer review) is the author/funder, who has granted bioRxiv a license to display the preprint in perpetuity. It is made available under a CC-BY 4.0 International license.

pericyte recruitment and function [74,75]. Although their barrier properties are non-assessed, angiocrine signals such as leukaemia inhibitory factor (LIF) and TGF-β induce both astrocyte [76] and oligodendrocyte differentiation [77], respectively. Wnt7a/b ligands secreted by neural progenitor cells bind to Frizzled receptors on endothelial cells, activating canonical Wnt signaling and downstream genes. WNT ligands knockouts lead to angiogenic defects and BBB leakages specifically in the CNS [78]. Endothelial GPR124, as a coactivator of canonical Wnt signaling, has important function in CNS-specific angiogenesis and BBB establishment [79-81]. Other signaling ligands such as angiopoietins and Ephrin family ligands orchestrate with Tie or EphB receptors on endothelial cells, respectively[82]. Briefly, complex interactions between BBB cell types orchestrate proper angiogenesis and CNS development in a spatio-temporal manner.

Compared with pericytes and endothelial cell signaling, we have less knowledge on glia signaling in the BBB development and maturation. Astrocytes ensheathe capillaries through polarized end feet that are enriched with aquaporin-4 (Aqp4) proteins, colocalized with inwardly rectified K^+ channels[83,84]. Functional coupling of ion and water fluxes plays a critical role in regulating local osmotic equilibrium. During development, radial glia is a neuroepithelial origin with heterogeneous populations that are able to generate neurons, astrocytes, and oligodendrocytes[85-88]. In zebrafish, radial glia has long been considered serving an astrocytic role. Radial glia in zebrafish enriches with several key molecular markers

bioRxiv preprint doi: https://doi.org/10.1101/2025.04.08.647738; this version posted April 9, 2025. The copyright holder for this preprint (which was not certified by peer review) is the author/funder, who has granted bioRxiv a license to display the preprint in perpetuity. It is made available under a CC-BY 4.0 International license.

for astrocytes and tight junctions while Aqp4^{+} radial glial processes rarely contact the vasculature[89]. A more recent article has reported that zebrafish *Glast*-expressing radial glia transform into astrocyte-like cells, displaying dense cellular processes, tiling behavior and proximity to synapses [90]. Whether end feet of these astrocytes enwrap capillary blood vessels and resemble mammalian astrocytes warranty future investigations. In agreement with mammalian astrocytes, two independent groups have shown that ablation of pan-glia results in progressive brain hemorrhage[91,92] or deficiency of spinal cord arteries development in zebrafish [93], demonstrating important role of zebrafish glia in BBB formation. Multiple glia/astrocyte-derived signals have been shown to contribute to endothelial barrier properties development. Astrocyte-expressed sonic hedgehog (Shh) bind to hedgehog (Hh) receptors on endothelial cells and contribute to the BBB functions by promoting junctional protein expression and the quiescence of the immune system [94-97]. Before BBB formation, notochord-derived Shh activity promote arterial cell fate on developing endothelial cells [98]. Shh stimulates the production of angiogenic cytokines, angiopoietins and interleukins, *via* downstream transcription factor *Gli* or non-canonical pathways crosstalks with iNOS/Netrin-1/PKC, RhoA/Rock, ERK/MAPK, PI3K/Akt, Wnt/β-catenin, and Notch signaling pathways [99]. VEGF is the main pro-angiogenic growth factor produced by various cell types that controls multiple vascular development steps, such as proliferation, migration, permeability and survival *via* interacting with VEGF receptors on endothelial cells. Inactivation of VEGFA in astrocytes leads to BBB disruption in multiple sclerosis models [100,101]. In early development of avascular

bioRxiv preprint doi: https://doi.org/10.1101/2025.04.08.647738; this version posted April 9, 2025. The copyright holder for this preprint (which was not certified by peer review) is the author/funder, who has granted bioRxiv a license to display the preprint in perpetuity. It is made available under a CC-BY 4.0 International license.

neural tube, VEGF derived from neuroectoderm serve as a central role in inducing tip cells sprouting from the perineural vascular plexus (PVNP) and formation of vasculature lumens from stem cells [102,103]. Ablating neuroglia reduces *vegfab* signals and leads to ectopic intersegmental vessels sprouting and vertebral arteries in zebrafish [93]. VEGF signaling orchestrates elaborately with other signaling pathways such as delta-like 4 (Dll4)/Notch signaling [104] and activates downstream components including the Ras/Raf/MEK, PI3K/AKT, and p38/MAPK/HSP27 pathways [105]. Our data suggest glial *betaPix* as an important factor in vascular integrity development. Together with previous studies, *betaPix-Pak1-stathmin* signaling regulates glial growth and differentiation[32] and betaPix regulates *Vegfaa* secretion *via* downstream transcription factors *Zfhx3/4*. Thus, this work presents a novel glial betaPix signaling in regulating zebrafish BBB development.

Basement membrane is a non-cellular component consisting of several extracellular matrix (ECM) proteins, which laminins are the most abundant ones, while collagen IV, fibronectin, and perlecan serve as hub for structural supports, anchoring and intercellular communication. Components of basement membrane are synthesized in surrounding cells with diverse expression patterns [106]. For example, mice with deletion of Collagen IV in either brain microvascular endothelial cells (BMEC)- or pericytes lead to fully penetrant intracerebral haemorrhage, while COL4A1 deletion in astrocytes results in mild haemorrhage phenotypes [69]. Differential cell-specific expression pattern of laminin isoforms contribute differently to BBB formation [107]. As

bioRxiv preprint doi: https://doi.org/10.1101/2025.04.08.647738; this version posted April 9, 2025. The copyright holder for this preprint (which was not certified by peer review) is the author/funder, who has granted bioRxiv a license to display the preprint in perpetuity. It is made available under a CC-BY 4.0 International license.

461 astrocytic laminins mediate pericyte differentiation and regulate capillary
462 permeability [108], intercellular interactions with the ECM occur by cell surface integrin
463 receptors. Integrin β1 on endothelial cells are critical during angiogenesis[109]. On the
464 other hand, integrin αvβ8 has glial-specific enrichment which mediate focal adhesion
465 to modulate vascular integrity[17,110,111]. Notably, degradation of ECM and focal
466 adhesions at the perivascular space is responsible for the hemorrhagic phenotypes of
467 *bbh* mutants [17,18]. It would be of great interest to determine whether glial *betaPix*
468 account for ECM breakdown in *bbh* mutants in future studies.
469

bioRxiv preprint doi: https://doi.org/10.1101/2025.04.08.647738; this version posted April 9, 2025. The copyright holder for this preprint (which was not certified by peer review) is the author/funder, who has granted bioRxiv a license to display the preprint in perpetuity. It is made available under a CC-BY 4.0 International license.

Acknowledgements

The authors thank Drs. Bo Zhang, Jiulin Du, Liangyi Chen, Kazu Kikuchi, and Jian Chen for providing fish lines, plasmid clones, and human glial cell lines; the members of Dr. Jing-Wei Xiong's laboratory for helpful discussions and technical assistance; and the National Center for Protein Sciences at Peking University, particularly Dr. Liying Du at the Flow Cytometry Core for technical help on the Beckman Coulter MoFlo XDP; and Dr. Hua Liang at National Biomedical Imaging Center, Peking University for assistance with the Luxendo Multi-View Selective-Plane Illumination Microscopy (Bruker). This work is supported by grants from the National Key R&D Program of China (2019YFA0801602 and 2023YFA1800600); the National Natural Science Foundation of China (32230032 and 31730061).

Declaration of Interest

The authors declare no competing financial interests.

bioRxiv preprint doi: https://doi.org/10.1101/2025.04.08.647738; this version posted April 9, 2025. The copyright holder for this preprint (which was not certified by peer review) is the author/funder, who has granted bioRxiv a license to display the preprint in perpetuity. It is made available under a CC-BY 4.0 International license.

Materials and Methods

Fish maintenance

Zebrafish were raised and handled in accordance with the guidelines of the Peking University Animal Care and Use Committee accredited by the AAALAC.

The *bbh*^{fn40a} mutant was isolated from a large-scale mutagenesis screen of the zebrafish genome at Massachusetts General Hospital, Boston[9]. Tg(*acta2:GFP-Cre*) was purchased from Xinjia Pharmaceutical Technology Co., Ltd (Nanjing, China); Tg(*neurod:EGFP*) were kindly provided by Dr. Bo Zhang (Peking University, China); Tg(*huC:GFP*) were kindly provided by Dr. Liangyi Chen (Peking University, China); Tg(*kdrl:GFP*) [112] and Tg(*kdrl:mCherry*) [113] were described previously.

Cell culture and transfection

U251 and A172 human glioblastoma cell lines, kindly provided by Dr. Jian Chen at Chinese Institute for Brain Research, Beijing, were cultured in high glucose DMEM medium (Hyclone) supplemented with 10% fetal bovine serum and 1% penicillin/streptomycin, at 37°C in 5% CO_2 humidified incubator. The *betaPix* siRNAs and *STMN1* siRNAs were purchased from GenePharma (Shanghai, China). The sequences of the siRNAs are listed in **Table S2**. Transfection was conducted with Lipofectamine 3000 (Invitrogen) at a final siRNA concentration of 30 nM.

mRNA/gRNA synthesis and microinjections

mRNA and gRNA were synthesized as described previously [114]. In brief, linearized

bioRxiv preprint doi: https://doi.org/10.1101/2025.04.08.647738; this version posted April 9, 2025. The copyright holder for this preprint (which was not certified by peer review) is the author/funder, who has granted bioRxiv a license to display the preprint in perpetuity. It is made available under a CC-BY 4.0 International license.

pT3TS-nls-zCas9-nls [115], pXT7-*Cre*, and pXT7-*Zfhx4* plasmid DNA were purified as templates using TIANquick Mini Purification Kit (TIANGEN, DP203, China). Next, *in vitro* transcription reactions were performed using the mMESSAGE mMACHINE T3 (for pT3TS-nls-zCas9-nls) or T7 (for pXT7-*Cre* and pXT7-*Zfhx4*) kits (Life Technologies) according to manufacturer's instructions. Templates for gRNA were generated by complementary annealing and elongation of two oligos. Forward oligo contained a T7 promoter and gRNA target sequence, and reverse oligo contained the universal gRNA scaffold [23]. The resulting double-stranded DNA served as the templates for *in vitro* transcription using HiScribe® T7 High Yield RNA Synthesis Kit (NEB). The sequences of the gRNAs are listed in **Table S3**. For global *betaPix* inactivation, *Cre* mRNA with a working concentration of 200 ng/μL were injected into the *betaPix*$^{ct/ct}$ embryos at one-cell stage. For CRISPR-mediated knockouts, 300 ng/μL Cas9 mRNA and 20-50 ng/μL gRNAs were injected into zebrafish embryos at one-cell stage. For *Zfhx4* rescue experiments, *Zfhx4* mRNA with a working concentration of 400 ng/μL were injected into the *bbh*^{fn40a} mutants or in combination with CRISPR-mediated *betaPix* knockout system at one-cell stage. Injected embryos were scored for mutant phenotypes at 36 or 48 hpf.

Construction of *betaPix* conditional knockout zebrafish

The pZwitch plasmid clone was kindly provided by Dr. Kazu Kikuchi (National Cerebral and Cardiovascular Center Research Institute, Suita, Japan). GSG spacer was added to pZwitch+3 between P2A and TagRFP coding sequences by overlapping primer

bioRxiv preprint doi: https://doi.org/10.1101/2025.04.08.647738; this version posted April 9, 2025. The copyright holder for this preprint (which was not certified by peer review) is the author/funder, who has granted bioRxiv a license to display the preprint in perpetuity. It is made available under a CC-BY 4.0 International license.

pairs. Next, a highly efficient gRNA was found from the fifth intron of *betaPix*. Primer pairs were designed to amplify the left and right homologous arms from the gRNA site for 1000 bp and 24 bp with following modifications: 1) The 5' end of the forward primer of the left homologous arm were added with an *Nhe*1 site and a universal gRNA site which provided an *in vivo* linearization cleavage site; a *Mlu*1 site to the 5' end of the reverse primer of the left arm. 2) Added *EcoR*1 site to the 5' end of the forward primer of the right homologous arm; added *Xho1* site and universal gRNA site to the 5' end of the reverse primer of the right homologous arm. Then we cloned the inverted homologous arms into polyclonal sites of the modified pZwitch+3, and purified plasmid DNA with EndoFree Mini Plasmid Kit (Tiangen, DP118). *In vivo* knock-in system was composed of 300 ng/μL Cas9 mRNA, 50 ng/μL *betaPix*-intron5 gRNA, 50 ng/μL Universal gRNA, and 20 ng/μL donor vector. Microinjected *in vivo* knock-in system into wildtype embryos at one-cell stage. Fish founders were screened for *α*-crystallin reporter expression, raised to adulthood, and re-screened for germline transmission and precise knock-in by Sanger sequencing.

Construction of transgenic reporters

The glial reporter plasmid *gfap*-EGFP [26] was kindly provided by Dr Jiulin Du (Shanghai Institute for Biological Sciences, Shanghai, China). The *gfap* promoter was used to establish Tg(*gfap:GFP-Cre*) plasmid. The *stmn1b* coding sequences were amplified from wild-type zebrafish cDNA library, which were used to establish Tg(*gfap:GFP-stmn1b*) plasmid.

bioRxiv preprint doi: https://doi.org/10.1101/2025.04.08.647738; this version posted April 9, 2025. The copyright holder for this preprint (which was not certified by peer review) is the author/funder, who has granted bioRxiv a license to display the preprint in perpetuity. It is made available under a CC-BY 4.0 International license.

Transgenic reporters were generated by using *Tol2*-based transgenesis [116]. In brief, 100 ng/μL *Tol2* transposase mRNA in combination with 20 ng/μL donor plasmid DNA were co-injected into the embryos at one-cell stage. Transgenic founders were screened for specific transgenic GFP expression, raised to adulthood, and re-screened for germline transmission.

Inhibitor treatment

IPA-3 (Proteintech, CM05727) were dissolved in DMSO to form a 10 mM stock, and then diluted with E3 medium to 3 μM in 6-well plates. Zebrafish embryos were treated from 24 to 48 hpf, and then washed with E3 medium for phenotype analysis.

***o*-dianisidine staining**

o-dianisidine staining was performed as described previously [18]. In brief, embryos were dechorionated, anesthetized and incubated in fresh staining solution (0.6 mg/mL *o*-dianisidine, 0.01 M sodium acetate pH4.5, 0.65% H_2O_2 and 40% Ethanol) for 20 minutes in dark. Washed three times with methanol, and performed benzyl alcohol/benzyl benzoate (BABB) tissue clearing before imaging with stereo microscope (Leica, 160F).

Whole-mount *in situ* hybridization (WISH)

Whole-mount *in situ* RNA hybridization was performed as described previously [117]. Antisense probes were synthesized using a digoxigenin RNA labeling kit (Roche,

bioRxiv preprint doi: https://doi.org/10.1101/2025.04.08.647738; this version posted April 9, 2025. The copyright holder for this preprint (which was not certified by peer review) is the author/funder, who has granted bioRxiv a license to display the preprint in perpetuity. It is made available under a CC-BY 4.0 International license.

11277073910). Primer sequences for all WISH probes used in this paper are provided in **Table S4**.

Quantitative real-time RT-PCR

Total RNA was isolated from embryos using Trizol (invitrogen) and cDNA was generated using HiScript® III RT SuperMix (Vazyme) according to the manufacturer's instruction. Quantitative real-time PCR was performed using Lightcycler (Roche) and ChamQ SYBR qPCR Master Mix (Vazyme). Primer sequences are listed in Supplementary Materials **Table S5**. Gene expression level was normalized against GAPDH level.

Light-sheet fluorescence microscopy imaging

Light-sheet microscopy imaging was performed as described previously [118]. In brief, transgenic zebrafish embryos were collected and maintained at 28.5°C. At the required developmental stages, the embryos were carefully dechorionated, paralyzed with tricaine, and transferred into 1% ultrapure low melting point agarose (16520-050; Invitrogen). The embryo was then drawn into a glass tube in top-down position using a 1 mL syringe with an 18G blunt needle. After agarose coagulation, a wire was inserted from bottom to push the agarose with embryo upwards, removed excess agar until the head area is exposed from the top of the glass tube. Finally, the glass tube was fixed in a sample holder for subsequent imaging.

Imaging was carried out with Luxendo Multi-View Selective-Plane Illumination

bioRxiv preprint doi: https://doi.org/10.1101/2025.04.08.647738; this version posted April 9, 2025. The copyright holder for this preprint (which was not certified by peer review) is the author/funder, who has granted bioRxiv a license to display the preprint in perpetuity. It is made available under a CC-BY 4.0 International license.

Microscopy (Bruker). Optical calibrations were adjusted according to the instruction manual.

The optical plates are emitted from two Nikon CFI Plan Fluor 10x W 0.3 NA immersion objectives in opposite directions. The detection is completed by two Olympus 20x 1.0 NA immersion lenses. The parameters are set as follows: the green fluorescence channel uses a laser of 488 nm coupled with BP497-554 filter, the red fluorescent channel uses laser 561 nm coupled with BP580-627 filter, with an exposure time of 100 ms, a delay of 11 ms, a line mode of 50 px, and z-Stack interval of 3 μm. The raw data were stored in H5 file format, processed into TIFF format and merged Multi-View dataset using MATLAB software. After pre-processing, multi-fluorescence channels were merged in ImageJ, and 3D visualization and measurement were performed by Imaris.

Single-cell RNA sequencing

For knockout samples, 300 ng/μL Cas9 mRNA and a mixture of number 1 to 4 *betaPix* gRNAs with 50 ng/μL each were co-injected into wildtype embryos at one-cell stage. Injection with equivalent concentration of Cas9 mRNA with PBS served as siblings. After microinjection, embryos were collected and maintained at 28.5°C. At 24 or 48 hpf, zebrafish were dechorionated, paralyzed and transferred onto agarose plate. Heads were harvested with dissecting scissors in cold sterile 1X PBS with pooling 200 heads for each group. Heads were then dissociated in 900 μL Accutase cell detachment solution (Sigma-Aldrich, A6964) at 28.5°C for 3 hours and re-suspended by pipetting every 30 min. Once digestion was complete, 100 μL FBS was added to cell suspension

bioRxiv preprint doi: https://doi.org/10.1101/2025.04.08.647738; this version posted April 9, 2025. The copyright holder for this preprint (which was not certified by peer review) is the author/funder, who has granted bioRxiv a license to display the preprint in perpetuity. It is made available under a CC-BY 4.0 International license.

and centrifuged at 4℃, 500 g for 3 min. The cells were gently re-suspended in cold 500 μL 2.5% FBS in 1X PBS and filtered through a 40 μm strainer. PI and Hoechst33342 were stained for distinguishing living cells. The single, living cells were sorted by Aria SORP (BD biosciences) into 1.5 ml tubes. The cell counts and vitality were verified by AOPI staining coupled with an Automated Cell Counter (Countstar BioTech). Single cells were barcoded with Chromium Next GEM Single Cell 3 'Reagent Kits V3.1 kit (10x Genomics, 1000269) in 10× Chromium Controller (10× Genomics). After qualified by peak shapes, fragment size and tailing with Fragment Analyzer System kit (Agilent Technologies, DNF-915), single-cell transcriptome libraries were sequenced via Illumina High Throughput Sequencing PE150 (Novogene, Beijing). The sequencing data were analyzed using the CellRanger-6.1.1 (10x Genomics) and mapped to reference genome GRCz11-GRCz11.103.

Cells were excluded from subsequent analyses under the following conditions: when the number of expressed genes was less than 500, when there were abnormally high counts of UMIs or genes (outliers of a normal distribution), or when the mitochondrial content exceeded 9%. Unsupervised clustering was performed using Seurat (version: 4.0.2) with a resolution of 2.5, resulted in 71 cell populations and further annotated into 24 zebrafish major cranial cell types. Differential expression analysis in Seurat v4 was used to identify cluster/cell type markers by Wilcoxon rank sum test.

Scratch assay

U251 cells were planted into culture plate and performed transfection at the desired

bioRxiv preprint doi: https://doi.org/10.1101/2025.04.08.647738; this version posted April 9, 2025. The copyright holder for this preprint (which was not certified by peer review) is the author/funder, who has granted bioRxiv a license to display the preprint in perpetuity. It is made available under a CC-BY 4.0 International license.

density. At 24 hours post-transfection, we vertically scratched monolayer cells by using a 200 μL pipette tip. Washed the cells three times with PBS, then replaced with serum-free culture medium for further culture. Stereo fluorescence microscopy (Leica, 160F) was used to document the scratch size at 0 hours, 18 and 24 hours. Images were processed by ImageJ.

Immunostaining

For assessing tubulin expression, U251 cells were planted into chamber slides (Saining, 1093000) and transfected at the desired density. At 24 hours post-transfection, washed the cells once on ice with pre-cooled PBS, then fixed with pre-cooled methanol at -20℃ for 20 minutes. The fixed cells were permeabilized with pre-cooled acetone at -20℃ for 1 minute. Removed acetone, incubated 0.5% BSA/PBS blocking solution at room temperature for 15 minutes. Cells were then incubated with 1:200 anti-α-tubulin mouse monoclonal antibody (EASYBIO, BE0031) at 37℃ for 45 minutes. After rinsing once with PBS, cells were incubated with 1:400 Alexa Fluor™ 488 goat anti-mouse IgG (H+L) secondary antibody (Invitrogen, A11029) at 37℃ for another 45 minutes. Washed three times with PBS, and sealed with Mounting Medium with DAPI (ZSGB Bio, ZLI-9557). Images were acquired by upright fluorescence microscopy (Leica, DM5000B) at 40× magnification, and processed by ImageJ.

Statistical analysis

Statistical analysis was performed using Graphpad Prism 6. The statistical significance

bioRxiv preprint doi: https://doi.org/10.1101/2025.04.08.647738; this version posted April 9, 2025. The copyright holder for this preprint (which was not certified by peer review) is the author/funder, who has granted bioRxiv a license to display the preprint in perpetuity. It is made available under a CC-BY 4.0 International license.

of differences between the two groups was determined by the independent unpaired Student's t-test. Among three or more groups, one-way ANOVA analysis coupled with Dunnett's test were used. All data are presented as the mean ± SEM. *P* value <0.05 indicates significant, with individual *P* values mentioned in the figure/figure legends.

bioRxiv preprint doi: https://doi.org/10.1101/2025.04.08.647738; this version posted April 9, 2025. The copyright holder for this preprint (which was not certified by peer review) is the author/funder, who has granted bioRxiv a license to display the preprint in perpetuity. It is made available under a CC-BY 4.0 International license.

Figure Legends

Figure 1. Generation of *betaPix* conditional trap (*betaPix^{ct}*) allele by an homologous recombination (HDR)-mediated knock-in method.

(A) Schematic diagram illustrates the HDR-mediated *Zwitch* strategy for generating zebrafish knock-in allele at the *betaPix* locus.

(B) Genomic PCR analysis of the F_1 embryos confirming the right *Zwitch* insertions.

(C) Sanger sequencing confirming the junction of *betaPix^{ct}* (after HDR-mediated insertion) or *betaPix^{m}* (after Cre-mediated inversion) that are highlighted by RED lines in (A).

(D) Representative stereomicroscopy images of erythrocytes stained with o-dianisidine in *betaPix$^{ct/ct}$* and *betaPix$^{m/m}$* embryos at 48 hpf. Brain hemorrhages, indicated with arrows, in Cre mRNA-injected embryos (*betaPix$^{m/m}$*). Lateral views, anterior to the left.

(E) Quantification of hemorrhagic parameters in (D). Left panel showing hemorrhage percentages with each dot representing an individual experiment (n>100 each), and right panel showing hemorrhage areas with each dot representing one embryo.

(F) qRT-PCR analysis showing the expression of *betaPix*, *RFP* and *alphaPix* in *betaPix$^{ct/ct}$*, *betaPix$^{ct/m}$*, and *betaPix$^{m/m}$* embryos at 48 hpf. Each dot represents one embryo. cryaa, αA-crystallin; PA, polyadenylation signal; SA, splice acceptor; T2A, T2A self-cleaving peptide.

bioRxiv preprint doi: https://doi.org/10.1101/2025.04.08.647738; this version posted April 9, 2025. The copyright holder for this preprint (which was not certified by peer review) is the author/funder, who has granted bioRxiv a license to display the preprint in perpetuity. It is made available under a CC-BY 4.0 International license.

Figure 2. *betaPix*$^{m/m}$ mutant have brain hemorrhages, central artery defects and abnormal glial structure that was partially rescued by Pak1 inhibitor IPA3 treatment.

(A) Left panel showing the maximum intensity projection of the glial structures in the hindbrain of *betaPix*$^{ct/ct}$ and *betaPix*$^{m/m}$ embryos at 48 hpf. Lateral view, anterior to left. Middle panel showing representative optical sections and right panel showing the higher magnifications of boxed area, presenting atypical glial structures with disoriented arrangements (yellow arrows) in *betaPix*$^{m/m}$ embryos.

(B) Quantification of glial parameters in (A). Left panel showing the average glia length, and right panel showing glia length index normalized to individual head length, which each dot represents one embryo.

(C) Whole-mount RNA *in situ* hybridization revealed *nestin* and *pax2a* expression pattern in *betaPix*$^{ct/ct}$ and *betaPix*$^{m/m}$ embryos at 48 hpf. Dorsal view, anterior to the left.

(D) Optical sections of glial structure (green) and blood vessels (magenta) in the heads of siblings and CRISPR-mediated *betaPix* F_0 knockout embryos. Arteries in the hindbrain of *betaPix* KO mutants had developmental defects (white arrowheads), showing shorter distance between basilar artery (BA) and glial cell bodies.

(E) 3D reconstruction of the sox2-positive precursors (green) and vasculatures (magenta) in the heads of siblings and CRISPR-mediated *betaPix* F_0 knockout

bioRxiv preprint doi: https://doi.org/10.1101/2025.04.08.647738; this version posted April 9, 2025. The copyright holder for this preprint (which was not certified by peer review) is the author/funder, who has granted bioRxiv a license to display the preprint in perpetuity. It is made available under a CC-BY 4.0 International license.

embryos at 48 hpf. Box areas are shown in higher magnifications at the middle panels, with optical sections shown in the right panels. Arrows indicate CtA with enlarged perivascular space.

(F) Representative stereomicroscopy images of *o*-dianisidine staining of *betaPix*$^{ct/ct}$ and *betaPix*$^{m/m}$ embryos at 48 hpf that were treated with DMSO or PAK inhibitor IPA3. Brain hemorrhages indicated with the arrows.

(G) Quantification of brain hemorrhagic parameters in (F).

(H) 3D reconstruction of the glial structure (green) and vasculature (magenta) in the heads of *betaPix*$^{ct/ct}$ and *betaPix*$^{m/m}$ embryos at 48 hpf treated with DMSO or IPA3. Lateral view, anterior to left. Defects in CtAs (white arrows) and glia (yellow arrows) shown in *betaPix*$^{m/m}$ embryos treated with DMSO or IPA3.

(I) Quantification of CtA parameters in (H).

(J) Quantification of glia parameters in (H).

Figure 3. Glial-specific *betaPix* knockouts recapture global *betaPix* mutant phenotypes.

(A) Representative stereomicroscopy images of erythrocytes stained with *o*-dianisidine in *betaPix*$^{ct/ct}$ siblings and *gfap:GFP-Cre*; *betaPix*$^{ct/ct}$ mutant embryos treated with DMSO or IPA3 at 48 hpf. Brain hemorrhages indicated with arrows in glial-specific *betaPix* knockouts. Lateral view with anterior to the left.

bioRxiv preprint doi: https://doi.org/10.1101/2025.04.08.647738; this version posted April 9, 2025. The copyright holder for this preprint (which was not certified by peer review) is the author/funder, who has granted bioRxiv a license to display the preprint in perpetuity. It is made available under a CC-BY 4.0 International license.

(B) 3D reconstruction of the vasculatures (magenta) in the heads at 48 hpf, showing lateral view with anterior to the left. The box areas are shown in higher magnifications of brain vasculatures at the right panels. CtA defects (yellow arrows) were evident in *gfap:GFP-Cre*; *betaPix*$^{ct/ct}$ mutant embryos.

(C) Quantification of brain hemorrhages (A) and CtA parameters (B). Left panel showing hemorrhage percentages with each dot representing an individual experiment (n>100 each). Middle panel showing hemorrhage areas with each dot representing one embryo. Right panel showing CtA length index normalized to individual head length, with each dot representing one embryo.

Figure 4. Single cell transcriptome reveals that a subcluster of glial progenitor and stathmin family members are associated with *betaPix* mutation.

(A) Experimental strategy for single cell RNA sequencing of embryonic heads from wild-type siblings and *betaPix* CRISPR mutants at 1 dpf and 2 dpf.

(B) UMAP visualization and clustering of cells labeled by cell type. Four samples were aggregated and analyzed together.

(C) Proportions of 24 cell clusters were differentially distributed among four sample groups. ctrl_1d, PBS-injected siblings at 1 dpf; ko_1d, *betaPix* CRISPR mutants at 1 dpf; ctrl_2d, PBS-injected siblings at 2 dpf; ko_2d, *betaPix* CRISPR mutants at 2 dpf.

(D) Enriched GO terms for differentially expressed genes for progenitor sub-cluster comparing ko_2d to ctrl_2d groups.

bioRxiv preprint doi: https://doi.org/10.1101/2025.04.08.647738; this version posted April 9, 2025. The copyright holder for this preprint (which was not certified by peer review) is the author/funder, who has granted bioRxiv a license to display the preprint in perpetuity. It is made available under a CC-BY 4.0 International license.

(E) Violin plots showing the expression of the stathmin family genes by all cells among four sample groups (left panel) or by progenitor sub-cluster among four sample groups (right panel).

(F) qRT-PCR analysis showing expression of *betaPix*, *stmn1a*, *stmn1b*, *stmn4l* and *ppfia3* in glia of FACS-sorted *betaPix*$^{ct/ct}$ siblings and *betaPix*$^{m/m}$ mutants at 48 hpf. Each dot represents cells sorted from one embryo.

(G) qRT-PCR analysis showing expression of *betaPix*, *stmn1a*, *stmn1b*, *stmn4l* and *ppfia3* in glia of FACS-sorted *betaPix*$^{ct/ct}$ siblings and *gfap:GFP-Cre*; *betaPix*$^{ct/ct}$ mutants at 48 hpf. Each dot represents cells sorted from one embryo.

(H) Whole-mount RNA *in situ* hybridization revealing down-regulation of *stmn1a*, *stmn1b* and *stmn4l* in *betaPix*$^{ct/ct}$ siblings and *gfap:GFP-Cre*; *betaPix*$^{ct/ct}$ mutant embryos at 48 hpf.

Figure 5. Stathmin acts downstream of *betaPix* in glial migration *via* regulating tubulin polymerization.

(A) Whole-mount RNA *in situ* hybridization showing that *stmn1a, stmn1b and stmn4l* expression in *gfap:GFP-Cre*; *betaPix*$^{ct/ct}$ embryos were partially rescued by Pak1 inhibitor IPA3 treatment at 48 hpf. Dorsal views, anterior to the left.

bioRxiv preprint doi: https://doi.org/10.1101/2025.04.08.647738; this version posted April 9, 2025. The copyright holder for this preprint (which was not certified by peer review) is the author/funder, who has granted bioRxiv a license to display the preprint in perpetuity. It is made available under a CC-BY 4.0 International license.

(B) qRT-PCR analysis showing that *stmn1a* and *stmn4l* expression were rescued in *gfap:GFP-Cre*; *betaPix*$^{ct/ct}$ mutants by IPA3 treatment at 48 hpf. Each dot represents one embryo.

(C) Representative stereomicroscopy images of erythrocytes stained with *o*-dianisidine in siblings and *stmn1a/1b/4l* CRISPR mutants at 48 hpf. Brain hemorrhages, indicated with arrows, appeared in *stmn1a/1b/4l* mutants. Lateral views with anterior to the left.

(D) Quantification of hemorrhagic parameters in (C). Left panel showing hemorrhage percentages with each dot representing an individual experiment (n>100 each), and right panel showing hemorrhage areas with each dot representing one embryo.

(E) 3D reconstruction of glial structure (green) and vasculature (magenta) in the heads at 48 hpf. Lateral view with anterior to the left. CtA defects (white arrows) appeared in *stmn1a/1b/4l* mutants.

(F) Quantification of CtA and glia parameters in (E). Length index normalized to individual head length, with each dot representing one embryo.

(G) Representative stereomicroscopy images of erythrocytes stained with *o*-dianisidine in *bbh*^{fn40a} and *bbh*^{fn40a}; Tg(*gfap:GFP-stmn1b*) embryos at 48 hpf. Brain hemorrhages, indicated with arrows, decreased in *bbh*^{fn40a} mutants with glia-specific overexpression of *stmn1b*, compared with *bbh*^{fn40a} mutant siblings. Lateral views with anterior to the left.

bioRxiv preprint doi: https://doi.org/10.1101/2025.04.08.647738; this version posted April 9, 2025. The copyright holder for this preprint (which was not certified by peer review) is the author/funder, who has granted bioRxiv a license to display the preprint in perpetuity. It is made available under a CC-BY 4.0 International license.

(H) Quantification of hemorrhagic parameters of (G). Left panel showing hemorrhage percentages with each dot representing an individual experiment (n>100 each), and right panel showing hemorrhage area with each dot representing one embryo.

(I) 3D reconstruction of the *gfap:GFP-stmn1b* overexpression (green) and vasculature (magenta) in the heads of *bbh*^{fn40a} siblings and *bbh*^{fn40a}; Tg(*gfap:GFP-stmn1b*) mutants at 48 hpf. Lateral view with anterior to left. White arrows indicate CtA defects.

(J) Quantification of CtA and glia parameters in (I). Length index normalized to individual head length, with each dot representing one embryo.

(K) Representative stereomicroscopy images of U251 cells at 0 and 24 hours after wounding. U251 cells were transfected with negative control siRNA or *betaPIX* siRNA separately, in combination with pcDNA3.1 vector, *betaPIX* overexpression plasmid, and *STMN1* overexpression plasmid. The wound edges are highlighted by dashed lines, with arrow lines indicating the wound width.

(L) Quantification of wound closure in (K), showing $^{*}P<0.05$, $^{***}P<0.005$ compared to negative control siRNA with empty vector transfection. $^{\#\#}P<0.01$, $^{\#\#\#}P<0.005$ compared to *betaPix* knockdown with empty vector transfection.

(M) Representative immunofluorescence image of alpha-tubulin and DAPI signals in U251 cells. U251 cells were transfected with negative control siRNA or *betaPIX* siRNA separately, in combination with pcDNA3.1 vector, *betaPIX* overexpression plasmid, and *STMN1* overexpression plasmid. Box

bioRxiv preprint doi: https://doi.org/10.1101/2025.04.08.647738; this version posted April 9, 2025. The copyright holder for this preprint (which was not certified by peer review) is the author/funder, who has granted bioRxiv a license to display the preprint in perpetuity. It is made available under a CC-BY 4.0 International license.

areas are shown in higher magnifications. Arrows indicate protrusions at the cell periphery.

(N) Quantification of cell percentages with protrusions in (M). $^{***}P<0.005$ compared to negative control siRNA with empty vector transfection. $^{\#}P<0.05$, $^{\#\#}P<0.01$ compared to *betaPix* knockdown with empty vector transfection.

Figure 6. *Zfhx3/4* acts downstream of *betaPix* to regulate vascular integrity development.

(A) Whole-mount RNA *in situ* hybridization revealing that *vegfaa* decreased in *bbh*^{fn40a} mutants compared with siblings at 36 hpf. Lateral views with anterior to the left. Arrows indicate *vegfaa* expression in the CtAs.

(B) qRT-PCR analysis revealing that *ZFHX3*, *ZFHX4 and* VEGFA decreased in U251 cells transfected with *betaPIX* siRNA, which were rescued by *betaPIX* overexpression.

(C) Whole-mount RNA *in situ* hybridization showing that *vegfaa* decreased in CRISPR-mediated *zfhx3/4* F_0 knockout embryos at 36 hpf. Lateral views with anterior to the left. Arrows indicate *vegfaa* expression in the CtAs.

(D) Representative stereomicroscopy images of erythrocytes stained with *o*-dianisidine in siblings and CRISPR-mediated *zfhx3/4* F_0 knockout embryos at 48 hpf. Arrows indicated brain hemorrhages in the knockout brains. Lateral views with anterior to the left.

bioRxiv preprint doi: https://doi.org/10.1101/2025.04.08.647738; this version posted April 9, 2025. The copyright holder for this preprint (which was not certified by peer review) is the author/funder, who has granted bioRxiv a license to display the preprint in perpetuity. It is made available under a CC-BY 4.0 International license.

(E) Quantification of hemorrhagic parameters in (D). Left panel showing hemorrhage percentages with each dot representing an individual experiment (n>100 each), and right panel showing hemorrhage areas with each dot representing one embryo.

(F) 3D reconstruction of the glial structure (green) and vasculature (magenta) in the hindbrains of siblings and CRISPR-mediated *zfhx3/4* F_0 knockouts at 48 hpf. Lateral view with anterior to the left. White arrows indicate CtA defects in *zfhx3/4* knockout embryos.

(G) Quantification of CtA and glia length parameters of (F). Length index normalized to individual head length, with each dot representing one embryo.

(H) Representative stereomicroscopy images of erythrocytes stained with *o*-dianisidine in CRISPR-mediated *betaPix* F0 knockout embryos with or without *zfhx4* mRNA injection at 48 hpf. Arrows indicate brain hemorrhages. Lateral views with anterior to the left.

(I) Quantification of hemorrhagic parameters in (H). Left panel showing hemorrhage percentages with each dot representing an individual experiment (n>100 each), and right panel showing hemorrhage area with each dot representing one embryo.

(J) 3D reconstruction of the glial structure (green) and vasculature (magenta) in CRISPR-mediated *betaPix* F_0 knockout embryos with or without *zfhx4* mRNA injection at 48 hpf. White arrows indicate CtAs and yellow arrows indicate glia.

bioRxiv preprint doi: https://doi.org/10.1101/2025.04.08.647738; this version posted April 9, 2025. The copyright holder for this preprint (which was not certified by peer review) is the author/funder, who has granted bioRxiv a license to display the preprint in perpetuity. It is made available under a CC-BY 4.0 International license.

(K) Quantification of CtA and glia length parameters in (J). Length index normalized to individual head length, with each dot representing one embryo.

(L) Whole-mount RNA *in situ* hybridization revealed that *zfhx4* and *vegfaa* decreased in CRISPR-mediated *betaPix* F_0 knockout embryos at 36 hpf, which were rescued by *zfhx4* mRNA injection. Lateral views with anterior to the left. Arrows indicate hindbrain regions.

(M) Dot plots of several angiogenesis-associated genes expression in endothelial cell cluster. Dot size indicates the percentage of cells with gene expression, and dot color represents the average gene expression level.

Figure 7. Working Model on the function of glial *betaPix* in zebrafish vascular integrity development of the hindbrain. *betaPix* is enriched in glia and regulates the PAK1-Stathmin axis on microtublin stabilization, thus fine-tuning glial cell migration and their interactions with vanscular endothelial cells; and in paralelle, betaPix may also regulate Zfhx3/4-Vegfaa signaling in glia, which then modulates angiogenesis during cerebral vessel development and maturation. Deletion of *betaPix* affects glial cell migration and interaction with cerebral endothelial cells. MT, Microtubule.

Figure S1. Generation of betaPix conditional trap (*betaPix*^{ct}) allele by an HDR-mediated knock-in method.

(A) Sanger sequencing results of the original pZwitch (+3) and the modified vector with glycine-serine-glycine spacer (GSG) in front of the 2A peptide.

bioRxiv preprint doi: https://doi.org/10.1101/2025.04.08.647738; this version posted April 9, 2025. The copyright holder for this preprint (which was not certified by peer review) is the author/funder, who has granted bioRxiv a license to display the preprint in perpetuity. It is made available under a CC-BY 4.0 International license.

(B) Sanger sequencing results of the genomic PCR products at both junction sites from the *betaPix*^{ct} F_1 offspring showing the correct knock-in in the betaPix locus.

(C) The screening process for *betaPix*^{ct} knock-in zebrafish showing about 1% efficiency with correct homologous recombinations.

(D) Representative stereomicroscopy images of *o*-dianisidine staining in *bbh*^{fn40a} embryos at 48 hpf. Lateral view, anterior to the left in left panel; Dorsal view, anterior to the top in right panel.

(E) Quantification of hemorrhagic parameters in (D). Left panel showing hemorrhage percentages with each dot representing an individual experiment (n>100 each), and right panel showing hemorrhage areas with each dot representing one embryo.

(F) 3D reconstruction of the *betaPix* expression (magenta) in *betaPix*$^{ct/+}$ brains of embryos microinjected with PBS or *Cre* mRNA at 24 hpf, 48 hpf, 72 hpf and 144 hpf. Cre-induced *RFP* expression indicates successful inversion of gene trap system (arrows). Dorsal view, anterior to the top.

(G) 3D reconstruction of the *neurod1* transgenic expression (green) and *betaPix* expression (magenta) in *betaPix*$^{ct/+}$ brains of embryos microinjected with PBS or *Cre* mRNA at 24 hpf, 48 hpf, 72 hpf and 144 hpf. Cre-induced *RFP* expression indicates successful inversion of gene trap system (arrows), marking strong *betaPix* expression at the midbrain hindbrain boundary (MHB), and milder expression at hindbrain at early stages. At 144 hpf, *betaPix*

bioRxiv preprint doi: https://doi.org/10.1101/2025.04.08.647738; this version posted April 9, 2025. The copyright holder for this preprint (which was not certified by peer review) is the author/funder, who has granted bioRxiv a license to display the preprint in perpetuity. It is made available under a CC-BY 4.0 International license.

903 expresses ubiquitously in the brain, outlining the cerebellum (arrowheads).
904 Dorsal view, anterior to the top.
905
906 **Figure S2. *betaPix*$^{m/m}$ mutant had brain hemorrhages, central arteries defects,**
907 **and abnormal glial structure.**
908 (A) 3D reconstruction of the vasculature (green) in the heads with lateral view,
909 anterior to left. Endogenous *betaPix* expression (magenta) only shown in Cre
910 mRNA-injected mutant embryos. The box areas are shown in higher
911 magnifications of vasculatures at the right panels. Central arteries (CtA)
912 defects (white arrows) were evident in *betaPix*$^{m/m}$ embryos at 48 hpf. Arrow
913 lines indicating the CtA length.
914 (B) Quantification of CtA parameters in (A). Left panel showing the average CtA
915 length, and right panel showing the CtA length index normalized to individual
916 head length, with each dot representing one embryo.
917 (C) 3D reconstruction of the glia structure. Box areas showing higher
918 magnifications of glia at the right panels. D, dorsal; V, ventral. Arrow lines
919 indicating the glia length.
920
921 **Figure S3. CRISPR-mediated *betaPix* F_0 knockouts had similar phenotypes as**
922 ***betaPix*$^{m/m}$ mutants.**
923 (A) Schematic diagram illustrates guide RNA sites for CRISPR-mediated *betaPix*
924 F_0 knockout.

bioRxiv preprint doi: https://doi.org/10.1101/2025.04.08.647738; this version posted April 9, 2025. The copyright holder for this preprint (which was not certified by peer review) is the author/funder, who has granted bioRxiv a license to display the preprint in perpetuity. It is made available under a CC-BY 4.0 International license.

925 (B) qRT-PCR revealing that *betaPix* decreased in CRISPR-mediated *betaPix* F_0
926 knockout embryos compared with wild-type siblings at 48 hpf. Each dot
927 represents one embryo.
928 (C) Maximal intensity projection of the glial structure of the hindbrains in siblings
929 and CRISPR-mediated *betaPix* F_0 knockouts at 48 hpf, lateral view with
930 anterior to left.
931 (D) Whole-mount RNA *in situ* hybridization revealing up-regulated *nestin* and
932 down-regulated *pax2a* expression in CRISPR-mediated *betaPix* F_0 knockout
933 embryos at 48 hpf. Dorsal view with the anterior to the left.
934 (E) Quantification of hemorrhagic parameters of siblings and CRISPR-mediated
935 *betaPix* F_0 knockout embryos at 48 hpf. Left panel showing percentages of
936 brain hemorrhage with each dot representing an individual experiment (n>100
937 each), and right panel showing hemorrhage areas with each dot representing
938 one embryo.
939 (F) Quantification of CtA parameters of siblings and CRISPR-mediated *betaPix*
940 F_0 knockout embryos at 48 hpf. Left panel showing average CtA length, and
941 right panel showing CtA length index normalized to individual head length,
942 with each dot representing one embryo.
943 (G) Quantification of glial parameters of siblings and CRISPR-mediated *betaPix*
944 F_0 knockout embryos at 48 hpf. Left panel showing average glia length, and
945 right panel showing glia length index normalized to individual head length,
946 with each dot representing one embryo.

bioRxiv preprint doi: https://doi.org/10.1101/2025.04.08.647738; this version posted April 9, 2025. The copyright holder for this preprint (which was not certified by peer review) is the author/funder, who has granted bioRxiv a license to display the preprint in perpetuity. It is made available under a CC-BY 4.0 International license.

947 **Figure S4. Generating glial-specific *betaPix* knockout zebrafish.**

948 (A) Schematic diagram illustrates establishment of glial-specific *betaPix* knockout
949 zebrafish.

950 (B) 3D reconstruction of the heads at 48 hpf with lateral view, anterior to
951 left. Glial-specific *Cre* expression (green) was only shown in *gfap:GFP-Cre*;
952 *betaPix*$^{ct/ct}$ mutant embryos, which overlaps with betaPix:RFP expression
953 (magenta).

954 (C) Genomic PCR analysis of the *betaPix*^{ct}- or *betaPix*^{m}-unique sequences in
955 *betaPix*$^{ct/ct}$ siblings, *gfap:GFP-Cre*; *betaPix*$^{ct/+}$ heterozygous mutants, and
956 *gfap:GFP-Cre*; *betaPix*$^{ct/ct}$ homozygous mutants.

957 (D) qRT-PCR analysis revealing *Cre* expression in *gfap:GFP*-positive glial
958 population and *gfap:GFP*-negative non-glial population that were sorted from
959 *gfap:GFP-Cre*; *betaPix*$^{ct/ct}$ embryos. Each dot represents one embryo.

960 (E) qRT-PCR analysis showing *betaPix, betaPix-RFP* and *alphaPix* expression in
961 *betaPix*$^{ct/ct}$ control siblings and *gfap:GFP-Cre*; *betaPix*$^{ct/ct}$ mutant embryos at
962 48 hpf. Each dot represents one embryo.

963 (F) Whole-mount RNA *in situ* hybridization revealing that *alphaPix* was
964 comparable but *betaPix* decreased in *gfap:GFP-Cre*; *betaPix*$^{ct/ct}$ *mutants*
965 compared with *betaPix*$^{ct/ct}$ siblings at 48 hpf. Lateral view with anterior to the
966 left.

967

bioRxiv preprint doi: https://doi.org/10.1101/2025.04.08.647738; this version posted April 9, 2025. The copyright holder for this preprint (which was not certified by peer review) is the author/funder, who has granted bioRxiv a license to display the preprint in perpetuity. It is made available under a CC-BY 4.0 International license.

Figure S5. Neither endothelial-, neuronal- nor mural-specific deletion of *betaPix* caused brain hemorrhages and abnormal CtA phenotypes.

(A) Representative stereomicroscopy images of *o*-dianisidine staining in *betaPix*$^{ct/ct}$, *kdrl:Cre*; *betaPix*$^{ct/ct}$, *huC:GFP-Cre*; *betaPix*$^{ct/ct}$, and *acta2:GFP-Cre*; *betaPix*$^{ct/ct}$ embryos at 48 hpf.

(B) Quantification of hemorrhage parameters in (A).

(C) 3D reconstruction of the vasculature of *betaPix*$^{ct/ct}$, *kdrl:Cre*; *betaPix*$^{ct/ct}$, *huC:GFP-Cre*; *betaPix*$^{ct/ct}$, and *acta2:GFP-Cre*; *betaPix*$^{ct/ct}$ embryos at 48 hpf. Lateral view with anterior to left. The boxed areas of the hindbrains are shown in higher magnifications at the right panels.

(D) Quantification of CtA parameters in (C).

Figure S6. Glial progenitor sub-cluster of *betaPix* knockouts has down-regulation of *stathmin* family members and up-regulation of *pak1* gene.

(A) UMAP visualization and clustering of cells labeled by cell type across four sample groups.

(B) Dot plot of marker genes expression in each cell type. Dot size indicates the percentage of cells expressed, and dot color represents the average expression level.

(C) UMAP feature plots displaying relative expression levels of selected transcripts among four sample groups. Cells are colored by expression level.

bioRxiv preprint doi: https://doi.org/10.1101/2025.04.08.647738; this version posted April 9, 2025. The copyright holder for this preprint (which was not certified by peer review) is the author/funder, who has granted bioRxiv a license to display the preprint in perpetuity. It is made available under a CC-BY 4.0 International license.

Figure S7. CRISPR-mediated *stmn1a/1b/4l* F_0 knockouts have similar but milder phenotypes as *betaPix* knockouts.

(A) qRT-PCR analysis showing that IPA3 treatment rescued *stmn1a* and *stmn4l* expression in CRISPR-mediated *betaPix* F_0 knockouts at 48 hpf. Each dot represents one embryo.

(B) Schematic diagram illustrates 4-guide RNAs mediated F_0 knockout strategy in the loci of *stmn1a*, *stmn1b* and *stmn4l*.

(C) Whole-mount RNA *in situ* hybridization confirming that *stmn1a, stmn1b* and *stmn4l* decreased in CRISPR-mediated *stmn1a/1b/4l* F_0 knockouts at 48 hpf. Dorsal views with anterior to the left.

(D) qRT-PCR analysis confirming that *stmn1a, stmn1b* and *stmn4l* decreased in mutant embryos of CRISPR-mediated *stmn1a/1b/4l* F_0 knockouts at 48 hpf. Each dot represents one embryo.

(E) qRT-PCR analysis confirming that *stmn1a, stmn1b* and *stmn4l* decreased in the FACS-sorted glia of CRISPR-mediated *stmn1a/1b/4l* F_0 knockouts at 48 hpf. Each dot represents sorted cells from one embryo.

(F) Optical sections of glial structure in the hindbrains of siblings and CRISPR-mediated *stmn1a/1b/4l* F_0 knockouts at 48 hpf. Lateral view with anterior to the left. Abnormal glial structures with disoriented arrangements (yellow arrows) in *stmn1a/1b/4l* mutant embryos.

(G) Quantification of average CtA and glial length in Figure 5 (E). Each dot represents one embryo.

bioRxiv preprint doi: https://doi.org/10.1101/2025.04.08.647738; this version posted April 9, 2025. The copyright holder for this preprint (which was not certified by peer review) is the author/funder, who has granted bioRxiv a license to display the preprint in perpetuity. It is made available under a CC-BY 4.0 International license.

(H) Whole-mount RNA *in situ* hybridization revealed that *nestin* increased while *pax2a* decreased in CRISPR-mediated *stmn1a/1b/4l* F_0 knockout embryos at 48 hpf. Dorsal views with anterior to the left.

(I) 3D reconstruction and whole-mount RNA *in situ* hybridization showing that *gfap:GFP-stmn1b* transgenic overexpression rescued glial defects in *bbh*^{fn40a}; Tg(*gfap:GFP-stmn1b*) embryos at 48 hpf. Lateral views with anterior to the left.

(J) Whole-mount RNA *in situ* hybridization showing that *nestin* and *pax2a* were normally expressed in *bbh*^{fn40a}; Tg(*gfap:GFP-stmn1b*) embryos at 48 hpf. Dorsal views with anterior to the left.

(K) Quantification of average CtA and glia length in Figure 5 (I). Each dot represents one embryo.

(L) qRT-PCR analysis confirming the efficacy of *betaPix* transgenic over-expression and *betaPix* siRNA knockdown in U251 cells.

(M) Representative stereomicroscopy images of A172 cells at 0 and 18 hours after wounding. *betaPIX* siRNA treatment decreased A172 cell migration, which were rescued by either *betaPIX* or STMN1 overexpression. The wound edges are highlighted by dashed lines, with arrow lines indicating the wound width.

(N) Quantification of wound closures in (M). $^{**}P<0.01$ compared to negative control siRNA and empty vector transfection. $^{\#\#}P<0.01$, $^{\#\#\#}P<0.005$ compared to *betaPix* knockdown and empty vector transfection.

bioRxiv preprint doi: https://doi.org/10.1101/2025.04.08.647738; this version posted April 9, 2025. The copyright holder for this preprint (which was not certified by peer review) is the author/funder, who has granted bioRxiv a license to display the preprint in perpetuity. It is made available under a CC-BY 4.0 International license.

Figure S8. *Zfhx3/4* acts downstream of *betaPix* to regulate vascular integrity development.

(A) Violin plots showing that *zfhx3* and *zfhx4* decreased in progenitor sub-cluster of *betaPix* knockouts.

(B) qRT-PCR analysis revealing that *zfhx3* and *zfhx4* decreased in FACS-sorted glia of *gfap:GFP-Cre*; *betaPix*$^{ct/ct}$ mutants compared with *betaPix*$^{ct/ct}$ siblings at 48 hpf. Each dot represents the cells sorted from one embryo.

(C) Schematic diagram illustrates 4-guide RNAs mediated F_0 knockout strategy in the *zfhx3* and *zfhx4* loci.

(D) Whole-mount RNA *in situ* hybridization confirming *zfhx3/4* efficiency in CRISPR-mediated *zfhx3/4* F_0 knockout embryos at 48 hpf.

(E) qRT-PCR analysis revealing that *zfhx3*, *zfhx4*, and *vegfaa* decreased in CRISPR-mediated *zfhx3/4* F_0 knockout embryos at 36 hpf.

(F) Whole-mount RNA *in situ* hybridization revealing that *nestin* increased in CRISPR-mediated *zfhx3/4* F_0 knockout embryos at 36 hpf. Arrows indicate the hindbrain regions.

(G) qRT-PCR analysis confirming overexpression of *zfhx4* in CRISPR-mediated *betaPix* F_0 knockout embryos with *zfhx4* mRNA injection at 70% epiboly.

(H) Representative stereomicroscopy images of erythrocytes stained with *o*-dianisidine showing that brain hemorrhages decreased in *bbh*^{fn40a} mutants with zfhx4 mRNA injection at 48 hpf. Arrows indicate brain hemorrhages. Lateral views with anterior to the left.

bioRxiv preprint doi: https://doi.org/10.1101/2025.04.08.647738; this version posted April 9, 2025. The copyright holder for this preprint (which was not certified by peer review) is the author/funder, who has granted bioRxiv a license to display the preprint in perpetuity. It is made available under a CC-BY 4.0 International license.

(I) Quantification of hemorrhagic parameters in (H). Left panel showing hemorrhage percentages with each dot representing an individual experiment (n>100 each), and right panel showing hemorrhage area with each dot representing one embryo.

bioRxiv preprint doi: https://doi.org/10.1101/2025.04.08.647738; this version posted April 9, 2025. The copyright holder for this preprint (which was not certified by peer review) is the author/funder, who has granted bioRxiv a license to display the preprint in perpetuity. It is made available under a CC-BY 4.0 International license.

References

1. Sheth, K.N. (2022). Spontaneous Intracerebral Hemorrhage. New England Journal of Medicine *387*, 1589-1596. doi:10.1056/NEJMra2201449.

2. Chiang, P.T., Tsai, L.K., and Tsai, H.H. (2025). New targets in spontaneous intracerebral hemorrhage. Curr Opin Neurol 38, 10-17. 10.1097/wco.0000000000001325.

3. Thangameeran, S.I.M., Pang, C.Y., Lee, C.H., Tsai, S.T., Hu, W.F., and Liew, H.K. (2023). Experimental animal models and evaluation techniques in intracerebral hemorrhage. Tzu Chi Med J *35*, 1-10. 10.4103/tcmj.tcmj_119_22.

4. Isogai, S., Horiguchi, M., and Weinstein, B.M. (2001). The vascular anatomy of the developing zebrafish: an atlas of embryonic and early larval development. Dev Biol *230*, 278-301. 10.1006/dbio.2000.9995.

5. Buchner, D.A., Su, F., Yamaoka, J.S., Kamei, M., Shavit, J.A., Barthel, L.K., McGee, B., Amigo, J.D., Kim, S., Hanosh, A.W., et al. (2007). pak2a mutations cause cerebral hemorrhage in redhead zebrafish. Proceedings of the National Academy of Sciences *104*, 13996-14001. 10.1073/pnas.0700947104.

6. Jin, S.W., Herzog, W., Santoro, M.M., Mitchell, T.S., Frantsve, J., Jungblut, B., Beis, D., Scott, I.C., D'Amico, L.A., Ober, E.A., et al. (2007). A transgene-assisted genetic screen identifies essential regulators of vascular development in vertebrate embryos. Dev Biol 307, 29-42. 10.1016/j.ydbio.2007.03.526.

bioRxiv preprint doi: https://doi.org/10.1101/2025.04.08.647738; this version posted April 9, 2025. The copyright holder for this preprint (which was not certified by peer review) is the author/funder, who has granted bioRxiv a license to display the preprint in perpetuity. It is made available under a CC-BY 4.0 International license.

7. Hegarty, J.M., Yang, H., and Chi, N.C. (2013). UBIAD1-mediated vitamin K2 synthesis is required for vascular endothelial cell survival and development. Development *140*, 1713-1719. 10.1242/dev.093112.

8. Stainier, D.Y., Fouquet, B., Chen, J.N., Warren, K.S., Weinstein, B.M., Meiler, S.E., Mohideen, M.A., Neuhauss, S.C., Solnica-Krezel, L., Schier, A.F., et al. (1996). Mutations affecting the formation and function of the cardiovascular system in the zebrafish embryo. Development *123*, 285-292.

9. Chen, J.N., van Bebber, F., Goldstein, A.M., Serluca, F.C., Jackson, D., Childs, S., Serbedzija, G., Warren, K.S., Mably, J.D., Lindahl, P., et al. (2001). Genetic steps to organ laterality in zebrafish. Comp Funct Genomics *2*, 60-68. 10.1002/cfg.74.

10. Liu, J., Fraser, S.D., Faloon, P.W., Rollins, E.L., Vom Berg, J., Starovic-Subota, O., Laliberte, A.L., Chen, J.N., Serluca, F.C., and Childs, S.J. (2007). A betaPix Pak2a signaling pathway regulates cerebral vascular stability in zebrafish. Proc Natl Acad Sci U S A 104, 13990-13995. 10.1073/pnas.0700825104.

11. Manser, E., Loo, T.H., Koh, C.G., Zhao, Z.S., Chen, X.Q., Tan, L., Tan, I., Leung, T., and Lim, L. (1998). PAK kinases are directly coupled to the PIX family of nucleotide exchange factors. Mol Cell 1, 183-192. 10.1016/s1097-2765(00)80019-2

12. Zhou, W., Li, X., and Premont, R.T. (2016). Expanding functions of GIT Arf GTPase-activating proteins, PIX Rho guanine nucleotide exchange factors and

bioRxiv preprint doi: https://doi.org/10.1101/2025.04.08.647738; this version posted April 9, 2025. The copyright holder for this preprint (which was not certified by peer review) is the author/funder, who has granted bioRxiv a license to display the preprint in perpetuity. It is made available under a CC-BY 4.0 International license.

GIT-PIX complexes. J Cell Sci *129*, 1963-1974. 10.1242/jcs.179465.

13. Morimoto, K., Tabata, H., Takahashi, R., and Nakajima, K. (2024). Interactions between neural cells and blood vessels in central nervous system development. Bioessays *46*, e2300091. 10.1002/bies.202300091.

14. Grinchevskaya, L.R., Salikhova, D.I., Silachev, D.N., and Goldshtein, D.V. (2024). Neural and Glial Regulation of Angiogenesis in CNS in Ischemic Stroke. Bull Exp Biol Med *177*, 528-533. 10.1007/s10517-024-06219-4.

15. McCarty, J.H. (2009). Cell adhesion and signaling networks in brain neurovascular units. Curr Opin Hematol *16*, 209-214. 10.1097/MOH.0b013e32832a07eb.

16. McCarty, J.H. (2009). Integrin-mediated regulation of neurovascular development, physiology and disease. Cell Adh Migr *3*, 211-215. 10.4161/cam.3.2.7767.

17. Liu, J., Zeng, L., Kennedy, R.M., Gruenig, N.M., and Childs, S.J. (2012). β Pix plays a dual role in cerebral vascular stability and angiogenesis, and interacts with integrin αvβ8. Dev Biol *363*, 95-105. 10.1016/j.ydbio.2011.12.022.

18. Yang, R., Zhang, Y., Huang, D., Luo, X., Zhang, L., Zhu, X., Zhang, X., Liu, Z., Han, J.Y., and Xiong, J.W. (2017). Miconazole protects blood vessels from MMP9-dependent rupture and hemorrhage. Dis Model Mech *10*, 337-348. 10.1242/dmm.027268.

19. Sugimoto, K., Hui, S.P., Sheng, D.Z., and Kikuchi, K. (2017). Dissection of

bioRxiv preprint doi: https://doi.org/10.1101/2025.04.08.647738; this version posted April 9, 2025. The copyright holder for this preprint (which was not certified by peer review) is the author/funder, who has granted bioRxiv a license to display the preprint in perpetuity. It is made available under a CC-BY 4.0 International license.

zebrafish shha function using site-specific targeting with a Cre-dependent genetic switch. Elife *6*. 10.7554/eLife.24635.

20. Ogawa, M., Geng, F.S., Humphreys, D.T., Kristianto, E., Sheng, D.Z., Hui, S.P., Zhang, Y., Sugimoto, K., Nakayama, M., Zheng, D., et al. (2021). Krü ppel-like factor 1 is a core cardiomyogenic trigger in zebrafish. Science *372*, 201-205. 10.1126/science.abe2762.

21. Ogawa, M., and Kikuchi, K. (2024). Generation of Conditional Knockout Zebrafish Using an Invertible Gene-Trap Cassette. Methods Mol Biol *2707*, 205-214. 10.1007/978-1-0716-3401-1_13.

22. Wierson, W.A., Simone, B.W., WareJoncas, Z., Mann, C., Welker, J.M., Kar, B., Emch, M.J., Friedberg, I., Gendron, W.A.C., Barry, M.A., et al. (2019). Expanding the CRISPR Toolbox with ErCas12a in Zebrafish and Human Cells. Crispr j *2*, 417-433. 10.1089/crispr.2019.0026.

23. Wu, R.S., Lam, II, Clay, H., Duong, D.N., Deo, R.C., and Coughlin, S.R. (2018). A Rapid Method for Directed Gene Knockout for Screening in G0 Zebrafish. Dev Cell *46*, 112-125 e114. 10.1016/j.devcel.2018.06.003.

24. Quiñonez-Silvero, C., Hübner, K., and Herzog, W. (2020). Development of the brain vasculature and the blood-brain barrier in zebrafish. Dev Biol *457*, 181-190. 10.1016/j.ydbio.2019.03.005.

25. Deacon, S.W., Beeser, A., Fukui, J.A., Rennefahrt, U.E., Myers, C., Chernoff, J., and Peterson, J.R. (2008). An isoform-selective, small-molecule inhibitor targets the autoregulatory mechanism of p21-activated kinase. Chem Biol *15*,

bioRxiv preprint doi: https://doi.org/10.1101/2025.04.08.647738; this version posted April 9, 2025. The copyright holder for this preprint (which was not certified by peer review) is the author/funder, who has granted bioRxiv a license to display the preprint in perpetuity. It is made available under a CC-BY 4.0 International license.

322-331. 10.1016/j.chembiol.2008.03.005.

26. Bernardos, R.L., and Raymond, P.A. (2006). GFAP transgenic zebrafish. Gene Expr Patterns *6*, 1007-1013. 10.1016/j.modgep.2006.04.006.

27. Kim, C.H., Ueshima, E., Muraoka, O., Tanaka, H., Yeo, S.Y., Huh, T.L., and Miki, N. (1996). Zebrafish elav/HuC homologue as a very early neuronal marker. Neurosci Lett *216*, 109-112. 10.1016/0304-3940(96)13021-4.

28. Raj, B., Wagner, D.E., McKenna, A., Pandey, S., Klein, A.M., Shendure, J., Gagnon, J.A., and Schier, A.F. (2018). Simultaneous single-cell profiling of lineages and cell types in the vertebrate brain. Nature Biotechnology *36*, 442-450. 10.1038/nbt.4103.

29. Raj, B., Farrell, J.A., Liu, J., El Kholtei, J., Carte, A.N., Navajas Acedo, J., Du, L.Y., McKenna, A., Relić, Đ., Leslie, J.M., and Schier, A.F. (2020). Emergence of Neuronal Diversity during Vertebrate Brain Development. Neuron *108*, 1058-1074.e1056. 10.1016/j.neuron.2020.09.023.

30. Farnsworth, D.R., Saunders, L.M., and Miller, A.C. (2020). A single-cell transcriptome atlas for zebrafish development. Dev Biol 459, 100-108. 10.1016/j.ydbio.2019.11.008.

31. Etienne-Manneville, S. (2013). Microtubules in cell migration. Annu Rev Cell Dev Biol *29*, 471-499. 10.1146/annurev-cellbio-101011-155711.

32. Kwon, Y., Jeon, Y.W., Kwon, M., Cho, Y., Park, D., and Shin, J.E. (2020). β Pix-d promotes tubulin acetylation and neurite outgrowth through a PAK/Stathmin1 signaling pathway. PLoS One *15*, e0230814.

bioRxiv preprint doi: https://doi.org/10.1101/2025.04.08.647738; this version posted April 9, 2025. The copyright holder for this preprint (which was not certified by peer review) is the author/funder, who has granted bioRxiv a license to display the preprint in perpetuity. It is made available under a CC-BY 4.0 International license.

10.1371/journal.pone.0230814.

33. Omelchenko, T., Rabadan, M.A., Hernandez-Martinez, R., Grego-Bessa, J., Anderson, K.V., and Hall, A. (2014). beta-Pix directs collective migration of anterior visceral endoderm cells in the early mouse embryo. Genes Dev *28*, 2764-2777. 10.1101/gad.251371.114.

34. Hsu, R.M., Hsieh, Y.J., Yang, T.H., Chiang, Y.C., Kan, C.Y., Lin, Y.T., Chen, J.T., and Yu, J.S. (2014). Binding of the extreme carboxyl-terminus of PAK-interacting exchange factor β (βPIX) to myosin 18A (MYO18A) is required for epithelial cell migration. Biochim Biophys Acta *1843*, 2513-2527. 10.1016/j.bbamcr.2014.06.023.

35. López Tobón, A., Suresh, M., Jin, J., Vitriolo, A., Pietralla, T., Tedford, K., Bossenz, M., Mahnken, K., Kiefer, F., Testa, G., et al. (2018). The guanine nucleotide exchange factor Arhgef7/βPix promotes axon formation upstream of TC10. Scientific Reports *8*, 8811. 10.1038/s41598-018-27081-1.

36. Cheng, K., Chahdi, A., Larabee, S.M., Tolaymat, M., Sundel, M.H., Drachenberg, C.B., Zhan, M., Hu, S., Said, A.H., Shang, A.C., et al. (2023). Muscarinic receptor agonist-induced βPix binding to β-catenin promotes colon neoplasia. Sci Rep *13*, 16920. 10.1038/s41598-023-44158-8.

37. Connor, K., Murray, D.W., Jarzabek, M.A., Tran, N.L., White, K., Dicker, P., Sweeney, K.J., O'Halloran, P.J., MacCarthy, B., Shiels, L.P., et al. (2020). Targeting the RhoGEF βPIX/COOL-1 in Glioblastoma: Proof of Concept Studies. Cancers (Basel) *12*. 10.3390/cancers12123531.

bioRxiv preprint doi: https://doi.org/10.1101/2025.04.08.647738; this version posted April 9, 2025. The copyright holder for this preprint (which was not certified by peer review) is the author/funder, who has granted bioRxiv a license to display the preprint in perpetuity. It is made available under a CC-BY 4.0 International license.

1192 38. Ward, J.D., Ha, J.H., Jayaraman, M., and Dhanasekaran, D.N. (2015). LPA-
1193 mediated migration of ovarian cancer cells involves translocalization of Gαi2
1194 to invadopodia and association with Src and β-pix. Cancer Lett *356*, 382-391.
1195 10.1016/j.canlet.2014.09.030.
1196 39. Bussmann, J., Wolfe, S.A., and Siekmann, A.F. (2011). Arterial-venous
1197 network formation during brain vascularization involves hemodynamic
1198 regulation of chemokine signaling. Development *138*, 1717-1726.
1199 10.1242/dev.059881.
1200 40. Eubelen, M., Bostaille, N., Cabochette, P., Gauquier, A., Tebabi, P., Dumitru,
1201 A.C., Koehler, M., Gut, P., Alsteens, D., Stainier, D.Y.R., et al. (2018). A
1202 molecular mechanism for Wnt ligand-specific signaling. Science *361*.
1203 10.1126/science.aat1178.
1204 41. Pitulescu, M.E., and Adams, R.H. (2014). Regulation of signaling interactions
1205 and receptor endocytosis in growing blood vessels. Cell Adh Migr *8*, 366-377.
1206 10.4161/19336918.2014.970010.
1207 42. Wang, J., Chen, Y., Zeng, Z., Feng, R., Wang, Q., Zhang, Q., Sun, K., Chen,
1208 A.F., Lu, Y., and Yu, Y. (2021). HMGA2 contributes to vascular development
1209 and sprouting angiogenesis by promoting IGFBP2 production. Exp Cell Res
1210 *408*, 112831. 10.1016/j.yexcr.2021.112831.
1211 43. Fu, C., An, N., Liu, J., A, J., Zhang, B., Liu, M., Zhang, Z., Fu, L., Tian, X.,
1212 Wang, D., and Dong, J.T. (2020). The transcription factor ZFHX3 is crucial
1213 for the angiogenic function of hypoxia-inducible factor 1α in liver cancer

bioRxiv preprint doi: https://doi.org/10.1101/2025.04.08.647738; this version posted April 9, 2025. The copyright holder for this preprint (which was not certified by peer review) is the author/funder, who has granted bioRxiv a license to display the preprint in perpetuity. It is made available under a CC-BY 4.0 International license.

cells. J Biol Chem *295*, 7060-7074. 10.1074/jbc.RA119.012131.

44. Gudbjartsson, D.F., Holm, H., Gretarsdottir, S., Thorleifsson, G., Walters, G.B., Thorgeirsson, G., Gulcher, J., Mathiesen, E.B., Njølstad, I., Nyrnes, A., et al. (2009). A sequence variant in ZFHX3 on 16q22 associates with atrial fibrillation and ischemic stroke. Nat Genet *41*, 876-878. 10.1038/ng.417.

45. Soriano-Tárraga, C., Lazcano, U., Giralt-Steinhauer, E., Avellaneda-Gómez, C., Ois, Á., Rodríguez-Campello, A., Cuadrado-Godia, E., Gómez-González, A., Fernández-Sanlés, A., Elosua, R., et al. (2020). Identification of 20 novel loci associated with ischaemic stroke. Epigenome-wide association study. Epigenetics *15*, 988-997. 10.1080/15592294.2020.1746507.

46. Malik, R., Traylor, M., Pulit, S.L., Bevan, S., Hopewell, J.C., Holliday, E.G., Zhao, W., Abrantes, P., Amouyel, P., Attia, J.R., et al. (2016). Low-frequency and common genetic variation in ischemic stroke: The METASTROKE collaboration. Neurology *86*, 1217-1226. 10.1212/wnl.0000000000002528.

47. Kalvaitytė, M., and Balciunas, D. (2022). Conditional mutagenesis strategies in zebrafish. Trends Genet *38*, 856-868. 10.1016/j.tig.2022.04.007.

48. Obermeier, B., Daneman, R., and Ransohoff, R.M. (2013). Development, maintenance and disruption of the blood-brain barrier. Nat Med *19*, 1584-1596. 10.1038/nm.3407.

49. Langen, U.H., Ayloo, S., and Gu, C. (2019). Development and Cell Biology of the Blood-Brain Barrier. Annu Rev Cell Dev Biol *35*, 591-613. 10.1146/annurev-cellbio-100617-062608.

bioRxiv preprint doi: https://doi.org/10.1101/2025.04.08.647738; this version posted April 9, 2025. The copyright holder for this preprint (which was not certified by peer review) is the author/funder, who has granted bioRxiv a license to display the preprint in perpetuity. It is made available under a CC-BY 4.0 International license.

1236 50. Fleming, A., Diekmann, H., and Goldsmith, P. (2013). Functional
1237 characterisation of the maturation of the blood-brain barrier in larval zebrafish.
1238 PLoS One *8*, e77548. 10.1371/journal.pone.0077548.
1239 51. Xie, J., Farage, E., Sugimoto, M., and Anand-Apte, B. (2010). A novel
1240 transgenic zebrafish model for blood-brain and blood-retinal barrier
1241 development. BMC Dev Biol *10*, 76. 10.1186/1471-213x-10-76.
1242 52. Armulik, A., Genove, G., and Betsholtz, C. (2011). Pericytes: developmental,
1243 physiological, and pathological perspectives, problems, and promises. Dev
1244 Cell *21*, 193-215. 10.1016/j.devcel.2011.07.001.
1245 53. Armulik, A., Genové, G., Mäe, M., Nisancioglu, M.H., Wallgard, E., Niaudet,
1246 C., He, L., Norlin, J., Lindblom, P., Strittmatter, K., et al. (2010). Pericytes
1247 regulate the blood-brain barrier. Nature *468*, 557-561. 10.1038/nature09522.
1248 54. Bell, R.D., Winkler, E.A., Sagare, A.P., Singh, I., LaRue, B., Deane, R., and
1249 Zlokovic, B.V. (2010). Pericytes control key neurovascular functions and
1250 neuronal phenotype in the adult brain and during brain aging. Neuron *68*, 409-
1251 427. 10.1016/j.neuron.2010.09.043.
1252 55. Daneman, R., Zhou, L., Kebede, A.A., and Barres, B.A. (2010). Pericytes are
1253 required for blood-brain barrier integrity during embryogenesis. Nature *468*,
1254 562-566. 10.1038/nature09513.
1255 56. Antonelli-Orlidge, A., Saunders, K.B., Smith, S.R., and D'Amore, P.A. (1989).
1256 An activated form of transforming growth factor beta is produced by
1257 cocultures of endothelial cells and pericytes. Proc Natl Acad Sci U S A *86*,

bioRxiv preprint doi: https://doi.org/10.1101/2025.04.08.647738; this version posted April 9, 2025. The copyright holder for this preprint (which was not certified by peer review) is the author/funder, who has granted bioRxiv a license to display the preprint in perpetuity. It is made available under a CC-BY 4.0 International license.

4544-4548. 10.1073/pnas.86.12.4544.

57. Dohgu, S., Takata, F., Yamauchi, A., Nakagawa, S., Egawa, T., Naito, M., Tsuruo, T., Sawada, Y., Niwa, M., and Kataoka, Y. (2005). Brain pericytes contribute to the induction and up-regulation of blood-brain barrier functions through transforming growth factor-beta production. Brain Res *1038*, 208-215. 10.1016/j.brainres.2005.01.027.

58. Dave, J.M., Mirabella, T., Weatherbee, S.D., and Greif, D.M. (2018). Pericyte ALK5/TIMP3 Axis Contributes to Endothelial Morphogenesis in the Developing Brain. Dev Cell *44*, 665-678.e666. 10.1016/j.devcel.2018.01.018.

59. Reyahi, A., Nik, A.M., Ghiami, M., Gritli-Linde, A., Pontén, F., Johansson, B.R., and Carlsson, P. (2015). Foxf2 Is Required for Brain Pericyte Differentiation and Development and Maintenance of the Blood-Brain Barrier. Dev Cell *34*, 19-32. 10.1016/j.devcel.2015.05.008.

60. Kim, Y., Imdad, R.Y., Stephenson, A.H., Sprague, R.S., and Lonigro, A.J. (1998). Vascular endothelial growth factor mRNA in pericytes is upregulated by phorbol myristate acetate. Hypertension *31*, 511-515. 10.1161/01.hyp.31.1.511.

61. Franco, M., Roswall, P., Cortez, E., Hanahan, D., and Pietras, K. (2011). Pericytes promote endothelial cell survival through induction of autocrine VEGF-A signaling and Bcl-w expression. Blood *118*, 2906-2917. 10.1182/blood-2011-01-331694.

62. Sato, T.N., Tozawa, Y., Deutsch, U., Wolburg-Buchholz, K., Fujiwara, Y.,

bioRxiv preprint doi: https://doi.org/10.1101/2025.04.08.647738; this version posted April 9, 2025. The copyright holder for this preprint (which was not certified by peer review) is the author/funder, who has granted bioRxiv a license to display the preprint in perpetuity. It is made available under a CC-BY 4.0 International license.

Gendron-Maguire, M., Gridley, T., Wolburg, H., Risau, W., and Qin, Y. (1995). Distinct roles of the receptor tyrosine kinases Tie-1 and Tie-2 in blood vessel formation. Nature *376*, 70-74. 10.1038/376070a0.

63. Thurston, G., Suri, C., Smith, K., McClain, J., Sato, T.N., Yancopoulos, G.D., and McDonald, D.M. (1999). Leakage-resistant blood vessels in mice transgenically overexpressing angiopoietin-1. Science *286*, 2511-2514. 10.1126/science.286.5449.2511.

64. Sundberg, C., Kowanetz, M., Brown, L.F., Detmar, M., and Dvorak, H.F. (2002). Stable expression of angiopoietin-1 and other markers by cultured pericytes: phenotypic similarities to a subpopulation of cells in maturing vessels during later stages of angiogenesis in vivo. Lab Invest *82*, 387-401. 10.1038/labinvest.3780433.

65. Wan, Y., Jin, H.J., Zhu, Y.Y., Fang, Z., Mao, L., He, Q., Xia, Y.P., Li, M., Li, Y., Chen, X., and Hu, B. (2018). MicroRNA-149-5p regulates blood-brain barrier permeability after transient middle cerebral artery occlusion in rats by targeting S1PR2 of pericytes. Faseb j *32*, 3133-3148. 10.1096/fj.201701121R.

66. Li, F., Lan, Y., Wang, Y., Wang, J., Yang, G., Meng, F., Han, H., Meng, A., Wang, Y., and Yang, X. (2011). Endothelial Smad4 maintains cerebrovascular integrity by activating N-cadherin through cooperation with Notch. Dev Cell *20*, 291-302. 10.1016/j.devcel.2011.01.011.

67. Liu, H., Zhang, W., Kennard, S., Caldwell, R.B., and Lilly, B. (2010). Notch3 is critical for proper angiogenesis and mural cell investment. Circ Res *107*,

bioRxiv preprint doi: https://doi.org/10.1101/2025.04.08.647738; this version posted April 9, 2025. The copyright holder for this preprint (which was not certified by peer review) is the author/funder, who has granted bioRxiv a license to display the preprint in perpetuity. It is made available under a CC-BY 4.0 International license.

860-870. 10.1161/circresaha.110.218271.

68. Gundersen, G.A., Vindedal, G.F., Skare, O., and Nagelhus, E.A. (2014). Evidence that pericytes regulate aquaporin-4 polarization in mouse cortical astrocytes. Brain Struct Funct *219*, 2181-2186. 10.1007/s00429-013-0629-0.

69. Jeanne, M., Jorgensen, J., and Gould, D.B. (2015). Molecular and Genetic Analyses of Collagen Type IV Mutant Mouse Models of Spontaneous Intracerebral Hemorrhage Identify Mechanisms for Stroke Prevention. Circulation *131*, 1555-1565. 10.1161/circulationaha.114.013395.

70. Gautam, J., Zhang, X., and Yao, Y. (2016). The role of pericytic laminin in blood brain barrier integrity maintenance. Sci Rep *6*, 36450. 10.1038/srep36450.

71. Gautam, J., Cao, Y., and Yao, Y. (2020). Pericytic Laminin Maintains Blood-Brain Barrier Integrity in an Age-Dependent Manner. Transl Stroke Res *11*, 228-242. 10.1007/s12975-019-00709-8.

72. Özkan, E., Çetin-Taş, Y., Şekerdağ, E., Kızılırmak, A.B., Taş, A., Yıldız, E., Yapıcı-Eser, H., Karahüseyinoğlu, S., Zeybel, M., and Gürsoy-Özdemir, Y. (2021). Blood-brain barrier leakage and perivascular collagen accumulation precede microvessel rarefaction and memory impairment in a chronic hypertension animal model. Metab Brain Dis *36*, 2553-2566. 10.1007/s11011-021-00767-8.

73. Stewart, P.A., and Wiley, M.J. (1981). Developing nervous tissue induces formation of blood-brain barrier characteristics in invading endothelial cells: a

bioRxiv preprint doi: https://doi.org/10.1101/2025.04.08.647738; this version posted April 9, 2025. The copyright holder for this preprint (which was not certified by peer review) is the author/funder, who has granted bioRxiv a license to display the preprint in perpetuity. It is made available under a CC-BY 4.0 International license.

study using quail--chick transplantation chimeras. Dev Biol *84*, 183-192. 10.1016/0012-1606(81)90382-1.

74. Hellström, M., Kalén, M., Lindahl, P., Abramsson, A., and Betsholtz, C. (1999). Role of PDGF-B and PDGFR-beta in recruitment of vascular smooth muscle cells and pericytes during embryonic blood vessel formation in the mouse. Development *126*, 3047-3055.

75. Bjarnegård, M., Enge, M., Norlin, J., Gustafsdottir, S., Fredriksson, S., Abramsson, A., Takemoto, M., Gustafsson, E., Fässler, R., and Betsholtz, C. (2004). Endothelium-specific ablation of PDGFB leads to pericyte loss and glomerular, cardiac and placental abnormalities. Development *131*, 1847-1857. 10.1242/dev.01080.

76. Mi, H., Haeberle, H., and Barres, B.A. (2001). Induction of astrocyte differentiation by endothelial cells. J Neurosci *21*, 1538-1547. 10.1523/jneurosci.21-05-01538.2001.

77. Paredes, I., Vieira, J.R., Shah, B., Ramunno, C.F., Dyckow, J., Adler, H., Richter, M., Schermann, G., Giannakouri, E., Schirmer, L., et al. (2021). Oligodendrocyte precursor cell specification is regulated by bidirectional neural progenitor-endothelial cell crosstalk. Nat Neurosci *24*, 478-488. 10.1038/s41593-020-00788-z.

78. Daneman, R., Agalliu, D., Zhou, L., Kuhnert, F., Kuo, C.J., and Barres, B.A. (2009). Wnt/beta-catenin signaling is required for CNS, but not non-CNS, angiogenesis. Proc Natl Acad Sci U S A *106*, 641-646.

bioRxiv preprint doi: https://doi.org/10.1101/2025.04.08.647738; this version posted April 9, 2025. The copyright holder for this preprint (which was not certified by peer review) is the author/funder, who has granted bioRxiv a license to display the preprint in perpetuity. It is made available under a CC-BY 4.0 International license.

10.1073/pnas.0805165106.

79. Kuhnert, F., Mancuso, M.R., Shamloo, A., Wang, H.T., Choksi, V., Florek, M., Su, H., Fruttiger, M., Young, W.L., Heilshorn, S.C., and Kuo, C.J. (2010). Essential regulation of CNS angiogenesis by the orphan G protein-coupled receptor GPR124. Science *330*, 985-989. 10.1126/science.1196554.

80. Cullen, M., Elzarrad, M.K., Seaman, S., Zudaire, E., Stevens, J., Yang, M.Y., Li, X., Chaudhary, A., Xu, L., Hilton, M.B., et al. (2011). GPR124, an orphan G protein-coupled receptor, is required for CNS-specific vascularization and establishment of the blood-brain barrier. Proc Natl Acad Sci U S A *108*, 5759-5764. 10.1073/pnas.1017192108.

81. Zhou, Y., and Nathans, J. (2014). Gpr124 controls CNS angiogenesis and blood-brain barrier integrity by promoting ligand-specific canonical wnt signaling. Dev Cell *31*, 248-256. 10.1016/j.devcel.2014.08.018.

82. Thomas, M., and Augustin, H.G. (2009). The role of the Angiopoietins in vascular morphogenesis. Angiogenesis *12*, 125-137. 10.1007/s10456-009-9147-3.

83. Nico, B., Frigeri, A., Nicchia, G.P., Quondamatteo, F., Herken, R., Errede, M., Ribatti, D., Svelto, M., and Roncali, L. (2001). Role of aquaporin-4 water channel in the development and integrity of the blood-brain barrier. J Cell Sci *114*, 1297-1307. 10.1242/jcs.114.7.1297.

84. Nicchia, G.P., Nico, B., Camassa, L.M., Mola, M.G., Loh, N., Dermietzel, R., Spray, D.C., Svelto, M., and Frigeri, A. (2004). The role of aquaporin-4 in the

bioRxiv preprint doi: https://doi.org/10.1101/2025.04.08.647738; this version posted April 9, 2025. The copyright holder for this preprint (which was not certified by peer review) is the author/funder, who has granted bioRxiv a license to display the preprint in perpetuity. It is made available under a CC-BY 4.0 International license.

blood-brain barrier development and integrity: studies in animal and cell culture models. Neuroscience *129*, 935-945. 10.1016/j.neuroscience.2004.07.055.

85. Hartfuss, E., Galli, R., Heins, N., and Götz, M. (2001). Characterization of CNS precursor subtypes and radial glia. Dev Biol *229*, 15-30. 10.1006/dbio.2000.9962.

86. Malatesta, P., Appolloni, I., and Calzolari, F. (2008). Radial glia and neural stem cells. Cell Tissue Res *331*, 165-178. 10.1007/s00441-007-0481-8.

87. Qian, X., Shen, Q., Goderie, S.K., He, W., Capela, A., Davis, A.A., and Temple, S. (2000). Timing of CNS cell generation: a programmed sequence of neuron and glial cell production from isolated murine cortical stem cells. Neuron *28*, 69-80. 10.1016/s0896-6273(00)00086-6.

88. Price, J., Williams, B.P., and Götz, M. (1995). The generation of cellular diversity in the cerebral cortex. Ciba Found Symp *193*, 71-84; discussion 117-126. 10.1002/9780470514795.ch4.

89. Grupp, L., Wolburg, H., and Mack, A.F. (2010). Astroglial structures in the zebrafish brain. J Comp Neurol *518*, 4277-4287. 10.1002/cne.22481.

90. Chen, J., Poskanzer, K.E., Freeman, M.R., and Monk, K.R. (2020). Live-imaging of astrocyte morphogenesis and function in zebrafish neural circuits. Nat Neurosci *23*, 1297-1306. 10.1038/s41593-020-0703-x.

91. Johnson, K., Barragan, J., Bashiruddin, S., Smith, C.J., Tyrrell, C., Parsons, M.J., Doris, R., Kucenas, S., Downes, G.B., Velez, C.M., et al. (2016). Gfap-

bioRxiv preprint doi: https://doi.org/10.1101/2025.04.08.647738; this version posted April 9, 2025. The copyright holder for this preprint (which was not certified by peer review) is the author/funder, who has granted bioRxiv a license to display the preprint in perpetuity. It is made available under a CC-BY 4.0 International license.

positive radial glial cells are an essential progenitor population for later-born neurons and glia in the zebrafish spinal cord. Glia *64*, 1170-1189. 10.1002/glia.22990.

92. Umans, R.A., Pollock, C., Mills, W.A., 3rd, Clark, K.C., Pan, Y.A., and Sontheimer, H. (2021). Using Zebrafish to Elucidate Glial-Vascular Interactions During CNS Development. Front Cell Dev Biol *9*, 654338. 10.3389/fcell.2021.654338.

93. Matsuoka, R.L., Rossi, A., Stone, O.A., and Stainier, D.Y.R. (2017). CNS-resident progenitors direct the vascularization of neighboring tissues. Proc Natl Acad Sci U S A *114*, 10137-10142. 10.1073/pnas.1619300114.

94. Alvarez, J.I., Dodelet-Devillers, A., Kebir, H., Ifergan, I., Fabre, P.J., Terouz, S., Sabbagh, M., Wosik, K., Bourbonnière, L., Bernard, M., et al. (2011). The Hedgehog pathway promotes blood-brain barrier integrity and CNS immune quiescence. Science *334*, 1727-1731. 10.1126/science.1206936.

95. Brilha, S., Ong, C.W.M., Weksler, B., Romero, N., Couraud, P.O., and Friedland, J.S. (2017). Matrix metalloproteinase-9 activity and a downregulated Hedgehog pathway impair blood-brain barrier function in an in vitro model of CNS tuberculosis. Sci Rep *7*, 16031. 10.1038/s41598-017-16250-3.

96. Shi, T., Yue, S., Xie, C., Li, X., Yang, D., Hu, L., Zhong, Y., Zhang, Y., and Liu, W. (2024). MMP-2-mediated Scube2 degradation promotes blood-brain barrier disruption by blocking the interaction between astrocytes and

bioRxiv preprint doi: https://doi.org/10.1101/2025.04.08.647738; this version posted April 9, 2025. The copyright holder for this preprint (which was not certified by peer review) is the author/funder, who has granted bioRxiv a license to display the preprint in perpetuity. It is made available under a CC-BY 4.0 International license.

endothelial cells via inhibiting Sonic hedgehog pathway during early cerebral ischemia. J Neurochem *168*, 1877-1894. 10.1111/jnc.16021.

97. Xing, G., Zhao, T., Zhang, X., Li, H., Li, X., Cui, P., Li, M., Li, D., Zhang, N., and Jiang, W. (2020). Astrocytic Sonic Hedgehog Alleviates Intracerebral Hemorrhagic Brain Injury via Modulation of Blood-Brain Barrier Integrity. Front Cell Neurosci *14*, 575690. 10.3389/fncel.2020.575690.

98. Lawson, N.D., Vogel, A.M., and Weinstein, B.M. (2002). sonic hedgehog and vascular endothelial growth factor act upstream of the Notch pathway during arterial endothelial differentiation. Dev Cell *3*, 127-136. 10.1016/s1534-5807(02)00198-3.

99. Mannan, A., Dhiamn, S., Garg, N., and Singh, T.G. (2023). Pharmacological modulation of Sonic Hedgehog signaling pathways in Angiogenesis: A mechanistic perspective. Dev Biol *504*, 58-74. 10.1016/j.ydbio.2023.09.009.

100. Argaw, A.T., Asp, L., Zhang, J., Navrazhina, K., Pham, T., Mariani, J.N., Mahase, S., Dutta, D.J., Seto, J., Kramer, E.G., et al. (2012). Astrocyte-derived VEGF-A drives blood-brain barrier disruption in CNS inflammatory disease. J Clin Invest *122*, 2454-2468. 10.1172/jci60842.

101. Chapouly, C., Tadesse Argaw, A., Horng, S., Castro, K., Zhang, J., Asp, L., Loo, H., Laitman, B.M., Mariani, J.N., Straus Farber, R., et al. (2015). Astrocytic TYMP and VEGFA drive blood-brain barrier opening in inflammatory central nervous system lesions. Brain *138*, 1548-1567. 10.1093/brain/awv077.

bioRxiv preprint doi: https://doi.org/10.1101/2025.04.08.647738; this version posted April 9, 2025. The copyright holder for this preprint (which was not certified by peer review) is the author/funder, who has granted bioRxiv a license to display the preprint in perpetuity. It is made available under a CC-BY 4.0 International license.

1434 102. Matsumoto, T., and Mugishima, H. (2006). Signal transduction via vascular
1435 endothelial growth factor (VEGF) receptors and their roles in atherogenesis. J
1436 Atheroscler Thromb *13*, 130-135. 10.5551/jat.13.130.
1437 103. Jakobsson, L., Franco, C.A., Bentley, K., Collins, R.T., Ponsioen, B., Aspalter,
1438 I.M., Rosewell, I., Busse, M., Thurston, G., Medvinsky, A., et al. (2010).
1439 Endothelial cells dynamically compete for the tip cell position during
1440 angiogenic sprouting. Nature Cell Biology *12*, 943-953. 10.1038/ncb2103.
1441 104. Liu, Z.J., Shirakawa, T., Li, Y., Soma, A., Oka, M., Dotto, G.P., Fairman,
1442 R.M., Velazquez, O.C., and Herlyn, M. (2003). Regulation of Notch1 and Dll4
1443 by vascular endothelial growth factor in arterial endothelial cells: implications
1444 for modulating arteriogenesis and angiogenesis. Mol Cell Biol *23*, 14-25.
1445 10.1128/mcb.23.1.14-25.2003.
1446 105. Olsson, A.K., Dimberg, A., Kreuger, J., and Claesson-Welsh, L. (2006). VEGF
1447 receptor signalling - in control of vascular function. Nat Rev Mol Cell Biol *7*,
1448 359-371. 10.1038/nrm1911.
1449 106. Xu, L., Nirwane, A., and Yao, Y. (2019). Basement membrane and blood-brain
1450 barrier. Stroke Vasc Neurol *4*, 78-82. 10.1136/svn-2018-000198.
1451 107. Halder, S.K., Sapkota, A., and Milner, R. (2022). The impact of genetic
1452 manipulation of laminin and integrins at the blood-brain barrier. Fluids
1453 Barriers CNS *19*, 50. 10.1186/s12987-022-00346-8.
1454 108. Yao, Y., Chen, Z.L., Norris, E.H., and Strickland, S. (2014). Astrocytic laminin
1455 regulates pericyte differentiation and maintains blood brain barrier integrity.

bioRxiv preprint doi: https://doi.org/10.1101/2025.04.08.647738; this version posted April 9, 2025. The copyright holder for this preprint (which was not certified by peer review) is the author/funder, who has granted bioRxiv a license to display the preprint in perpetuity. It is made available under a CC-BY 4.0 International license.

Nat Commun *5*, 3413. 10.1038/ncomms4413.

109. Milner, R., and Campbell, I.L. (2002). Developmental regulation of beta1 integrins during angiogenesis in the central nervous system. Mol Cell Neurosci *20*, 616-626. 10.1006/mcne.2002.1151.

110. Nishimura, S.L., Boylen, K.P., Einheber, S., Milner, T.A., Ramos, D.M., and Pytela, R. (1998). Synaptic and glial localization of the integrin alphavbeta8 in mouse and rat brain. Brain Res *791*, 271-282. 10.1016/s0006-8993(98)00118-8.

111. McCarty, J.H., Lacy-Hulbert, A., Charest, A., Bronson, R.T., Crowley, D., Housman, D., Savill, J., Roes, J., and Hynes, R.O. (2005). Selective ablation of alphav integrins in the central nervous system leads to cerebral hemorrhage, seizures, axonal degeneration and premature death. Development *132*, 165-176. 10.1242/dev.01551.

112. Beis, D., Bartman, T., Jin, S.W., Scott, I.C., D'Amico, L.A., Ober, E.A., Verkade, H., Frantsve, J., Field, H.A., Wehman, A., et al. (2005). Genetic and cellular analyses of zebrafish atrioventricular cushion and valve development. Development *132*, 4193-4204. 10.1242/dev.01970.

113. Jin, S.W., Beis, D., Mitchell, T., Chen, J.N., and Stainier, D.Y. (2005). Cellular and molecular analyses of vascular tube and lumen formation in zebrafish. Development *132*, 5199-5209. 10.1242/dev.02087.

114. Chang, N., Sun, C., Gao, L., Zhu, D., Xu, X., Zhu, X., Xiong, J.W., and Xi, J.J. (2013). Genome editing with RNA-guided Cas9 nuclease in zebrafish

bioRxiv preprint doi: https://doi.org/10.1101/2025.04.08.647738; this version posted April 9, 2025. The copyright holder for this preprint (which was not certified by peer review) is the author/funder, who has granted bioRxiv a license to display the preprint in perpetuity. It is made available under a CC-BY 4.0 International license.

embryos. Cell Res *23*, 465-472. 10.1038/cr.2013.45.

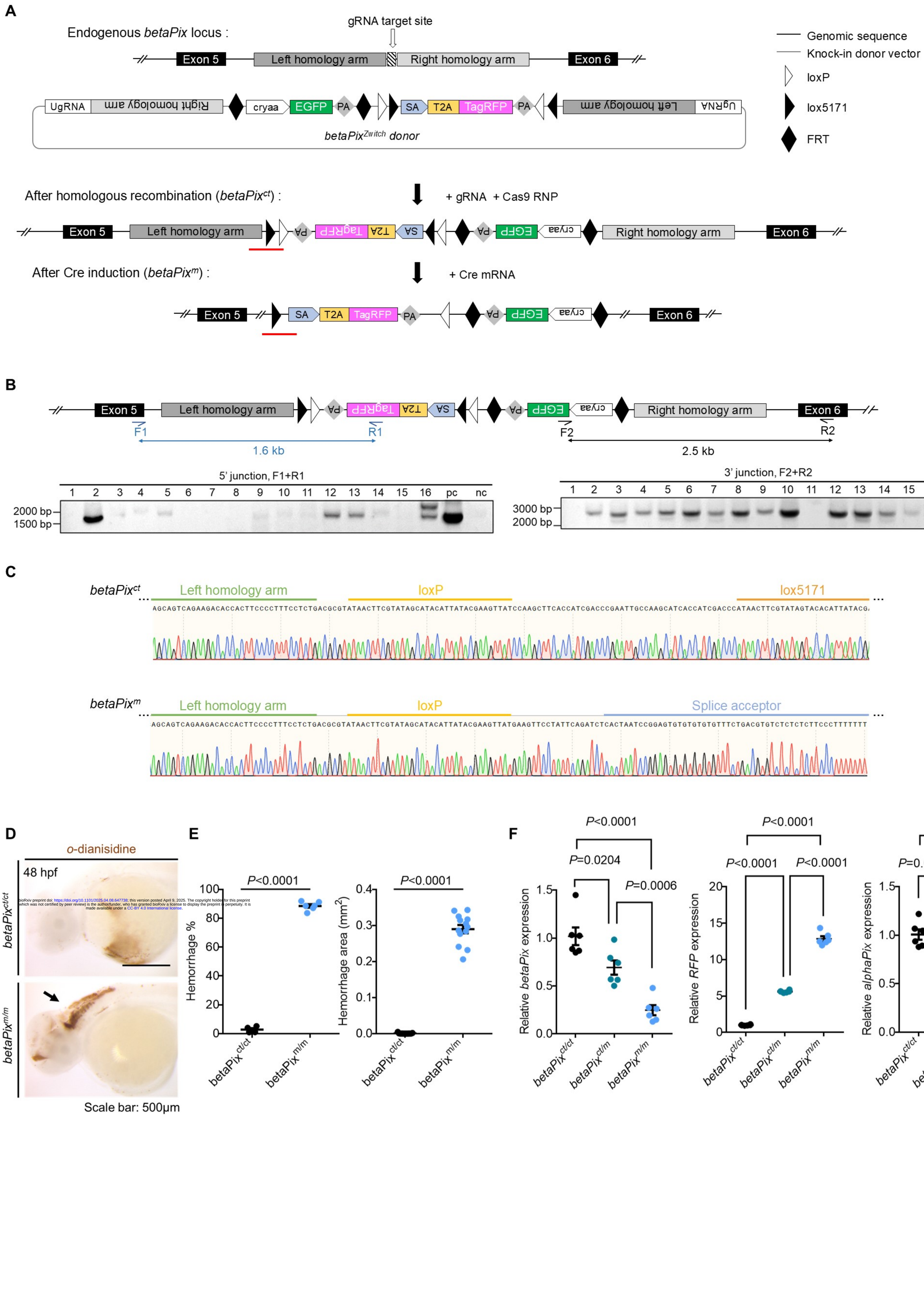
115. Jao, L.E., Wente, S.R., and Chen, W. (2013). Efficient multiplex biallelic zebrafish genome editing using a CRISPR nuclease system. Proc Natl Acad Sci U S A 110, 13904-13909. 10.1073/pnas.1308335110.

116. Kawakami, K. (2004). Transgenesis and gene trap methods in zebrafish by using the Tol2 transposable element. Methods Cell Biol *77*, 201-222. 10.1016/s0091-679x(04)77011-9.

117. Lei, L., Yan, S.Y., Yang, R., Chen, J.Y., Li, Y., Bu, Y., Chang, N., Zhou, Q., Zhu, X., Li, C.Y., and Xiong, J.W. (2017). Spliceosomal protein eftud2 mutation leads to p53-dependent apoptosis in zebrafish neural progenitors. Nucleic Acids Res *45*, 3422-3436. 10.1093/nar/gkw1043.

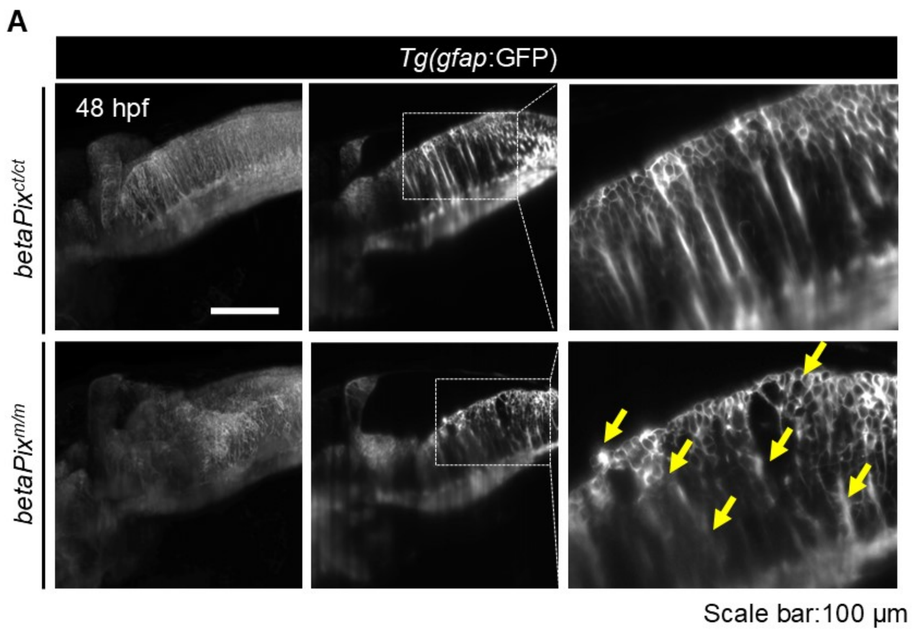
118. Pang, M., Bai, L., Zong, W., Wang, X., Bu, Y., Xiong, C., Zheng, J., Li, J., Gao, W., Feng, Z., et al. (2020). Light-sheet fluorescence imaging charts the gastrula origin of vascular endothelial cells in early zebrafish embryos. Cell Discovery *6*, 74. 10.1038/s41421-020-00204-7.

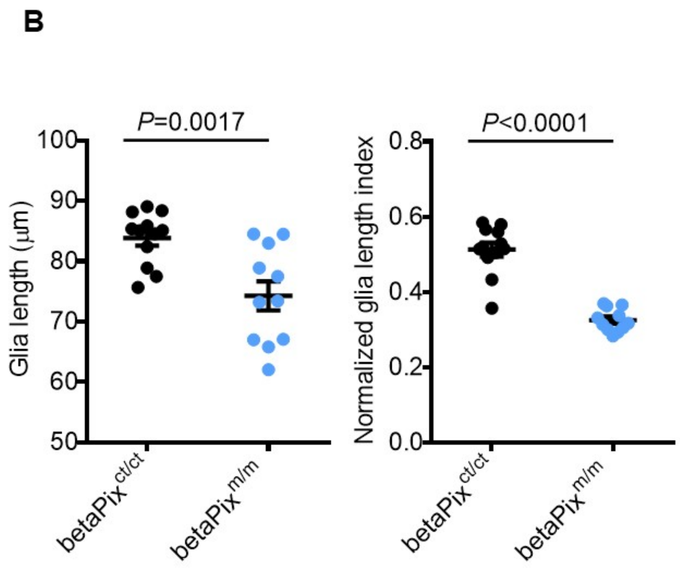
Figure 1

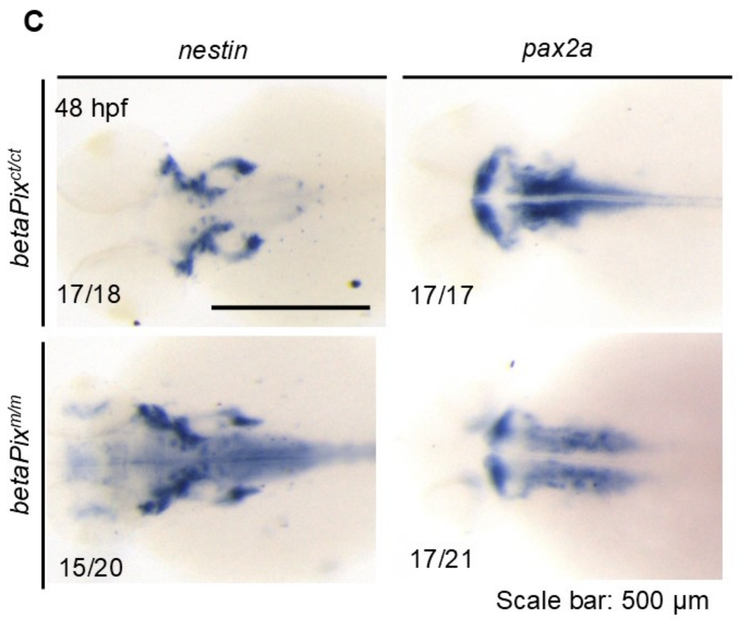


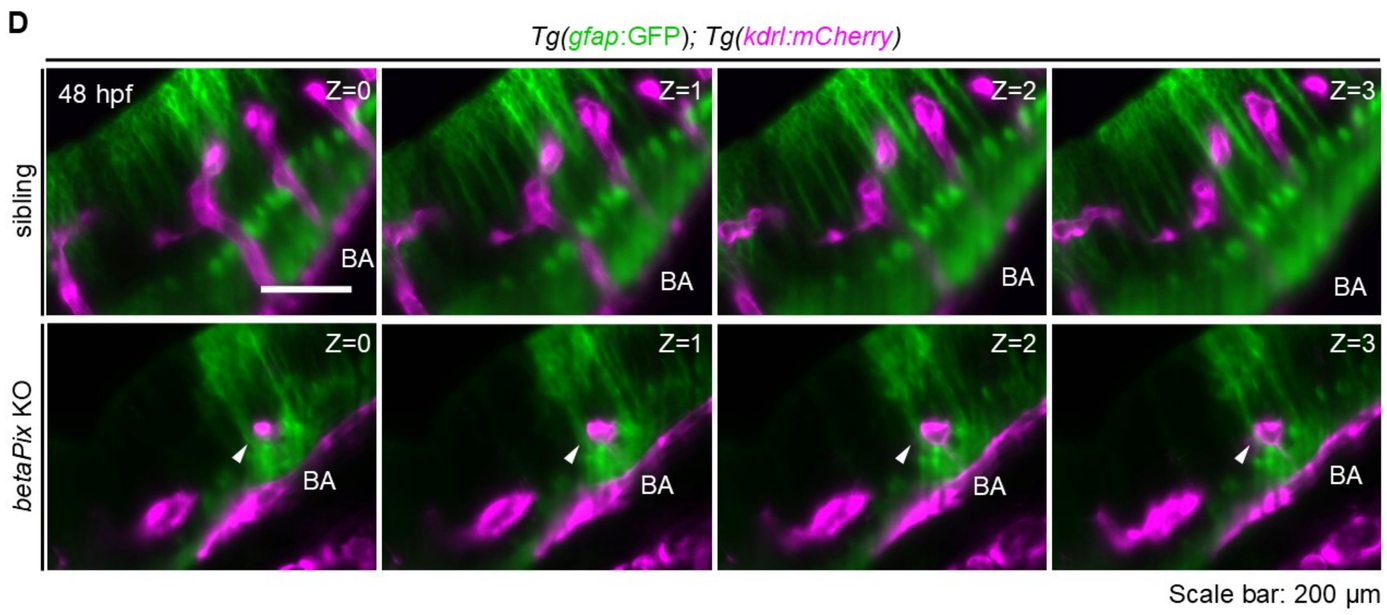
bioRxiv preprint doi: https://doi.org/10.1101/2025.04.08.647738; this version posted April 9, 2025. The copyright holder for this preprint (which was not certified by peer review) is the author/funder, who has granted bioRxiv a license to display the preprint in perpetuity. It is made available under a CC-BY 4.0 International license.

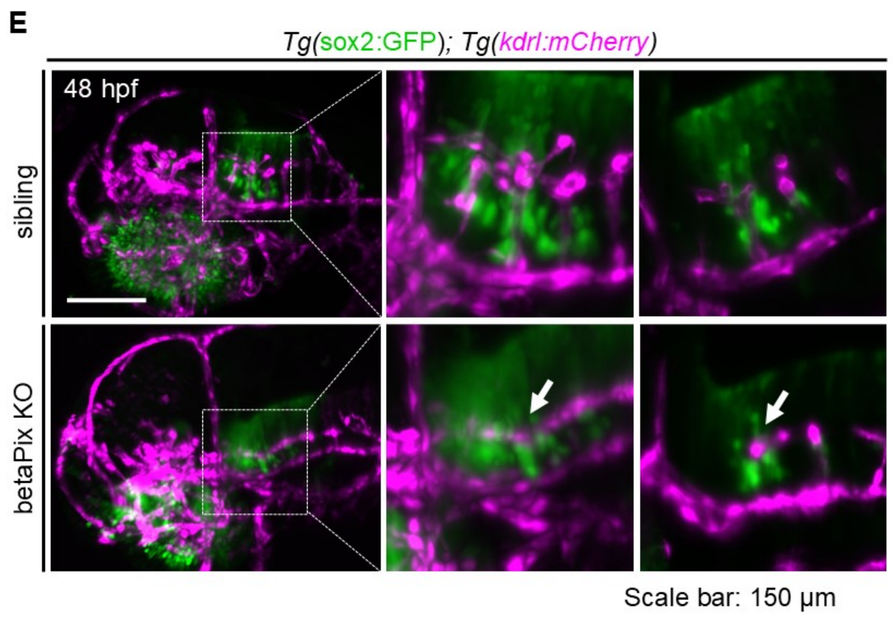
Figure 2

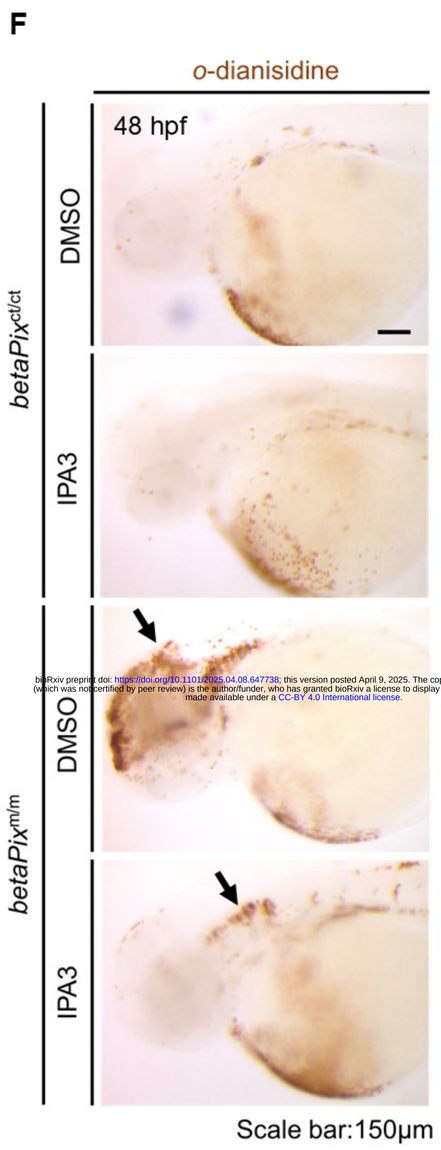


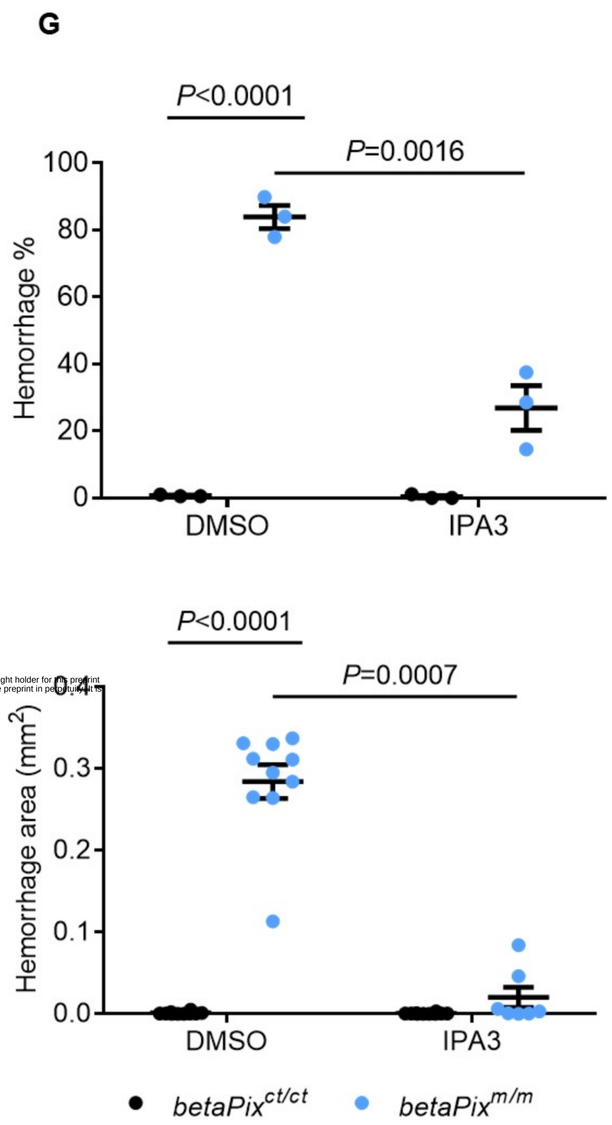


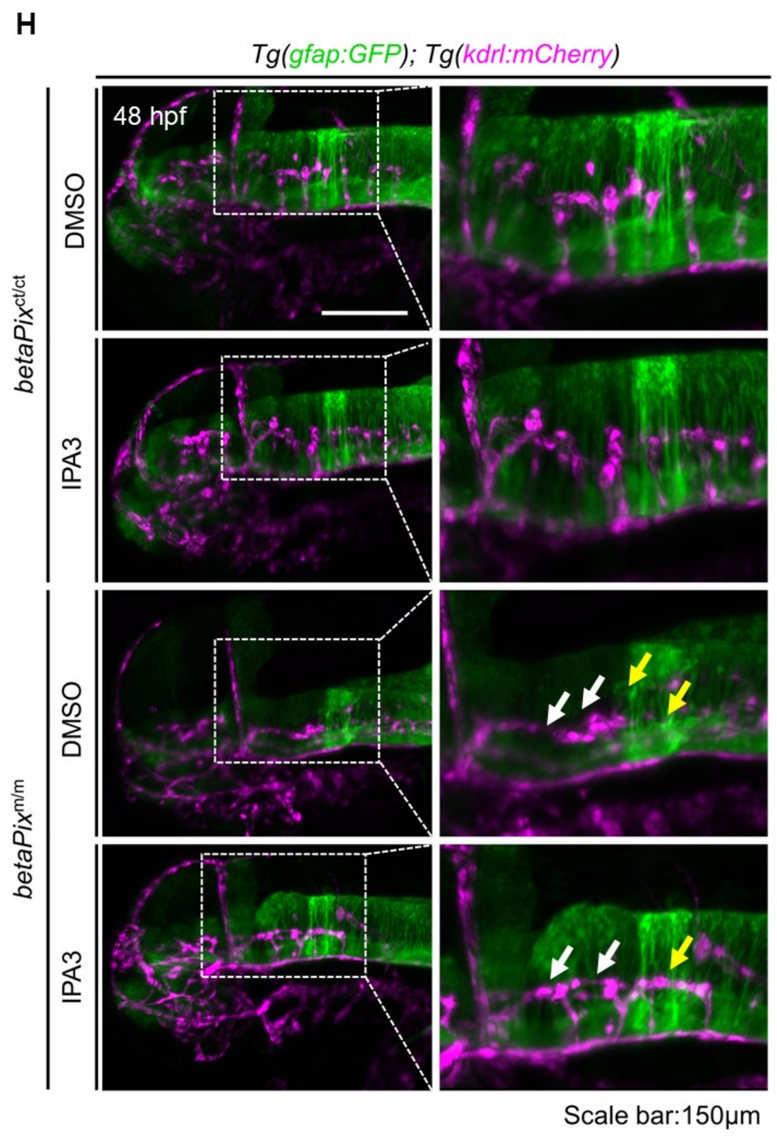


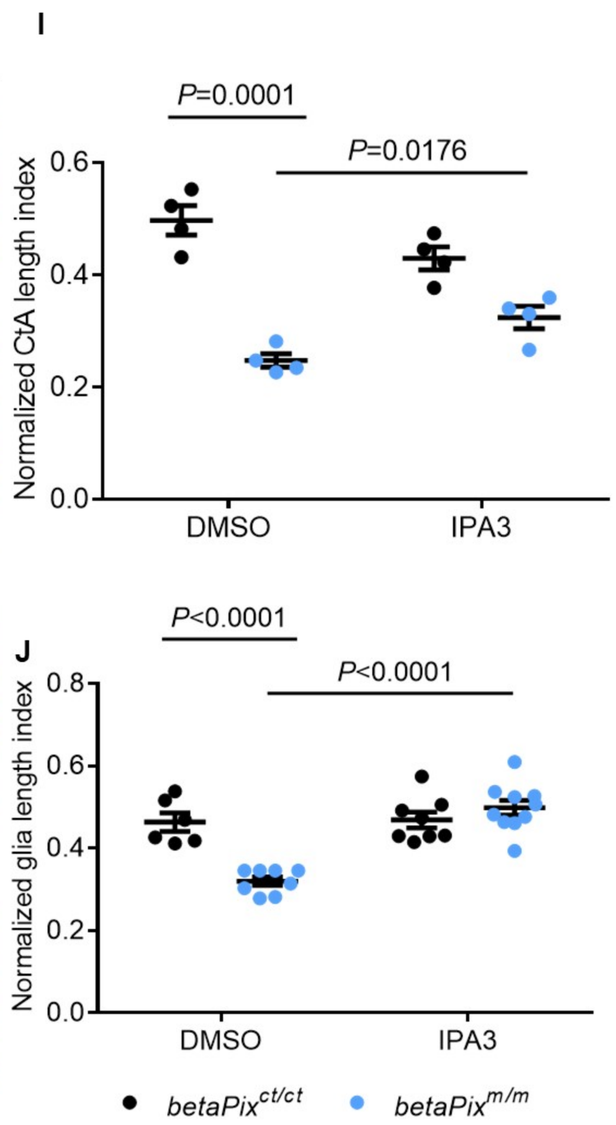






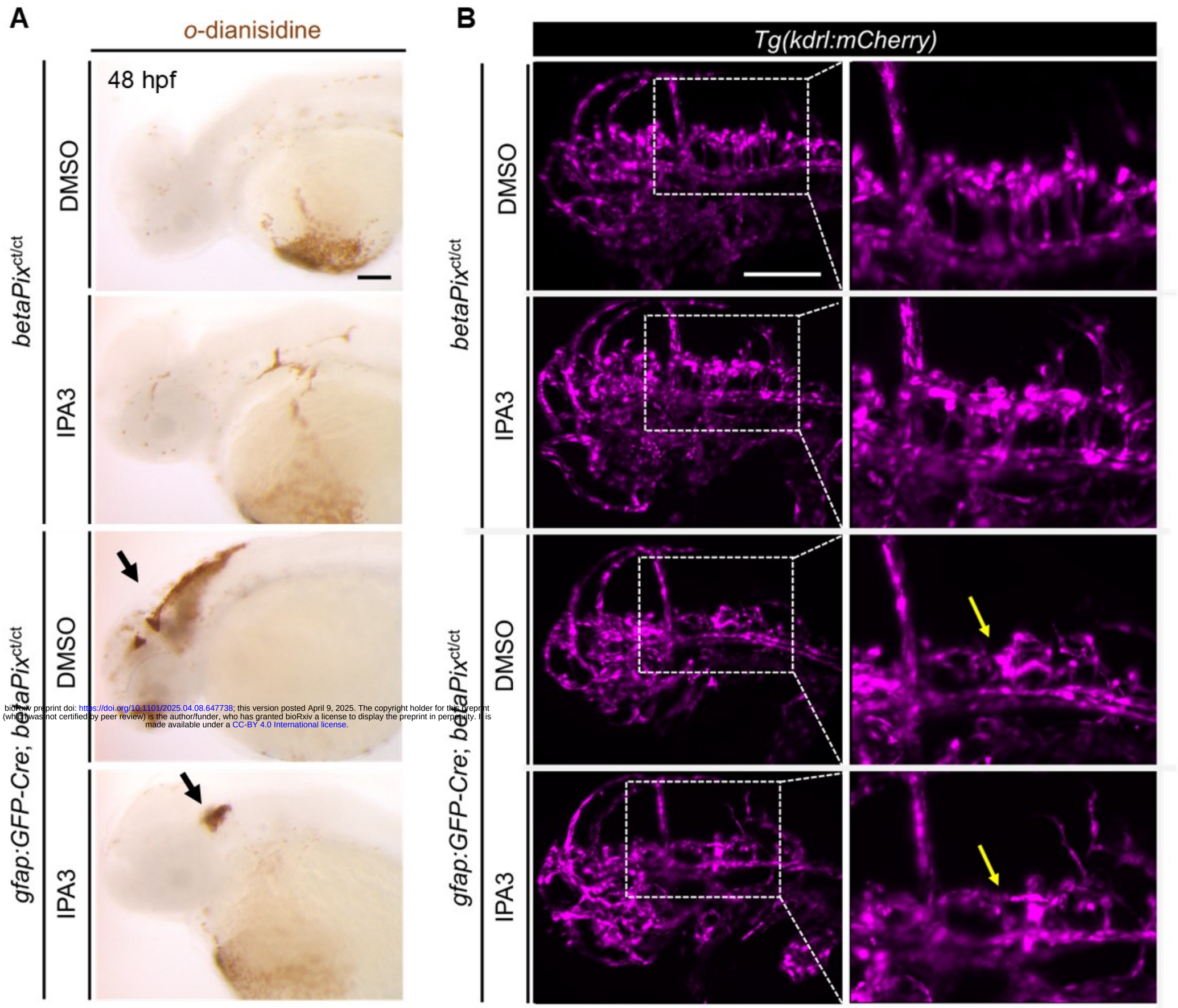






bioRxiv preprint doi: https://doi.org/10.1101/2025.04.08.647738; this version posted April 9, 2025. The copyright holder for this preprint (which was not certified by peer review) is the author/funder, who has granted bioRxiv a license to display the preprint in perpetuity. It is made available under a CC-BY 4.0 International license.

Figure 3



bioRxiv preprint doi: https://doi.org/10.1101/2025.04.08.647738; this version posted April 9, 2025. The copyright holder for this preprint (which was not certified by peer review) is the author/funder, who has granted bioRxiv a license to display the preprint in perpetuity. It is made available under a CC-BY 4.0 International license.

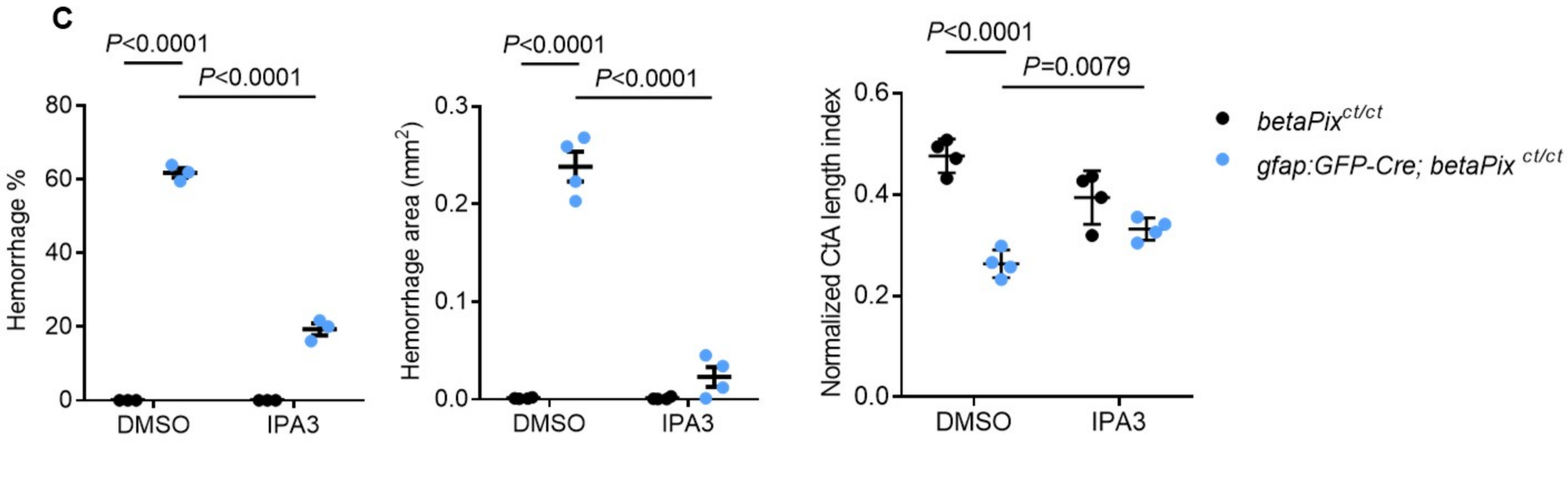
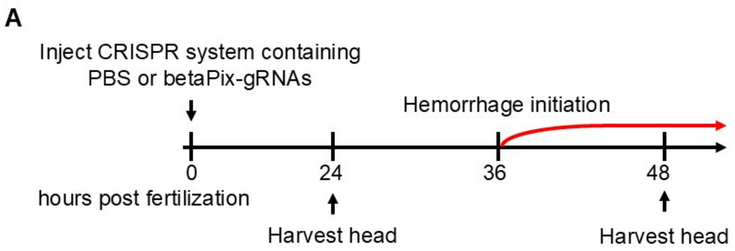
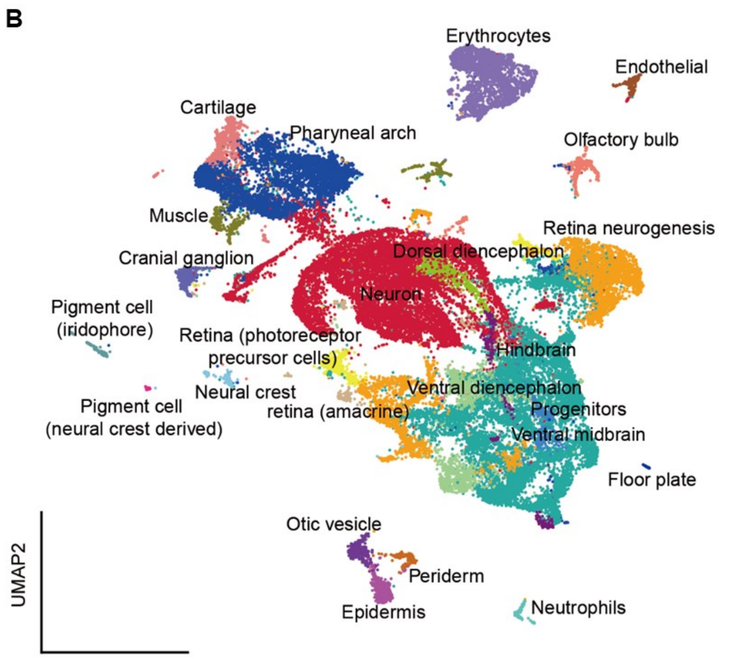
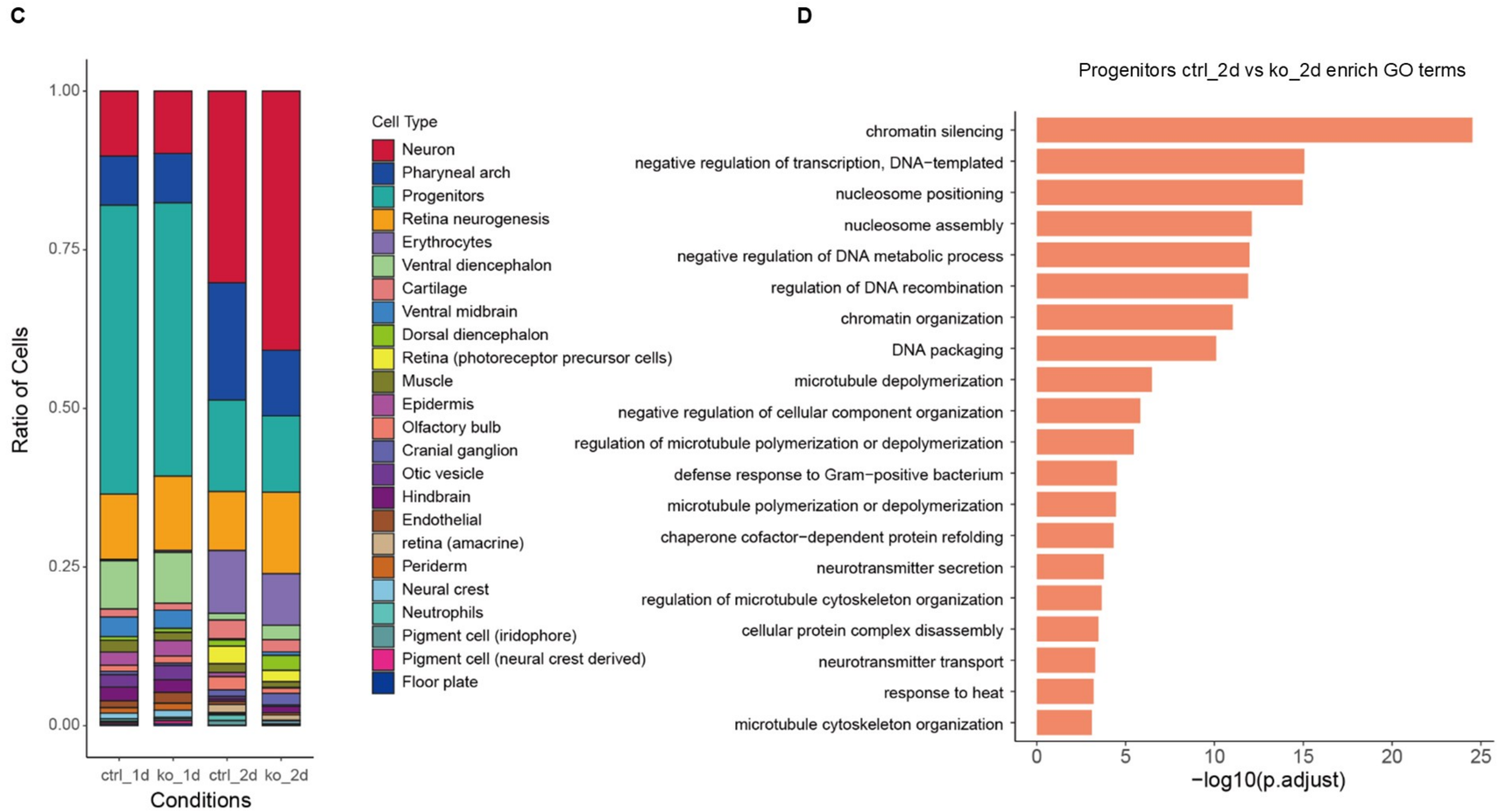
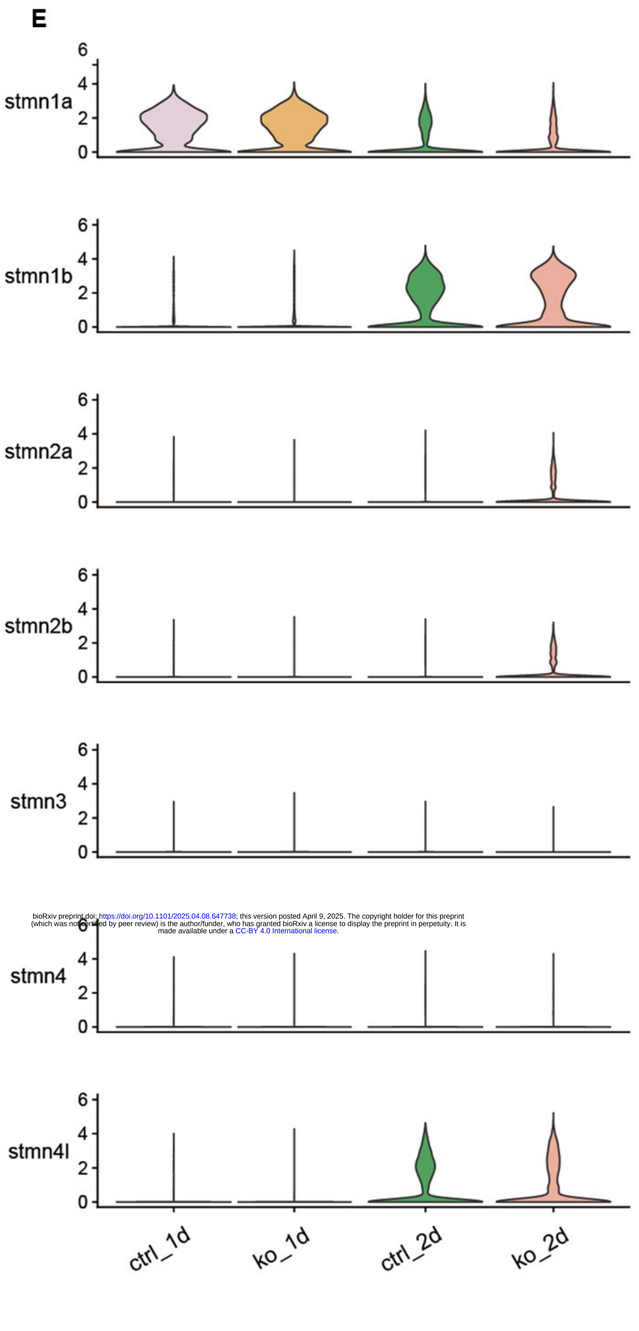


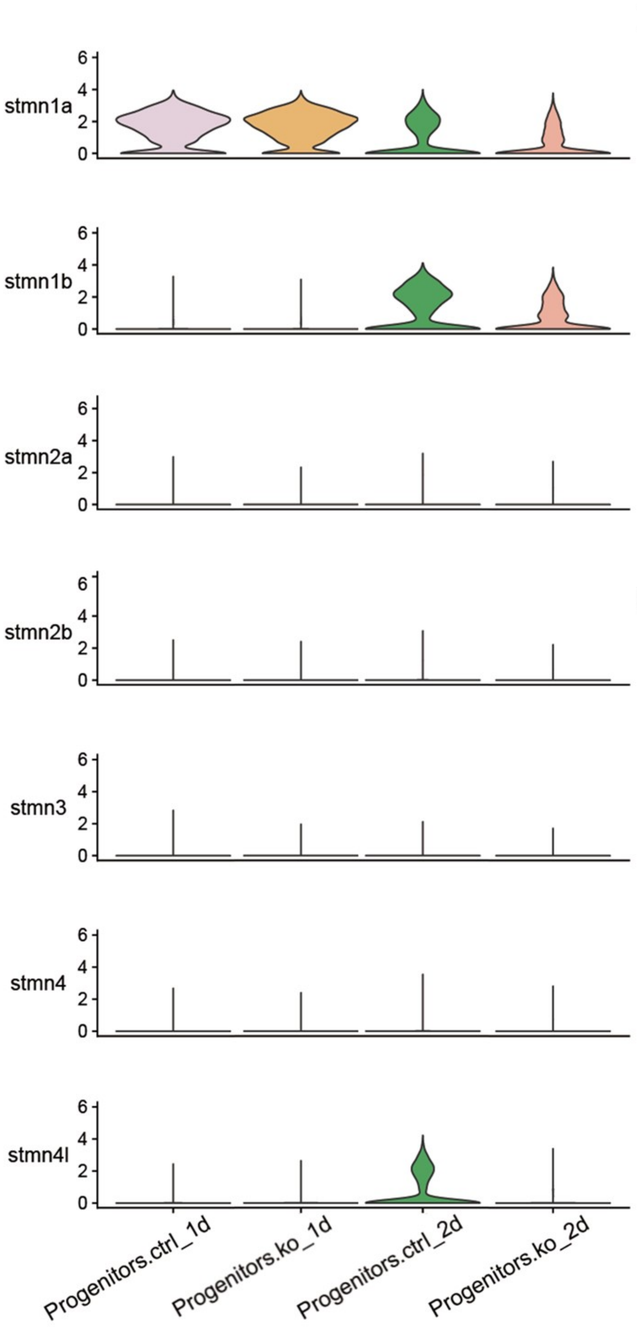
Figure 4

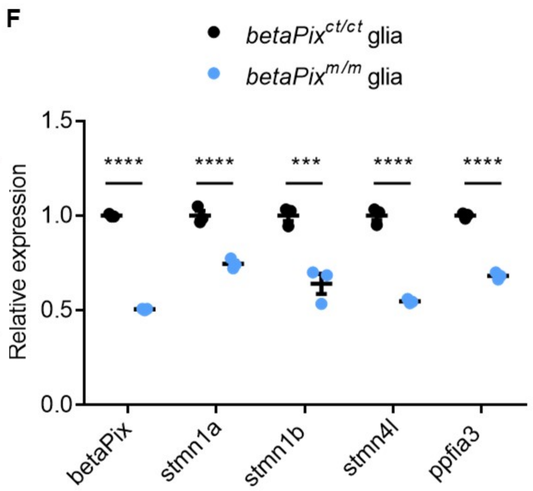


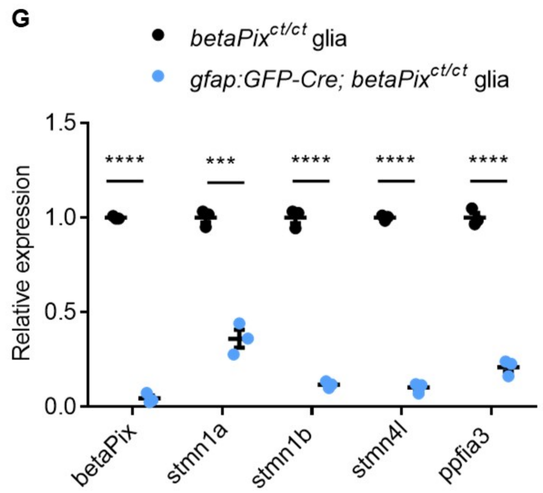


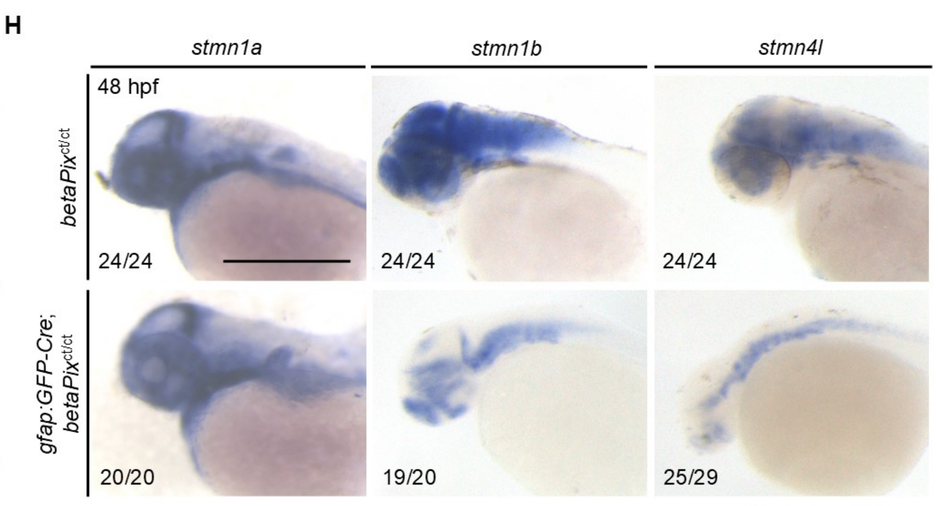






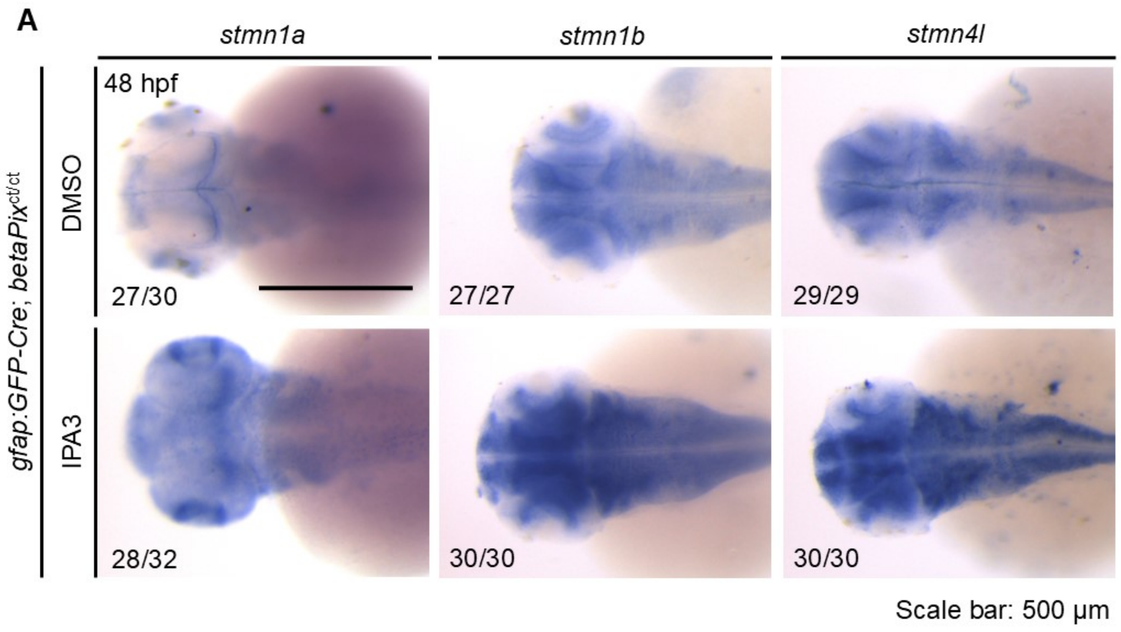


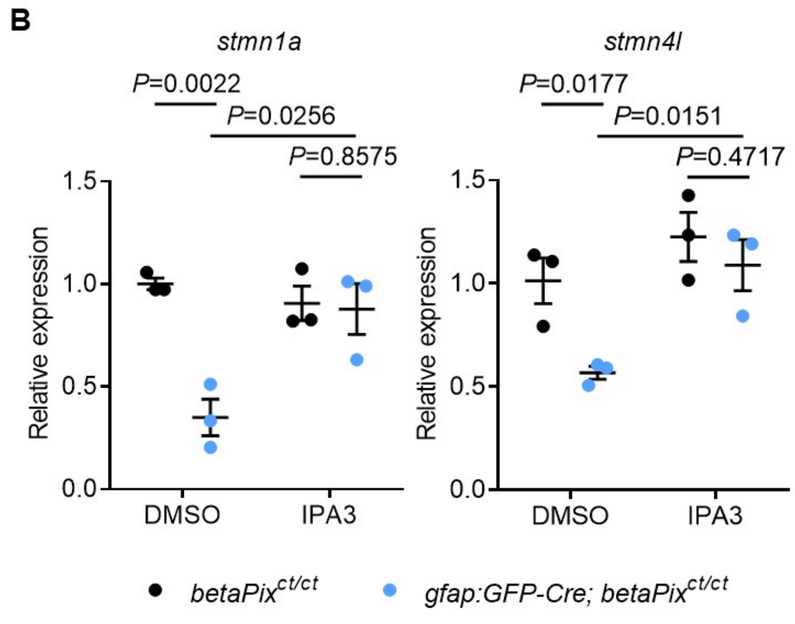


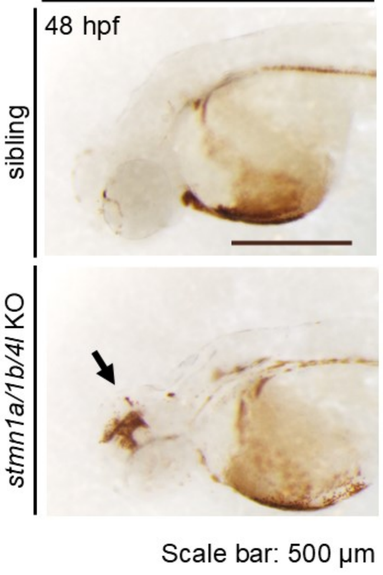


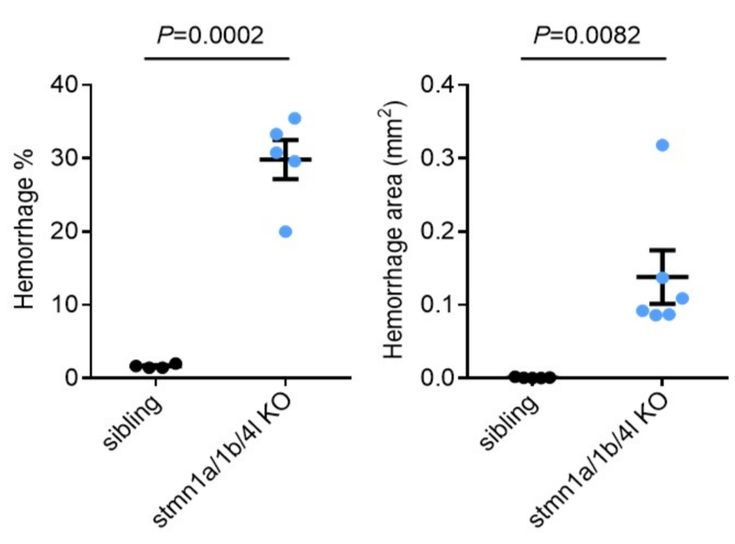
bioRxiv preprint doi: https://doi.org/10.1101/2025.04.08.647738; this version posted April 9, 2025. The copyright holder for this preprint (which was not certified by peer review) is the author/funder, who has granted bioRxiv a license to display the preprint in perpetuity. It is made available under a CC-BY 4.0 International license.

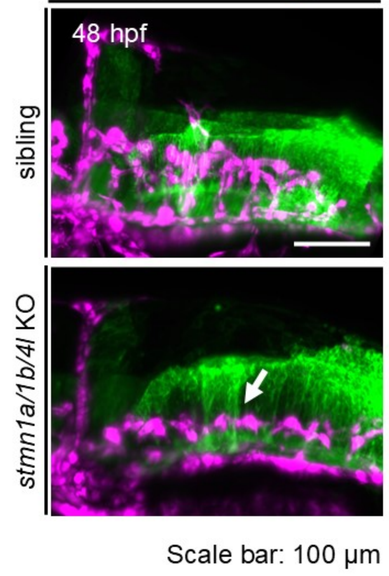
Figure 5

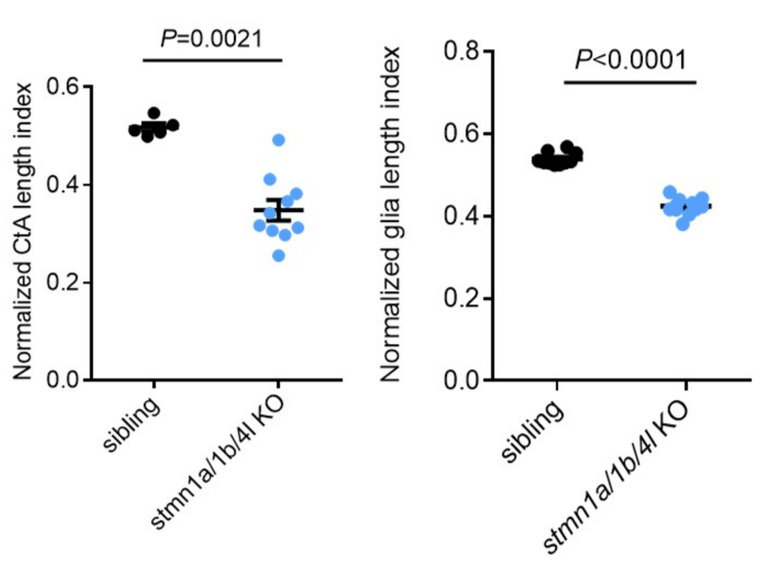


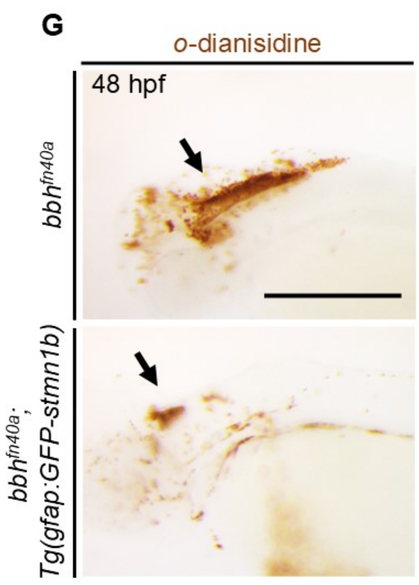


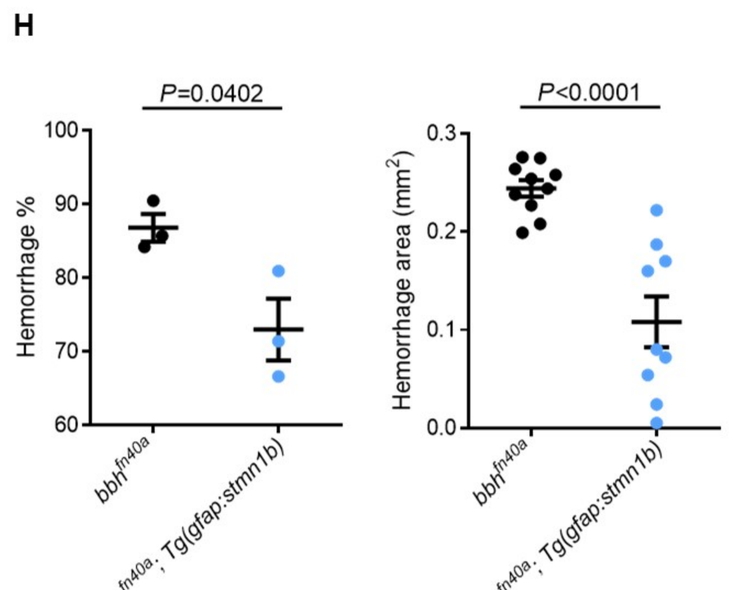


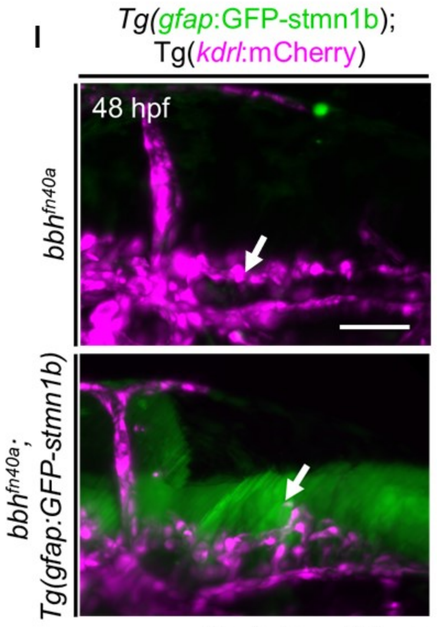


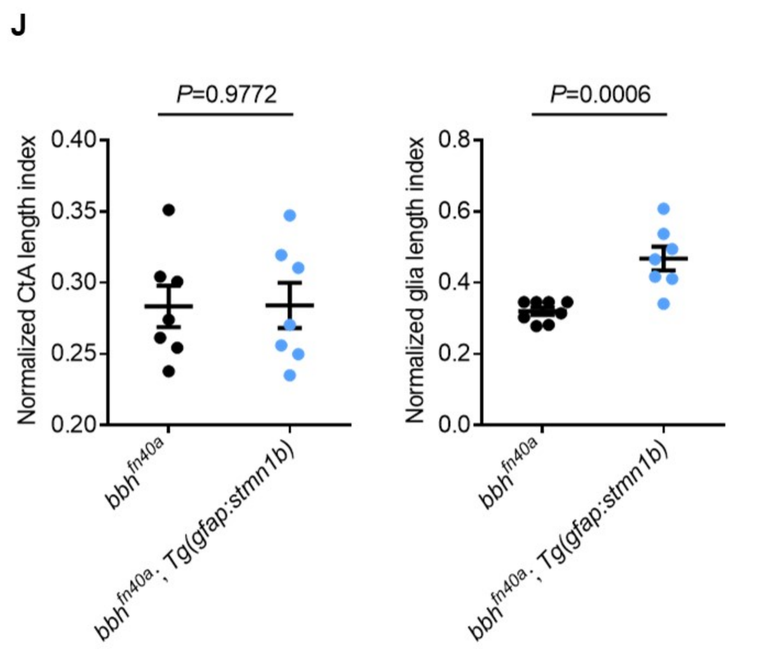


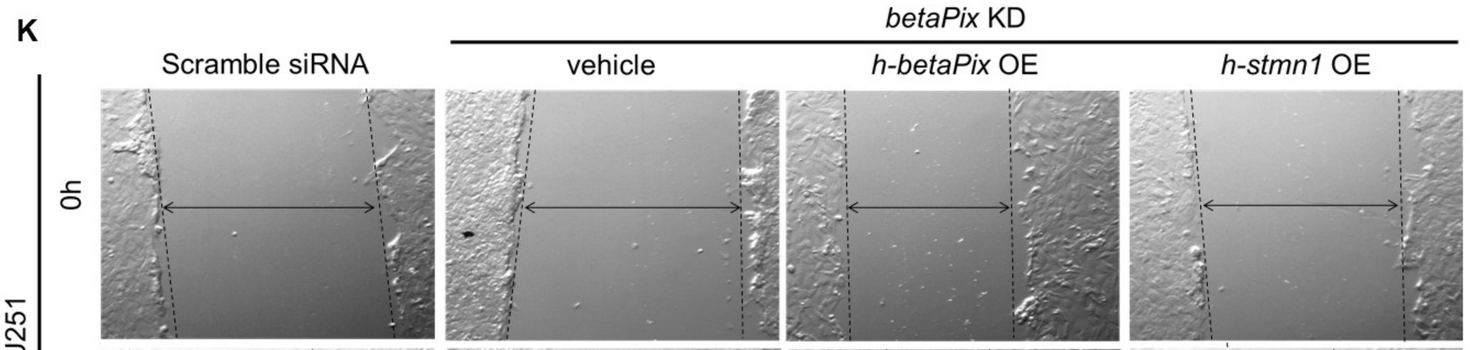


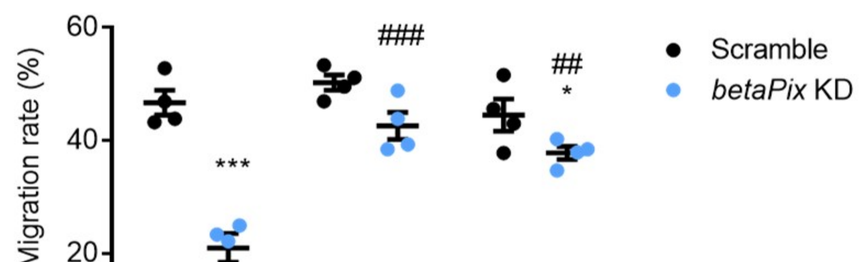


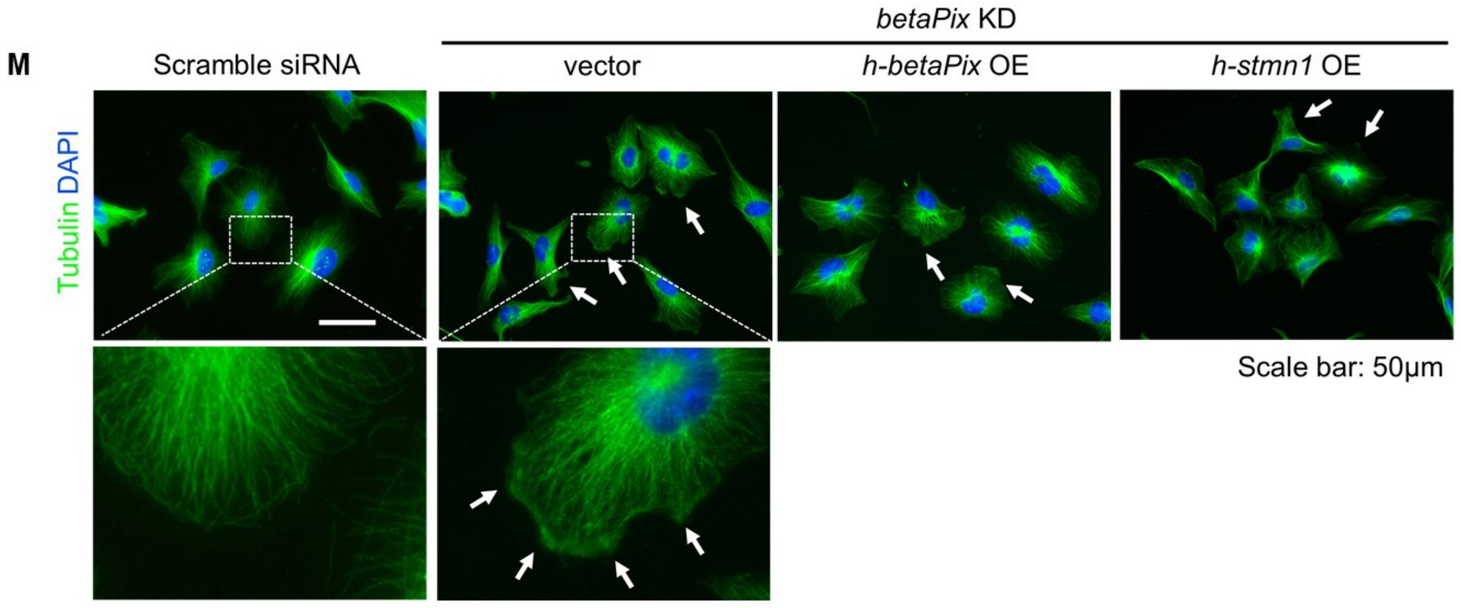


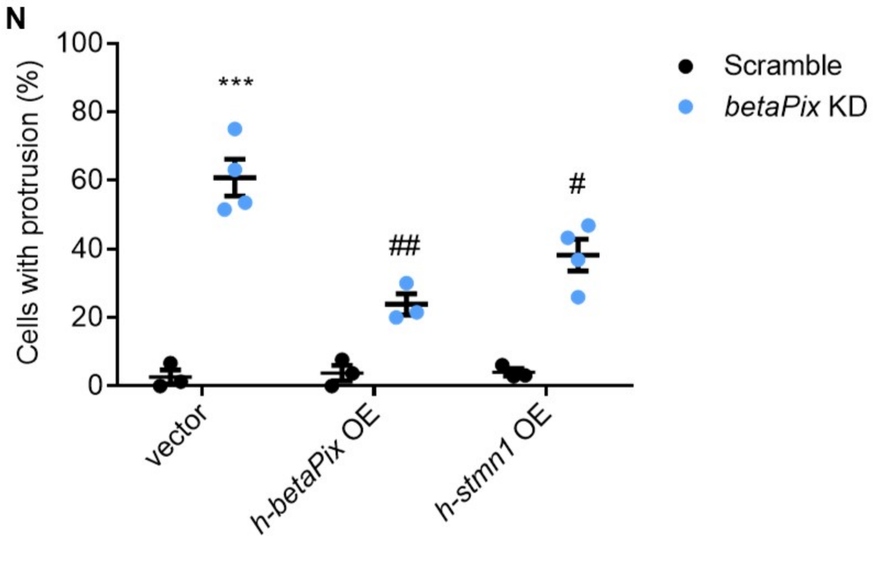






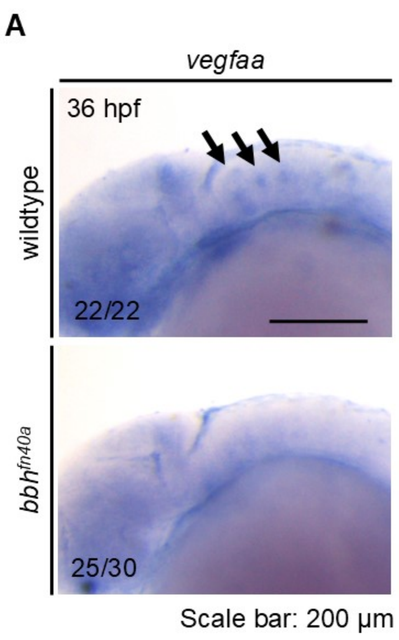


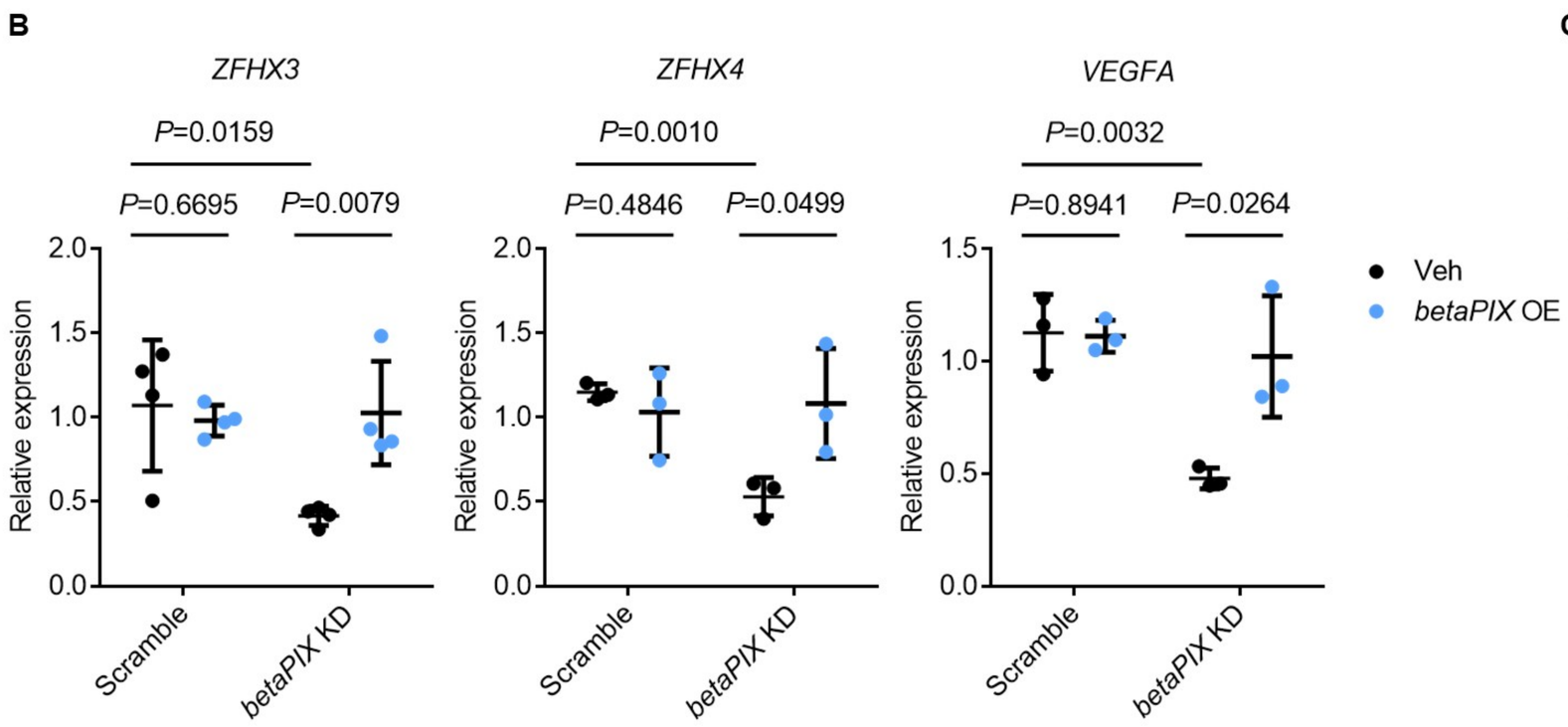


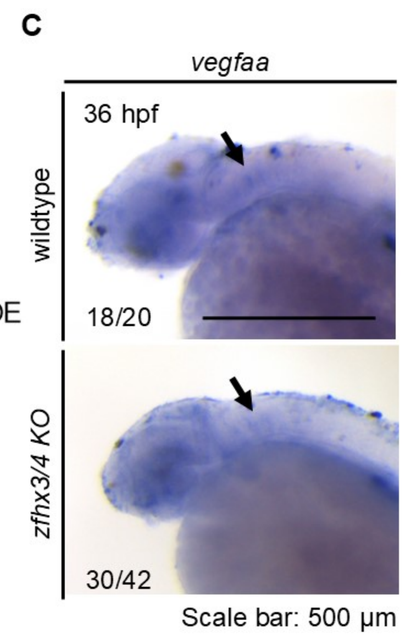


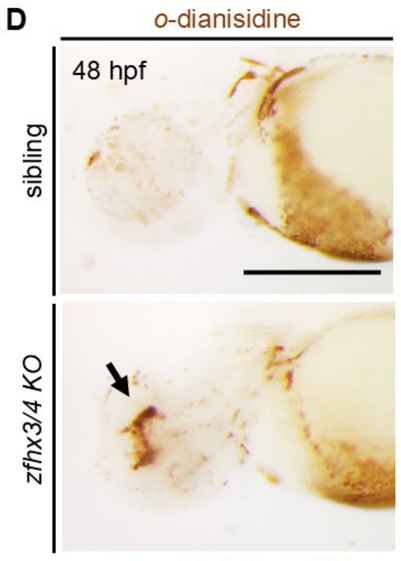
bioRxiv preprint doi: https://doi.org/10.1101/2025.04.08.647738; this version posted April 9, 2025. The copyright holder for this preprint (which was not certified by peer review) is the author/funder, who has granted bioRxiv a license to display the preprint in perpetuity. It is made available under a CC-BY 4.0 International license.

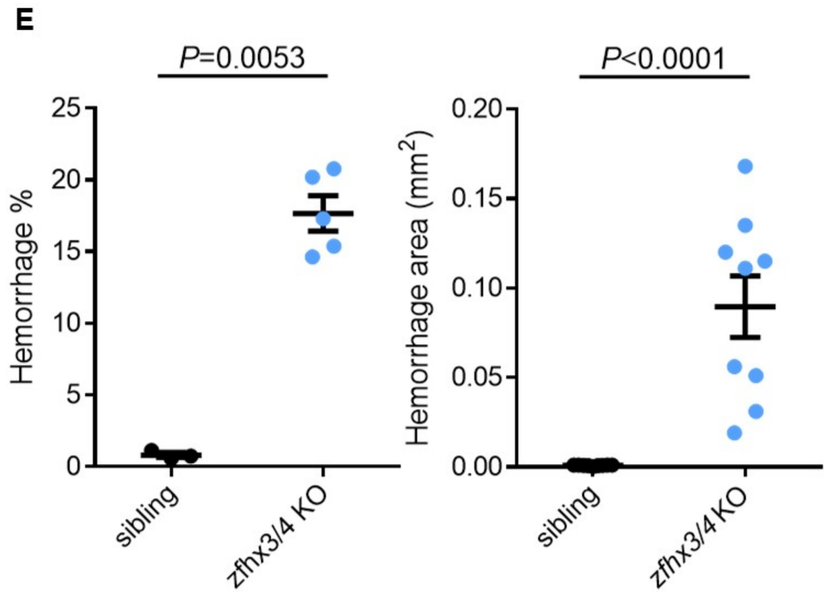
Figure 6

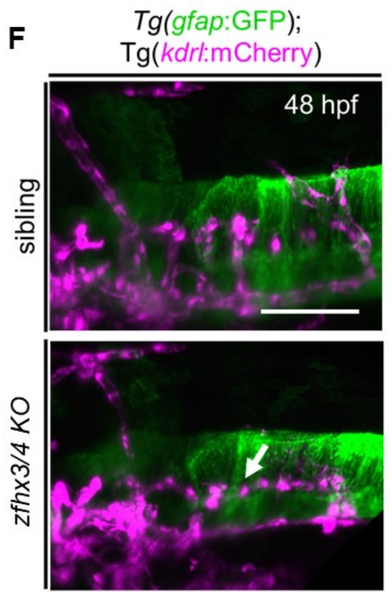


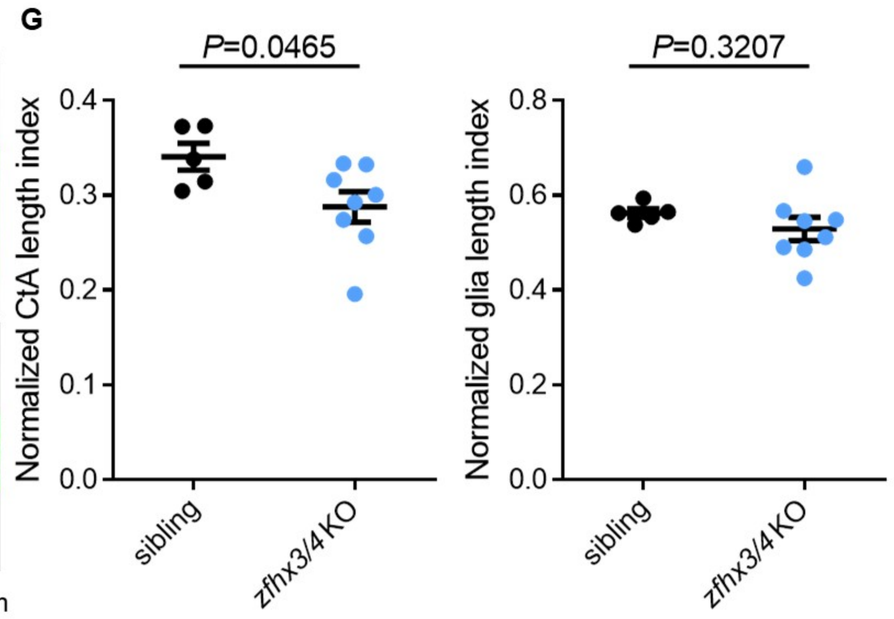


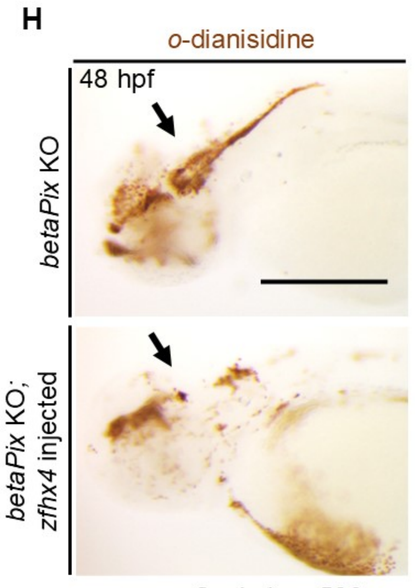


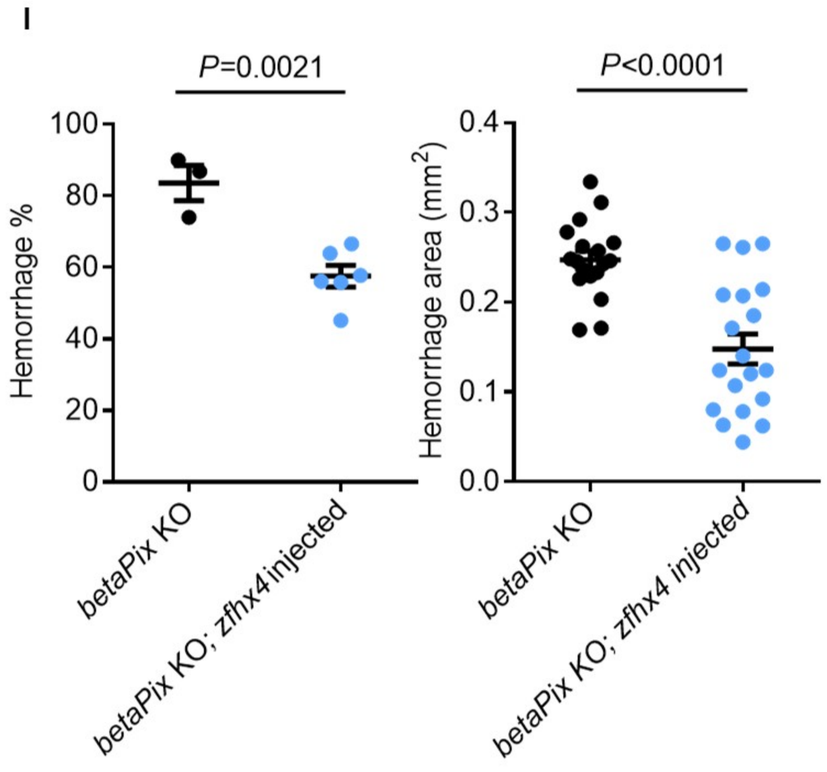


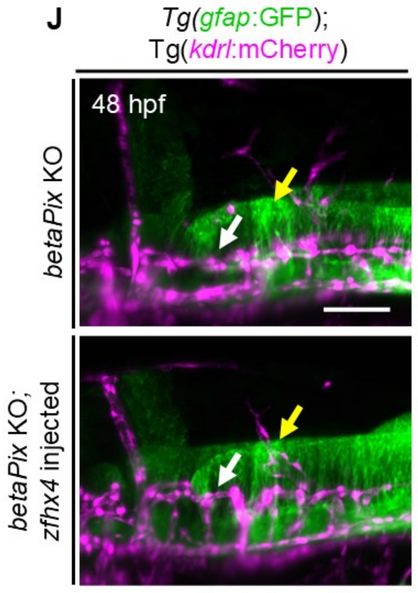


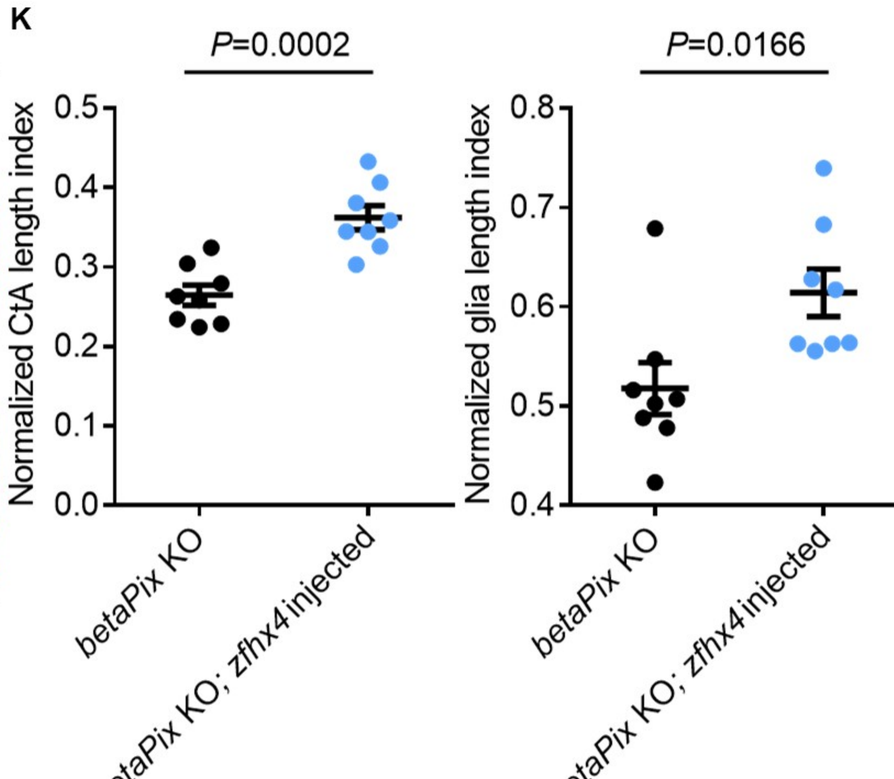


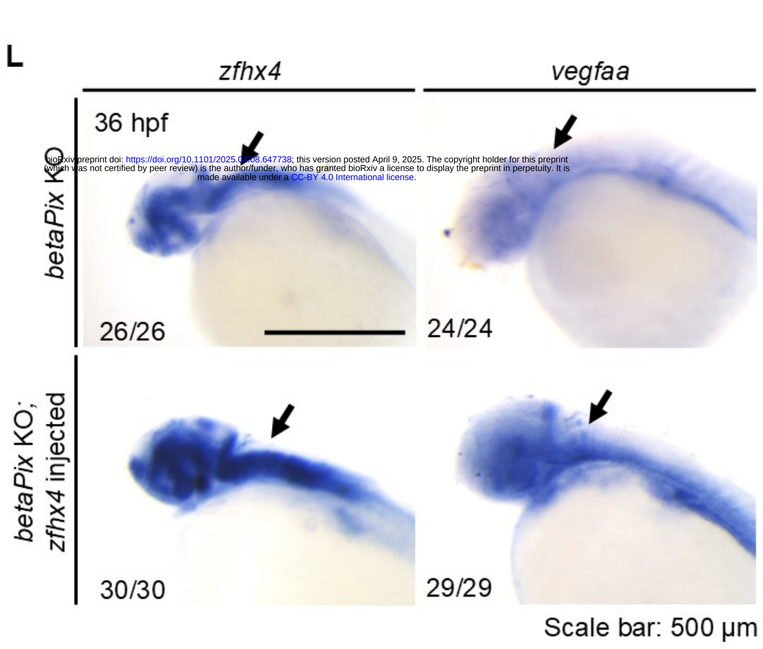












(bioRxiv preprint doi: https://doi.org/10.1101/2025.04.08.647738; this version posted April 9, 2025. The copyright holder for this preprint (which was not certified by peer review) is the author/funder, who has granted bioRxiv a license to display the preprint in perpetuity. It is made available under a CC-BY 4.0 International license.

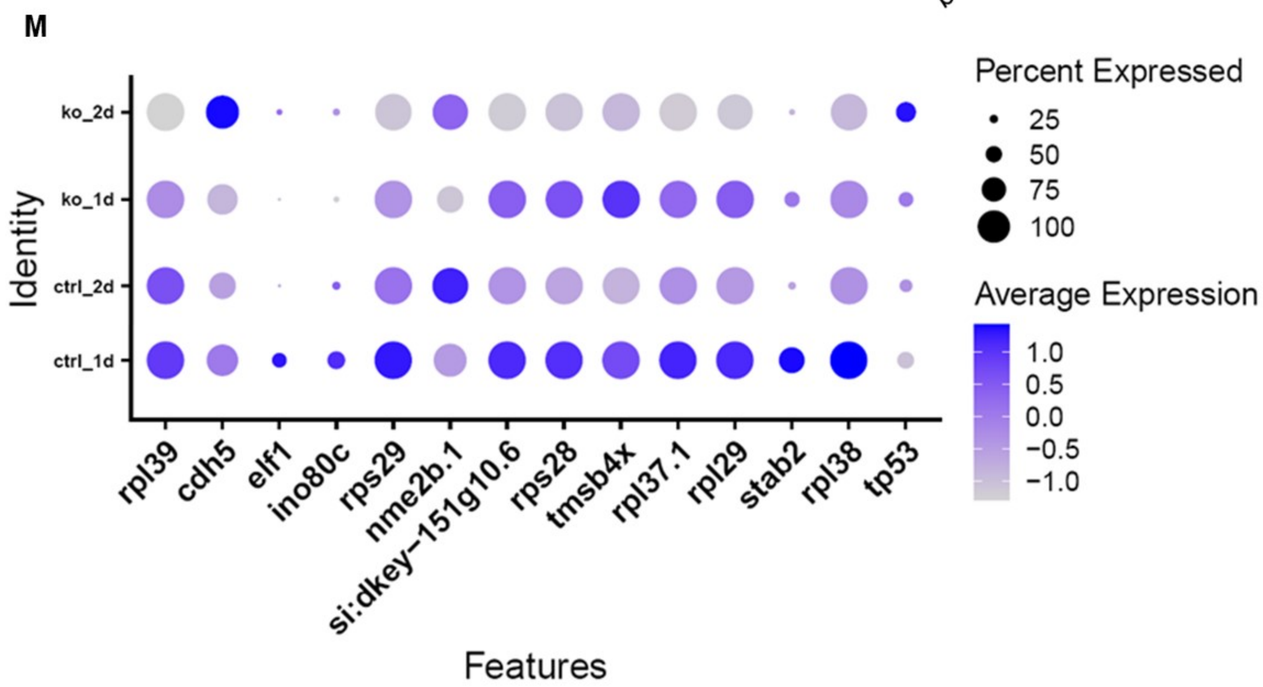
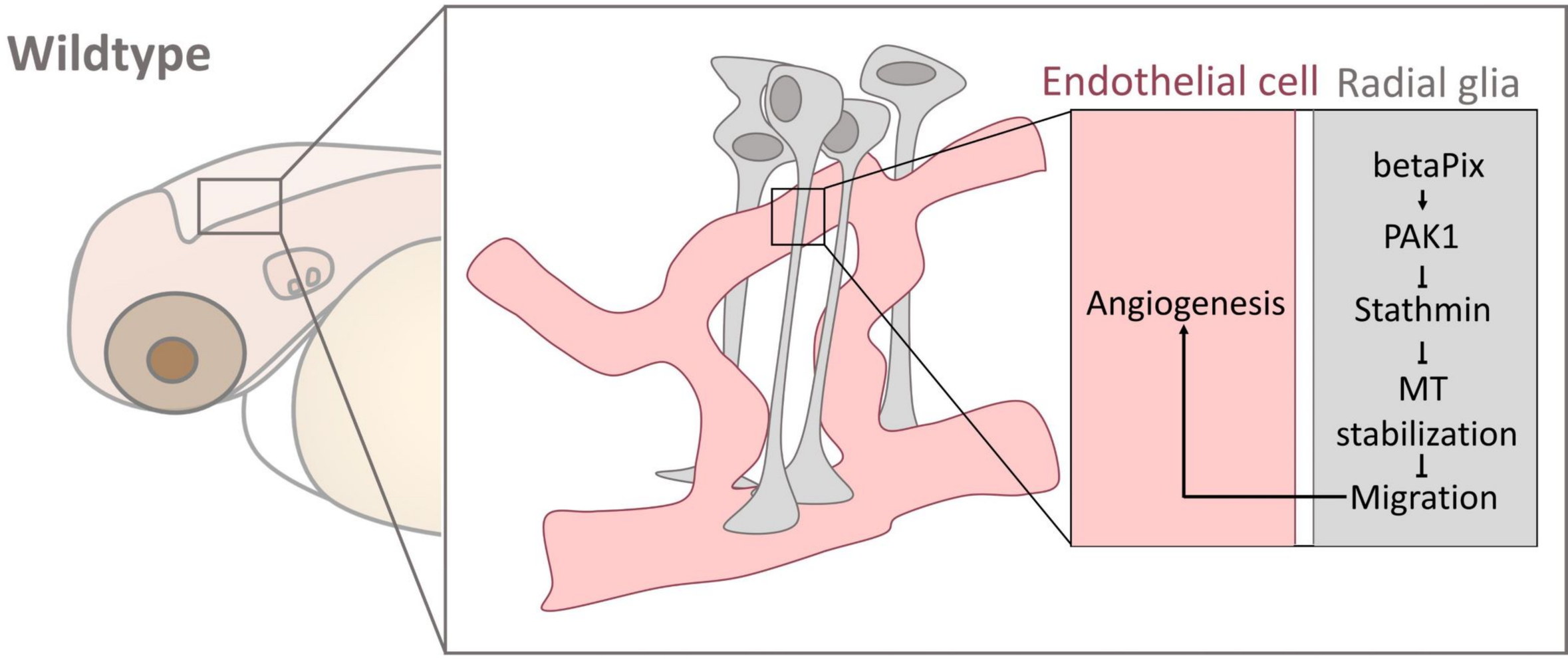
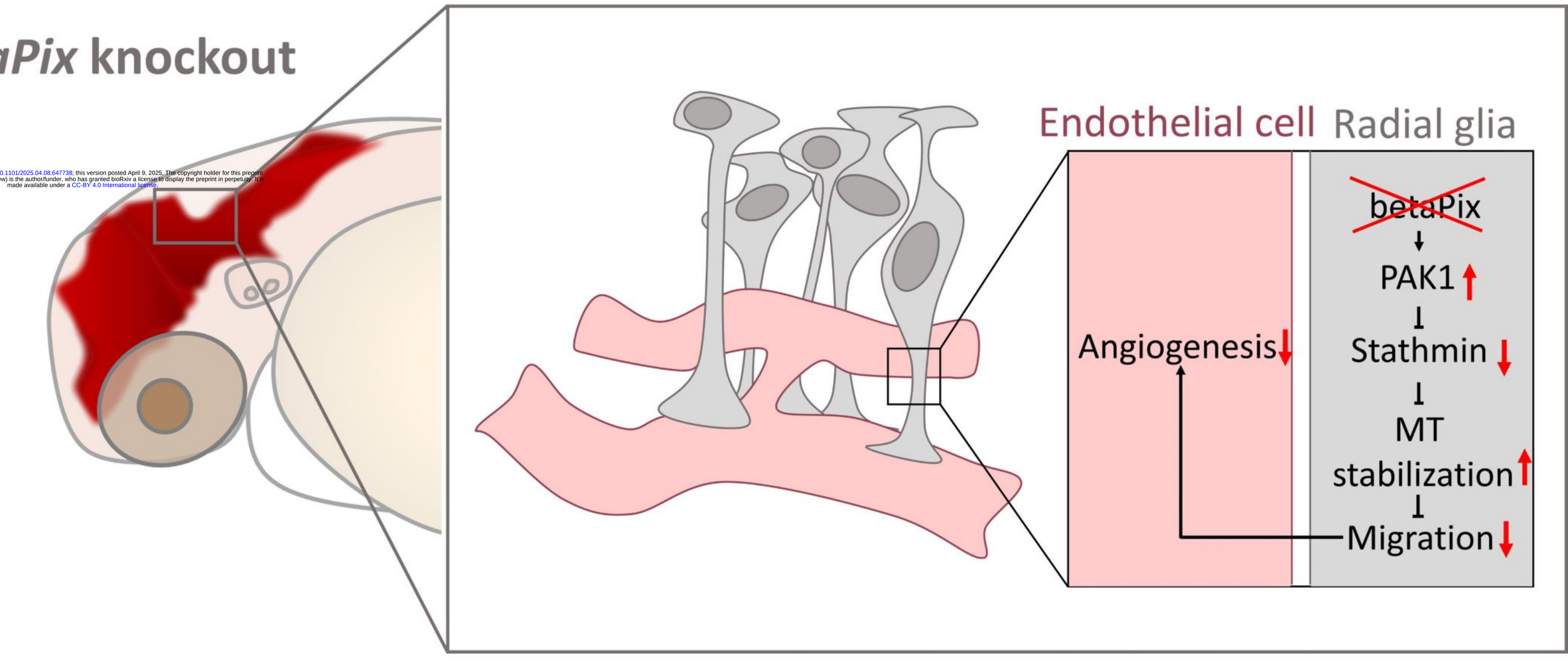


Figure 7





bioRxiv preprint doi: https://doi.org/10.1101/2025.04.08.647738; this version posted April 9, 2025. The copyright holder for this preprint (which was not certified by peer review) is the author/funder, who has granted bioRxiv a license to display the preprint in perpetuity. It is made available under a CC-BY 4.0 International license.